UNIVERSITY OF OKLAHOMA GRADUATE COLLEGE

SEISMIC STRATIGRAPHY, GEOMORPHOLOGY, AND LITHOLOGY PREDICTION OF FLUVIAL AND DEEPWATER SYSTEMS, NORTH MALAY AND DELAWARE BASINS.

A DISSERTATION

SUBMITTED TO THE GRADUATE FACULTY

in partial fulfillment of the requirements for the Degree of

DOCTOR OF PHILOSOPHY

By RUI ZHAI

Norman, Oklahoma

2025

SEISMIC STRATIGRAPHY, GEOMORPHOLOGY, AND LITHOLOGY PREDICTION OF FLUVIAL AND DEEPWATER SYSTEMS, NORTH MALAY AND DELAWARE BASINS.

A DISSERTATION APPROVED FOR THE

SCHOOL OF GEOSCIENCES

BY THE COMMITTEE CONSISTING OF

Dr. Matthew J. Pranter, Chair

Dr. Heather Bedle

Dr. Xingru Wu

Dr. Hao Hu

ACKNOWLEDGEMENTS

First and foremost, I would like to express my profound and heartfelt gratitude to Dr. John D. Pigott, whose guidance, brilliance, and unwavering support were instrumental in shaping this dissertation. I am truly honored to have learned from him. The time we shared, the countless thoughtful discussions, and the wisdom he so generously imparted have impacted both this dissertation and my personal and professional growth. His influence will resonate throughout my career and beyond.

I am deeply thankful to Dr. Matthew J. Pranter for welcoming me into his research group and for the invaluable mentorship, support, and encouragement he provided. His trust in my potential and steady guidance were a great motivation throughout this journey.

My sincere thanks also go to my committee Members, Dr. Heather Bedle, Dr. Xingru Wu, and Dr. Hao Hu, for their insightful suggestions and consistent support during the development of this dissertation.

Lastly, I extend my most profound appreciation to my family. Their steadfast support, boundless patience, and enduring encouragement sustained me through every challenge and triumph of my time at the University of Oklahoma. I am forever grateful for their love and belief in me.

TABLE OF CONTENTS

LIST OF TABLES

LIST OF FIGURES

ABSTRACT

High-frequency seismic sequence stratigraphy and quantitative seismic interpretation are essential for characterizing subsurface reservoirs' architecture and heterogeneity. Although significant advances in the theoretical understanding and research methods of fluvial and deepwater turbidite reservoirs, the inherent complexity of depositional architecture and the variability of reservoir properties continue to pose significant challenges for accurate seismic interpretation. This study addresses these limitations by integrating seismic sequence stratigraphy, seismic geomorphology, seismic inversion, and limited well data, all guided by geological prior knowledge. The aim is to enhance seismic interpretation and lithological prediction in the North Malay and Delaware Basins. The investigation focuses on the falling-stage systems tract (FSST) developed in two contrasting depositional environments, coastal plain and deepwater. First, a high-frequency seismic sequence stratigraphic analysis of the Pleistocene strata in the Northern Malay Basin is conducted, with particular attention paid to the FSST interval. This analysis reveals the internal fill architecture of two distinct types of incised valleys associated with the FSST. Then, seismic geomorphological analysis, using coherence attributes and spectral decomposition, is employed to characterize various mud-filled abandoned channels in fluvial systems spanning multiple FSSTs within the Pliocene–Pleistocene strata. These mud plugs are shown to impact reservoir connectivity significantly. Lastly, in the Delaware Basin, the study applies machine learning techniques and integrated well-seismic Bayesian lithology inversion to predict lithology and assess heterogeneity in mixed siliciclastic–carbonate turbidite reservoirs within the FSST of the Bone Spring Formation.

The insights gained from these multi-disciplinary approaches can be broadly applied to improve the quantitative seismic interpretation of analogous reservoir systems.

INTRODUCTION

The Falling Stage Systems Tract (FSST) is a key component of sequence stratigraphy, representing the deposition interval during a relative sea-level fall (Plint and Nummedal, 2000). It includes all regressive deposits formed after the onset of sea-level fall and before the subsequent rise (Posamentier and Morris, 2000). The FSST is situated above the Highstand Systems Tract (HST) and beneath the Lowstand Systems Tract (LST), bounded below by the sequence boundary and above by LST deposits. The FSST concept has evolved through various stratigraphic models (e.g., Posamentier and Vail, 1988; Van Wagoner et al., 1988; Hunt & Tucker, 1992; Catuneanu et al., 2009). Recognizing this systems tract is essential for building high-frequency stratigraphic frameworks, as it improves the precision of interpretations related to sea-level fluctuations and sedimentary processes. Furthermore, FSST interpretation critically impacts hydrocarbon exploration because forced regression influences sediment dispersal patterns and controls reservoir quality. Identifying the FSST in the stratigraphic record requires recognizing specific surfaces and stacking patterns. These include erosive-based shoreface sand bodies formed by wave scouring during sea-level fall and characteristic progradational stacking geometries, where sedimentary units step downward and basinward.

Recent advances in 3-D seismic sequence stratigraphy and seismic geomorphology (Wood, 2007; Posamentier et al., 2022) have improved the ability to detect and interpret such stacking patterns. Seismic geometric attributes, spectral decomposition, Bayesian lithology inversion, and machine learning techniques (Castagna and Sun, 2006; Larsen et al., 2006; Schmidhuber, 2015; Chopra and Marfurt, 2018) have enhanced our understanding of sedimentary dynamics influenced by high-frequency relative sea-level fluctuations and variable sediment supply. Integrating high-resolution seismic data with geomorphological analyses allows for a more accurate subsurface architecture interpretation and a better deposit distribution prediction.

Chapter 1 presents a study integrating seismic sequence stratigraphy and seismic geomorphology to investigate incised valleys within the Pleistocene strata of the North Malay Basin, Gulf of Thailand. Unlike standard models, in low-gradient coastal plains, FSST deposits are absent in interfluvial areas and only preserved within incised valleys above subaerial unconformities, where they developed on a specific transgressive erosional and appear as terraced fluvial deposition.

Chapter 2 analyzes various abandoned channels formed in the Pliocene–Pleistocene strata of the North Malay Basin, Gulf of Thailand. Within a high-frequency stratigraphic framework, seismic geomorphology was employed to characterize abandoned channels within fluvial systems by using 3-D geometric seismic attributes and spectral decomposition. These channels are commonly filled with mud plugs that significantly impair reservoir connectivity.

Chapter 3 focuses on the Bone Spring Formation in the Delaware Basin, southeast New Mexico, and West Texas. 3-D seismic and well-log data were integrated to analyze mixed siliciclastic-carbonate turbidite reservoirs deposited during FSST. Lithologies were predicted using a multilayer perceptron neural network, and Bayesian lithology inversion was subsequently used to map their spatial distribution. Reservoir stacking patterns and lithology distribution directly impact reservoir heterogeneity.

REFERENCES

Castagna, J. P., and S. Sun, 2006, Comparison of spectral decomposition methods: First Break, v. 24, no. 3, p. 75–79.

Catuneanu, O., V. Abreu, J. P. Bhattacharya, M. D. Blum, R.W. Dalrymple, P. G. Eriksson, C. R. Fielding, W. L. Fisher, W. E. Galloway, M. R. Gibling, and K. A. Giles, 2009, Towards the standardization of sequence stratigraphy: Earth–Science Reviews, v. 92, no. 1, p. 1–33.

Chopra, S., and K. J. Marfurt, 2018, Coherence attribute applications on seismic data in various guises–Part 1: Interpretation, v. 6, no. 3, p. T521–T529.

Hunt, D., and M. E. Tucker, 1992, Stranded parasequences and the forced regressive wedge systems tract: deposition during base–level fall: Sedimentary Geology, v. 81, no. 1, p. 1–9.

Larsen, A. L., M. Ulvmoen, H. More, and A. Buland, 2006, Bayesian lithology/fluid prediction and simulation on the basis of a Markov-chain prior model: Geophysics, v. 71, no. 5, p. B69–B78.

Plint, A. G. and D. Nummedal, 2000, The falling stage systems tract: recognition and importance in sequence stratigraphic analysis, Geological Society, London, Special Publications, v. 172, p. 1–17.

Posamentier, H. W. and W. R. Morris, 2000, Aspects of the stratal architecture of forced regressive deposits, Geological Society, London, Special Publications, v.172, p. 19–46.

Posamentier, H. W. and P. R. Vail, 1988, Eustatic controls on clastic deposition II—sequence and systems tract models: Society of Economic Paleontologists and Mineralogists, Special Publication v. 42, p. 125–154.

Posamentier, H.W., V. Paumard, and S. C. Lang, 2022, Principles of seismic stratigraphy and seismic geomorphology I: Extracting geologic insights from seismic data: Earth-Science Reviews, v. 228, p. 103963(1-57).

Schmidhuber J., 2015, Deep learning in neural networks-An overview: Neural Networks, v. 61, p. 85–117.

Van Wagoner, J.C., H. W. Posamentier, R. M. Mitchum, P. R. Vail, J. F. Sarg, T. S. Loutit, and J. Hardenbol, 1988, An overview of the fundamentals of sequence stratigraphy and key definitions, in C. K. Wilgus, et al., eds: Sea-level changes: An integrated approach: Society of Economic Paleontologists and Mineralogists, Special Publication v. 42, p. 39–46.

Wood, L. J., 2007, Quantitative seismic geomorphology of Pliocene and Miocene fluvial systems in the northern Gulf of Mexico, USA: Journal of Sedimentary Research, v. 77, no. 9, p. 713–730.

Chapter 1: Searching for the Missing Link: Falling-Stage Systems Tract – Seismic Stratigraphic Evidence from the North Malay Basin, Gulf of Thailand

ABSTRACT

This study investigates the stratigraphic architecture and morphology of incised valleys within the Pleistocene strata of the North Malay Basin to advance the understanding of the Falling-Stage Systems Tract (FSST) in low-gradient coastal plain settings. Nearly 900 km2 of high-resolution three-dimensional seismic data are employed to apply seismic sequence stratigraphy and seismic geomorphology for interpreting fluvial responses to base-level fluctuations. The results indicate that the FSST is poorly developed in interfluvial areas where highstand deposits directly overlap the subaerial unconformity. Tidal reworking during early transgression modified the subaerial unconformity into a transgressive ravinement surface. Together, they form a composite stratigraphic surface. In contrast, incised valleys preserve a complete FSST record expressed as terraced channel fills and stepped erosional surfaces, representing episodic fluvial incision during base-level fall followed by partial reworking during transgression. Two types of incised valleys are recognized. Low-sinuosity valleys display straight geometries and steep valley walls, reflecting vertical incision under confined conditions. A high-sinuosity valley exhibits broad meander belts and is interpreted as an inherited morphology from highstand fluvial systems, with additional modification due to tidal processes and relative proximity to a paleo-estuary. These findings highlight the spatial variability in FSST expression and preservation across the coastal plain. The interplay among fluvial dynamics, antecedent topography, sediment supply, and position relative to the shoreline firmly controls incised valley architecture. This work refines models of FSST development and sequence stratigraphic interpretation in coastal plain environments influenced by sea-level change.

1.1 INTRODUCTION

The falling-stage systems tract (FSST) refers to all strata accumulated during the forced regression of the shoreline in response to relative sea-level fall (Posamentier and Morris, 2000). The understanding of this systems tract has evolved significantly across different sequence stratigraphic models (Posamentier and Vail 1988; Van Wagoner et al., 1988; Hunt and Tucker, 1992; Nummedal et al, 1993; Ainsworth and Pattison, 1994; Plint and Nummedal, 2000). In the now widely accepted four systems tracts model, the FSST is bounded at its base by a marine basal surface of forced regression and at its top by a subaerial unconformity and its correlative conformity (Plint et al., 1988; Hunt and Tucker, 1992; Plint et al., 2001; Catuneanu et al., 2009). Its most prominent identifying feature is the downstepping offlap patterns on seismic profiles. Based on different sequence stratigraphic models, many studies have provided significant insights into the relationship between stratal stacking patterns and sedimentary facies distribution within the FSST, the linkage between nonmarine facies and coeval marine facies of FSST deposits, and controlling factors (Shanley and McCabe, 1994; Mattheus and Rodriguez, 2011; Holbrook and Bhattacharya, 2012; Blum et al., 2013). Most of this research has focused on forced regressive wedges along continental margins, as it is regarded as the product of coastal sediment progradation during sea-level fall (Plint and Norris, 1991; Mellere and Steel, 1995; Plint, 1996; Fitzsimmons and Johnson, 2000; Bhattacharya and Willis, 2001; Waelbroeck et al., 2002). In contrast, understanding FSST stratigraphic records in coastal plain settings remains a significant challenge due to difficulties in identification. It even appears as a missing link within the succession of systems tracts.

In response to base-level falls, fluvial systems in coastal plain settings extend their drainage networks and form incised valleys across exposed continental shelves (Van Wagoner et al., 1987, 1990; Posamentier et al., 1991; Allen and Posamentier 1993; Suter, 2006; Holbrook and Bhattacharya, 2012). Incised valley systems can extend seaward from an inland point unaffected by relative sea-level changes for tens to hundreds of kilometers, terminating valley mouths in lowstand deltas. As a result, they have the potential to preserve evidence of the transition from regression to transgression within a complete base-level cycle (Ardies et al., 2002; Bowen and Weimer, 2003; Strong and Paola, 2008; Wellner et al., 2018). Studies of Quaternary incised valleys along continental margins have provided insights into valley morphology, infill, and the processes regulating their deposition (Blum and Tornqvist, 2000; Wellner et al., 2003; Anderson et al., 2004; Labaune et al., 2005; Dalrymple, 2006; Gibling, 2006; Simms et al., 2006; Labaune et al., 2010; De Santis and Caldara, 2016 Alqahtani et al., 2017). However, the morphological expression, formation processes, and scale variations of incised valleys within a stratigraphic framework remain active research areas, as the dynamic depositional characteristics create significant variability.

This study focuses on the high-resolution seismic stratigraphic architecture and Pleistocene strata incised valleys in the North Malay Basin, Gulf of Thailand. Numerous long incised valley systems developed on exposed low-gradient paleo-topography during multiple Pleistocene sea-level falls. The study area has long been situated in a coastal plain setting between the uplifted hinterland and delta on the tectonically stable parts of the Sunda Shelf, making it an ideal location for 3-D seismic observation. This study aims to answer the following questions: (1) where and how are falling-stage systems tracts (FSST) deposits preserved within the coastal plain setting? (2) what stratigraphic surfaces define the FSST? Moreover, (3) what is the seismic expression of the FSST and incised valleys? This study provides new insights into the development of FSST under fluctuating base-level, enhancing our understanding of sedimentary responses to base-level changes in coastal plain environments. It also significantly contributes to the seismic geomorphological analysis of incised valleys by documenting the architecture of incised valleys infilled with complex fluvial and shallow marine deposits. These findings have broader implications for interpreting stratigraphic records in analogous low-gradient shelf settings.

To achieve these research objectives, we first identified and traced multiple stratigraphic surfaces within the Pleistocene strata within the study area and conducted seismic sequence stratigraphic interpretations. Within a sequence stratigraphic framework, we analyzed the stratigraphic architecture of the FSST in the uppermost seismic unit of the Late Pleistocene. Seismic profiles and slices were integrated to quantitatively interpret incised valleys' morphology, dimensions, and internal architecture. Finally, different incised valleys within the same FSST were compared and discussed. The study utilized high-resolution 3-D seismic surveys acquired across multiple years, covering 900 km^2 (347 mi^2), to enable geomorphological analysis of Late Pleistocene incised valley systems. Additionally, four borehole logs and lithological reports from five wells were used to determine lithologies.

1.2 GEOLOGICAL SETTING

The North Malay Basin is the northern part of the grand Malay Basin, located in the center of the Gulf of Thailand (GoT) and east of the Malay Peninsula. (Figure 1.1). The North Malay Basin is approximately 300 km (186 mi) long and 100 km (62 mi) width, with a northwest-southeast trend. The basin is separated from the Pattani Basin to the northwest and the Malay Basin to the southeast by basement highs. The North Malay Basin is one of several Cenozoic intracratonic rift basins west of the Sunda Shelf, a broad, low-gradient continental shelf of Mainland Southeast Asia. The tectonic evolution of the North Malay Basin consists of four phases: (1) Rifting (Late Eocene to Late Oligocene). The Indo-Australian Plate collided with the Eurasian Plate produced a transtensional shearing regime across the north-central Sunda Block. This process created a broad northwest-southeast left-lateral shearing zone across the GoT, extending from Three Pagodas fault systems (Morley, 2002; Pubellier and Morley, 2014). Lateral movements along these faults initially created the roughly north-south striking, pull-apart North Malay Basin. During the Oligocene, right-lateral shearing along the basin margin led to the formation of extensive half-grabens and structural highs. (2) Rapid Subsidence (Early to Middle Miocene). Thermal effects on the lithosphere and sediment loading induced lower crustal flow toward the surrounding highlands, creating significant accommodation for terrigenous sediment fluxes after extensional rifting ceased (Mansor et al., 2014). (3) Structural Inversion (Middle to Late Miocene). The northward subduction of the Indo-Australian Plate beneath the Sunda Block induced right-lateral shearing across the GoT. Transpression caused the uplift of the North Malay Basin, leading to the formation of a prominent regional Late Miocene unconformity. Sea-level fluctuations reduced terrigenous clastic supply during

Figure 1.1: Outline of the Cenozoic basin in the Gulf of Thailand, Sundaland, SE Asia (modified from Morley, 2002). The North Malay Basin is approximately 180 km (112 mi) from the shoreline and the average water depth is about 80 m (262 ft).

transgressions and generated several unconformities during regressions. (4) Steady Subsidence (Pliocene to Pleistocene). After tectonic inversion, the North Malay Basin underwent a prolonged phase of steady subsidence, eventually submerging due to transgression.

The North Malay Basin contains over 12 km (7.5 mi) of Oligocene–Holocene sediments, primarily of terrestrial and shallow marine origin, in its central region (Darmadi et al., 2007; Madon et al., 2013). Several stratigraphic schemes and nomenclatures from seismic stratigraphy, sequence stratigraphy and biostratigraphy are used to describe the Cenozoic strata (Hanebuth and Stattegger, 2003; Yakzan et al., 1996; Morley and Racey, 2011). The main stratigraphic subdivisions are summarized in Figure 1.2. The North Malay Basin stratigraphy is divided into five third-order sequences (Sequence I to Sequence V) corresponding to the basin's tectonic evolution. Sequence I comprises syn-rift and early post-rift strata deposited from the Late Eocene to Early Miocene. The oldest drilled sediments in the basin are Oligocene in age. The syn-rift strata consist of axial and transverse sediment influxes within the half-grabens, where lacustrine shale is interbedded with alluvial fan and fluvial-deltaic sandstone overlying the basement. The uppermost part is overlain by early post-rift lacustrine shale. Sequence II was deposited during the rapid subsidence stage of the Early Miocene. The former lake evolved into extensive wetlands, while fluvial systems transported large sediment loads from the northern margin into the basin, forming thick successions of fluvial sandstone and floodplain shale. The shale indicates a transition from lacustrine deposition to nearshore swamps. Sequence III was characterized by basin subsidence and transgression during the Miocene thermal subsidence. Much of the area covered by coastal plain, sea-level fluctuations resulted in the sequence composed of several transgressive-regressive cyclic depositions, which are dominated by fluvial sandstone, siltstone from basement highs, and marginal marine deposits associated with transgressions. Sequence III was marked by basin subsidence and transgression during Miocene thermal subsidence. Sea-level fluctuations led to a sequence composed of multiple transgression and regression on coastal plain, dominated by fluvial sandstone from basement highs, and marginal marine deposits associated with transgressions. Sequence IV was formed during the regression stage resulting from basin inversion in the late Middle to Late Miocene, featuring a regional unconformity at the top. Sequence IV formed during the regression stage due to basin inversion in the late Middle to Late Miocene, featuring a regional unconformity at the top. Sea-level falls during the late Miocene resulted in a basin-wide regression, leading to the development of fluvial systems along the basin axis. The strata comprised interbedded sandstone, siltstone, and shale with coals primarily deposited in coastal plain and floodplain environments. Sequence V consists of the Pliocene to recent deposits formed during the basin's thermal subsidence. Repeated cycles of transgression and regression led to interbedded fluvial and shallow marine successions, separated by unconformities.

This study focuses on fluvial succession of Sequence V. From the Pliocene to the present, sea-level fluctuations have intensified erosion around the Noth Malay Basin, driving a continuous influx of sediments from the north into the North Malay Basin via fluvial systems.

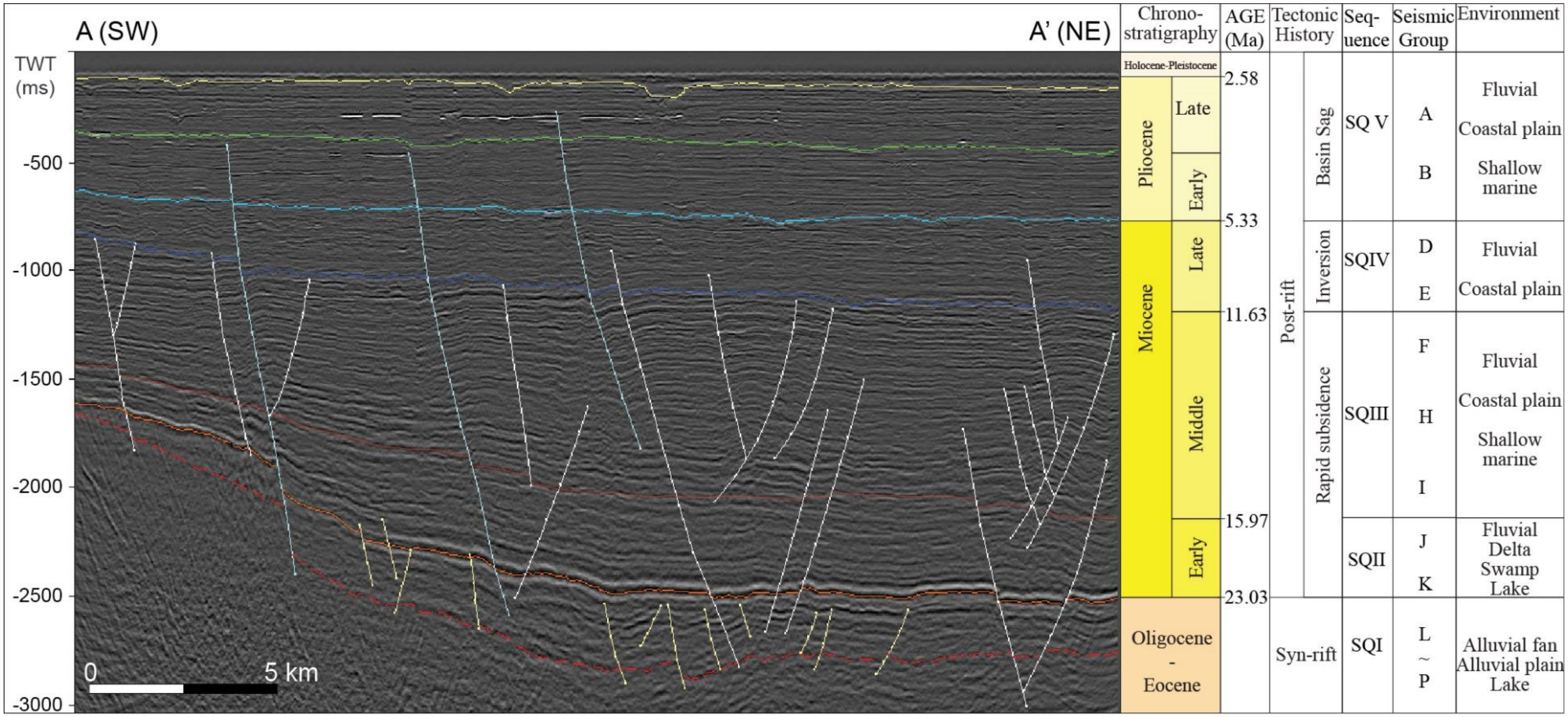

Figure 1.2: Stratigraphic summary across the North Malay Basin.

1.3 METHODS AND WORKFLOW

This study uses an integration of seismic sequence stratigraphy and seismic geomorphology approaches to interpret various fluvial stratigraphic features, from large-scale stratigraphic patterns to small-scale geomorphic features. The four systems tracts classification approach (Catuneanu, 2006; Catuneanu et al., 2009) and seismic sequence stratigraphy (Vail,1987; Van Wagoner et al., 1987, 1988, 1990) were applied to the 3-D seismic data-driven interpretations of local stratigraphic architectures. The four systems tracts classification approach inherently accounts for key stratigraphic events, including the onset and end of forced regression event, the end of a regression event, and the end of a transgression event, enabling the interpretation of stratigraphic stacking patterns in response to a complete base-level cycle. The onset of forced regression marks the transition from the Highstand Systems Tract (HST) to the Falling-Stage Systems Tract (FSST), the end of forced regression signifies the termination of the FSST and the initiation of the Lowstand Systems Tract (LST). The onset of transgression corresponds to the transition from the LST to the Transgressive Systems Tract (TST), while the end of transgression marks the shift from the TST back to the HST.

In this study, we focus on two key aspects of seismic sequence stratigraphic analysis: the superposition and internal variability of seismically recognizable stratigraphic surfaces, defined by reflection terminations, and the geometry of seismic facies, which provides additional sedimentological insights into these surfaces. The interpretation workflow involves: (1) identifying seismic reflection packages and their stacking trends, such as oblique, chaotic, and hummocky patterns; (2) delineating seismic reflection terminations and identifying key seismic stratigraphic surfaces, such as seismic-scale stratigraphic discontinuities, erosional truncations, onlap, and downlap; (3) subdividing the stratigraphic record into systems tracts based on the genetic relationships of seismic stratigraphic units; (4) defining typical sections for each systems tract to support regional stratigraphic correlation; (5) interpreting systems tracts in relation to base-level cycle stages.

Within the stratigraphic framework, geologically significant depositional patterns are extracted along the stratigraphic surfaces to analyze the evolution of stratigraphic surfaces and depositional patterns in plan-view by integrating stratigraphic architecture observed in seismic profiles (Cartwright and Huuse, 2005; Chopra and Marfurt, 2007; Posamentier, 2002, 2004). Advances in 3-D seismic attribute algorithms have enhanced seismic geomorphologic analyses, providing reliable support for paleogeomorphological interpretation (Posamentier and Kolla, 2003; Kolla et al., 2007; Chopra and Marfurt, 2008; Posamentier et al., 2022). To identify depositional features along stratigraphic surfaces and ensure accurate seismic geomorphological analysis, this study applied energy-ratio eigenstructure coherence attribute (Appendix), which has proven effective in highlighting lateral boundaries of continuous geological bodies (Marfurt et al., 1998; Marfurt, 2006; Chopra and Marfurt, 2007). Successive horizonal slices were constructed using geologically meaningful time surfaces, such as the unconformity and the seafloor reflection, as reference horizons to visualize attribute patterns in plan view. Seismic geomorphologic patterns were then interpreted, and their parameters analyzed based on sedimentological models and regional geological context.

1.4 RESULTS

1.4.1 Stratigraphic Surfaces

Three stratigraphic surfaces including subaerial unconformity (SB), maximum flooding surface (MFS), and transgressive ravinement surface (TRS), are identified based on regional stratal terminations and local stratal geometric relationships. These stratigraphic surfaces reflect variations in depositional environments and correspond to base-level changes over time.

(1) Subaerial Unconformity

Regional subaerial unconformity is identified and traced within Pleistocene strata across the entire study area (Figure 1.3). It is characterized by fluctuating, continuous high-amplitude reflections that truncate the underlying horizontal reflections. The unconformity has a low-gradient seaward slope and a topographic lowland characterized by a U-shaped valley pattern, marking its incision base. High-amplitude or chaotic reflections within the U-shaped pattern overly the unconformity, extending outward into surrounding parallel stratigraphic reflections. The late Pleistocene strata, is bounded by the unconformity at the base and the seafloor reflection at the top, constitute the target interval of this study.

(2) Maximum Flooding Surface

The maximum flooding surface (MFS) appears as a moderate amplitude reflection positioned on the top of the topographic depression. The critical identifying characteristic of the MFS is its position over the U-shaped valley pattern and onlapping its top margin (Figure 1.3). The MFS is characterized by an acoustic impedance contrast, separating the low-impedance strata within the topographic depression from the high-impedance

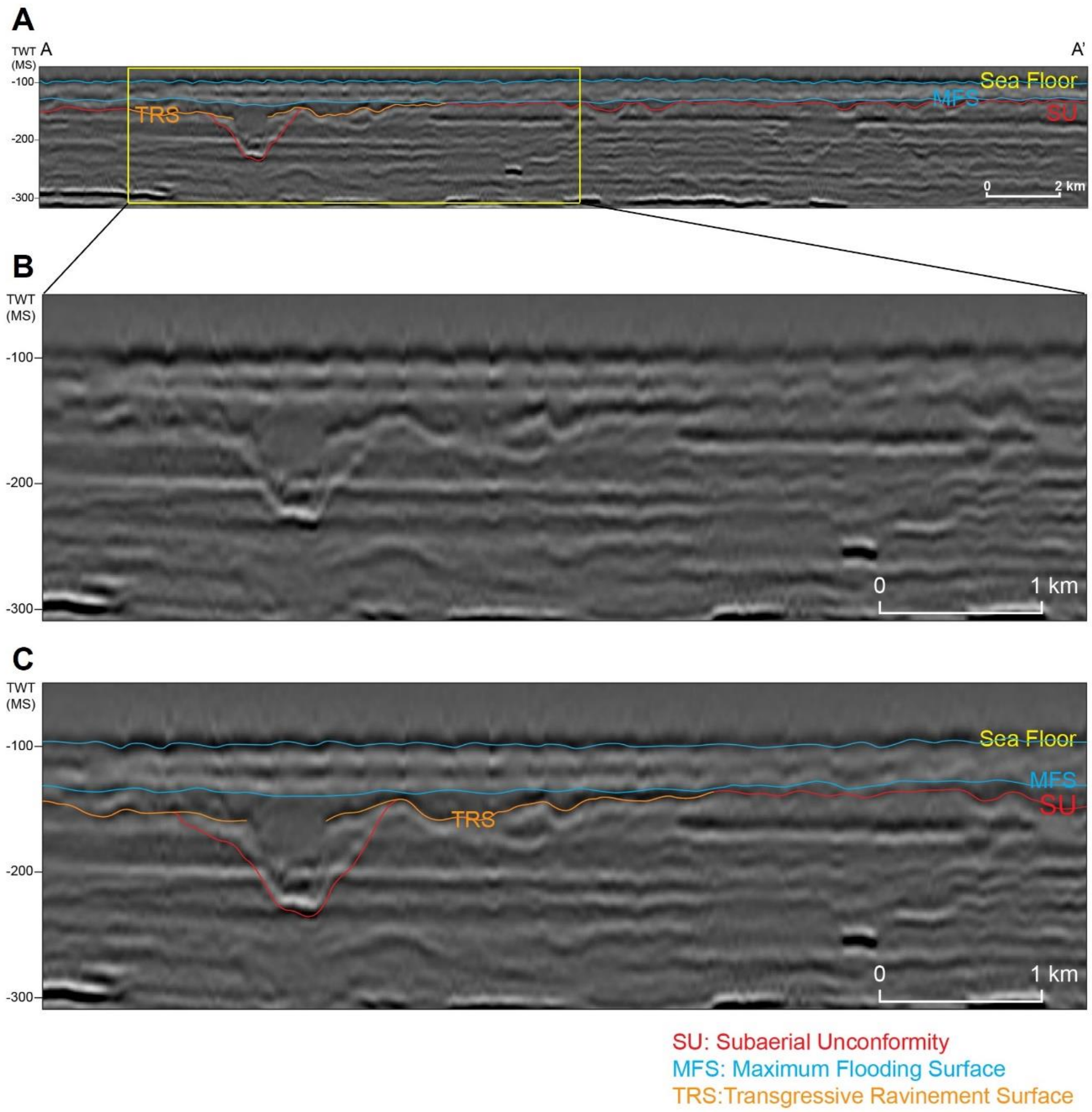

Figure 1.3: Seismic stratigraphic surface identification in the study succession (the profile location can be found in Figure 1.1). The subaerial unconformity is regional reflection that truncates the underlying reflections. The maximum flooding surface is only developed on the top of low-relief topography and extends laterally into the subaerial unconformity. The transgressive ravinement surface is localized and merges with the subaerial unconformity at the top of U-shaped reflections, forming a composite surface.

overlying strata. This transition marks the top of a fining-upward transgression succession from the basal unconformity. The MFS is overlain by nearly parallel, weak-to-moderate-amplitude reflections, confirming that transgression did not terminate at this conformable surface. The overlying reflections indicate highstand normal regression deposition.

(3) Transgressive Ravinement Surface

The transgressive ravinement surface (TRS) is a distinct stratigraphic surface observed on the subaerial unconformity and within the overlying fluvial strata. The TRS, which overlies the subaerial unconformity, forms due to tidal reworking during shoreline retreat. The TRS is characterized by local undulating reflections of the subaerial unconformity near the U-shaped valley pattern (Figure 1.3). In these areas, the TRS manifests as an impedance contrast, distinguishing the underlying high-impedance seismic facies associated with channel deposition from the overlying low-impedance transgression deposition. On seismic slices, the TRS is marked by transgressive scours and tidal-influenced dendritic channels. Within the fluvial strata, the TRS is difficult to identify on seismic profiles due to its small scale. However, it can be recognized drainage patterns on seismic slices through channel tops.

1.4.2 Seismic Facies

Six seismic facies (Figure 1.4) are identified based on observations of external geometry and internal configuration on seismic profiles, considering stratigraphic contact relationships, vertical stacking patterns, and facies belt variations.

Seismic facies 1 (SF1) represents a regional stratigraphic reflection package, bounded by erosional truncation of the subaerial unconformity. SF1 is characterized by weak-moderate amplitude, oblique-parallel reflections dipping seaward at a low angle (up to 1°).

Seismic facies 2 (SF2) is characterized by an infilling sequence composed of low to semitransparent amplitude, parallel, and continuous reflections arranged in aggrading packages. SF2 occurs only in the upper part of the U-shaped valley pattern, with onlap terminations along its walls.

Seismic facies 3 (SF3) exhibits a U-shaped valley pattern above the subaerial unconformity and is overlain by chaotic to variable high-amplitude reflections. The base of SF3 is characterized by incisions, where a strong acoustic impedance contrast highlights the erosional truncation and underlying parallel reflections.

Seismic facies 4 (SF4) generally consists of high-amplitude, chaotic to subparallel reflections within SF4. SF4 predominantly forms the middle to lower part of SF4, incomplete SF5 units can occur at varying depths along the internal flank of SF4.

Seismic facies 5 (SF5) consists of sigmoid to tangential-oblique parallel reflections associated with lateral accretions restricted to the lower part of SF5. These reflections dip toward the deepest part of SF5 and are overlain by SF2.

Seismic facies 6 (SF6) is characterized by a basal erosion surface overlain by moderate- to high-amplitude undulating reflections. SF6 occurs mainly on top and outside SF3.

	Seismic Facies	Reflection Characteristics
SF-1	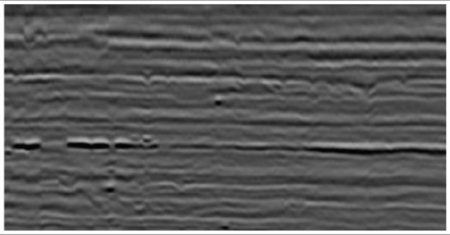	• A regional stratigraphic reflection package, bounded by erosional truncation of the subaerial unconformity. • Characterized by weak-moderate amplitude, oblique-parallel reflections dipping seaward at a low angle (up to 1°).
SF-2	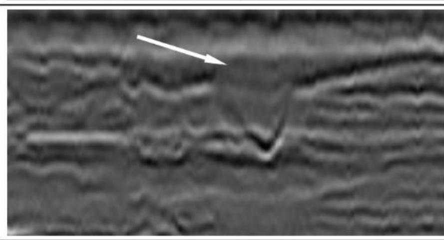	• Characterized by an infilling sequence composed of low to semitransparent amplitude, parallel, and continuous reflections arranged in aggrading packages. • Occurs only in the upper part of the U-shaped valley pattern, with onlap terminations along its walls.
SF-3	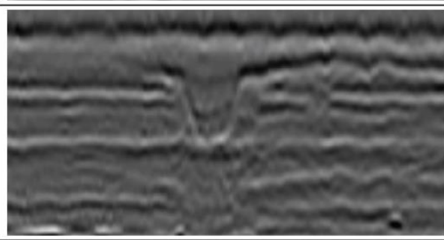	• U-shaped valley pattern above the subaerial unconformity and is overlain by chaotic to variable high-amplitude reflections. • The base is characterized by incisions, strong acoustic impedance contrast highlights the erosional truncation.
SF-4	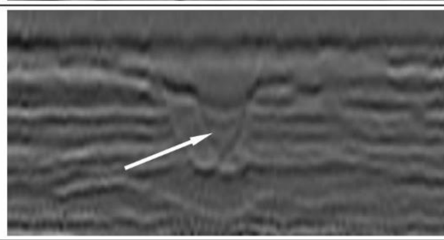	• High-amplitude, chaotic to subparallel reflections within SF4. • Predominantly forms the middle to lower part of SF4. • Incomplete SF5 units can occur at varying depths along the internal flank of SF4.
SF-5	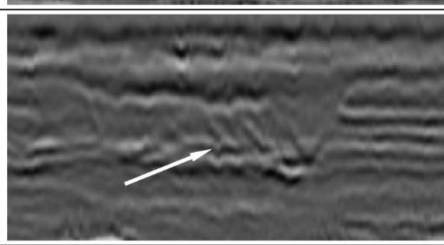	• Sigmoid to tangential-oblique parallel reflections associated with lateral accretions restricted to the lower part of SF4. • Reflections dip toward the deepest part of SF4 and are overlain by SF2.
SF-6	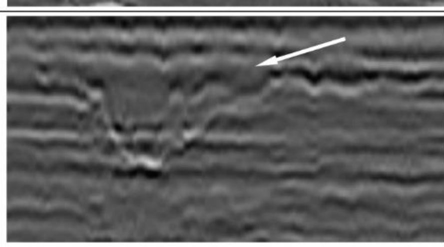	• Characterized by a basal erosion surface overlain by moderate- to high-amplitude undulating reflec-tions. • Occurs mainly on top and outside SF4.

Figure 1.4: Six seismic facies identified and their reflection characteristics.

1.5 INTERPRETATIONS

1.5.1 Seismic Sequence Stratigraphy

The studied interval comprises successive aggradational fluvial and shallow marine successions, representing the smallest identifiable seismic sequence stratigraphic unit. The diverse seismic facies are classified into genetic units corresponding to different systems tracts.

(1) Falling-Stage Systems Tract (FSST)

A forced regression driven by base-level fall produced a distinctive FSST stratigraphic architecture in the study area. FSST deposits are absent on the coastal plain and instead restricted to incised valleys above the unconformity (Figure 1.5 and Figure 1.6). Typical FSST stacking patterns, which are progradational features indicating vertical components and fluvial aggradation for horizontal components, are not observed across the seismic profiles throughout the entire study area. Instead, the FSST stage unconformity directly truncates weak-moderate amplitude parallel reflections (SF1) and is overlain by similar patterns, interpreted as vertically stacked highstand systems tracts deposition across the unconformity. U-shaped SF3 of varying scales observed on the unconformity are interpreted as incised valleys, a key FSST feature during the regression. Figure 1.5 and Figure 1.6 show typical incised valley fills in the northern and southern parts of the study area; chaotic high-amplitude SF4 reflections in the valley base are truncated downward by inclined SF5 reflections. SF4 and SF5 are interpreted as channel and point bars; the point bar's top and base dip toward the channel, indicating deposition above the base-level. The downstepping terrace morphology suggests that the channel complex formed during different stages of base-level fall. Horizontal slices through the FSST reveal diverse incised

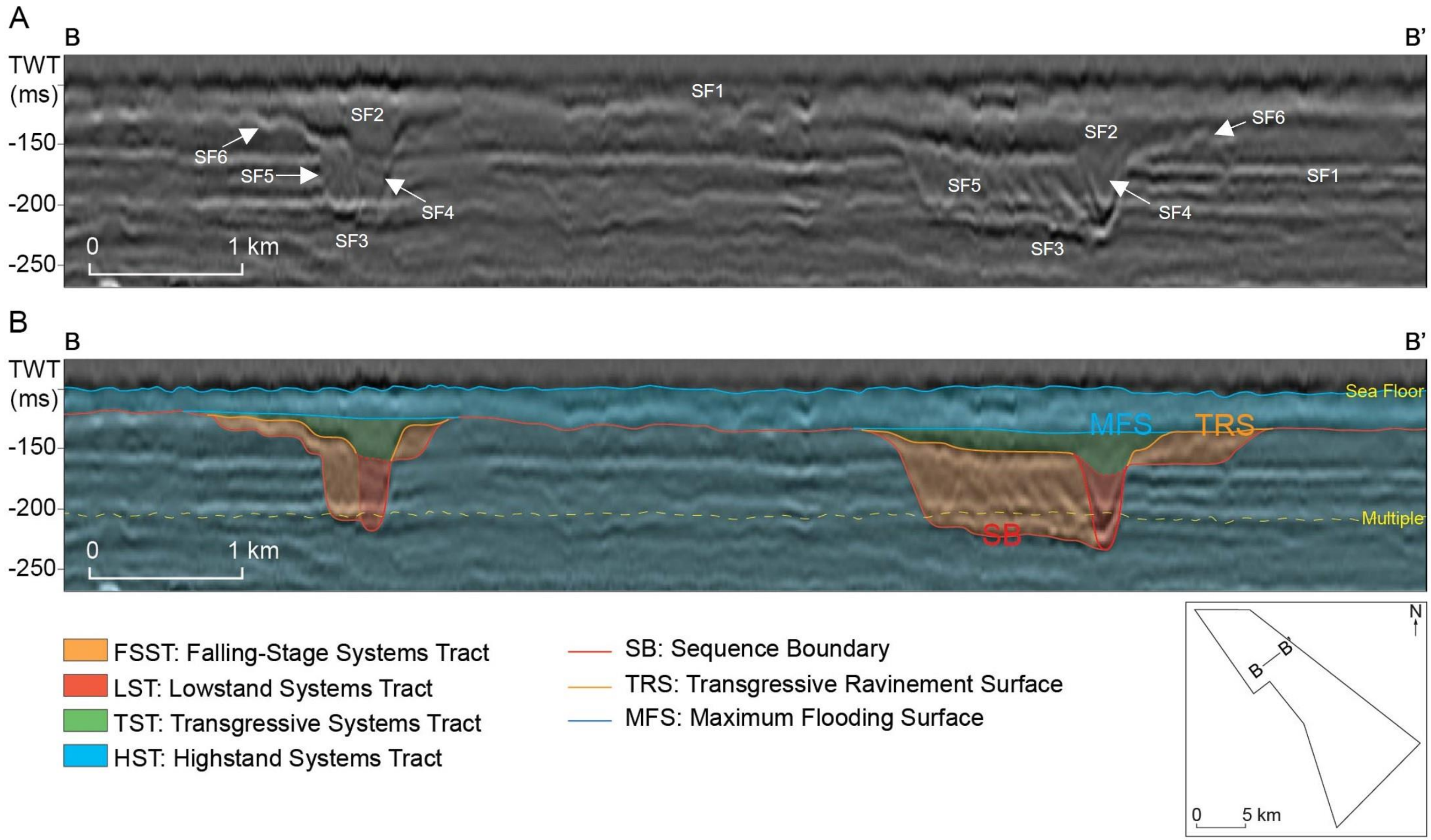

Figure 1.5: Uninterpreted (A) and interpreted (B) seismic profile in the northern part of study area showing the falling-stage systems tract (FSST), lowstand systems tract (LST), transgressive systems tract (TST), and highstand systems tract (HST) bounded by stratigraphic surfaces.

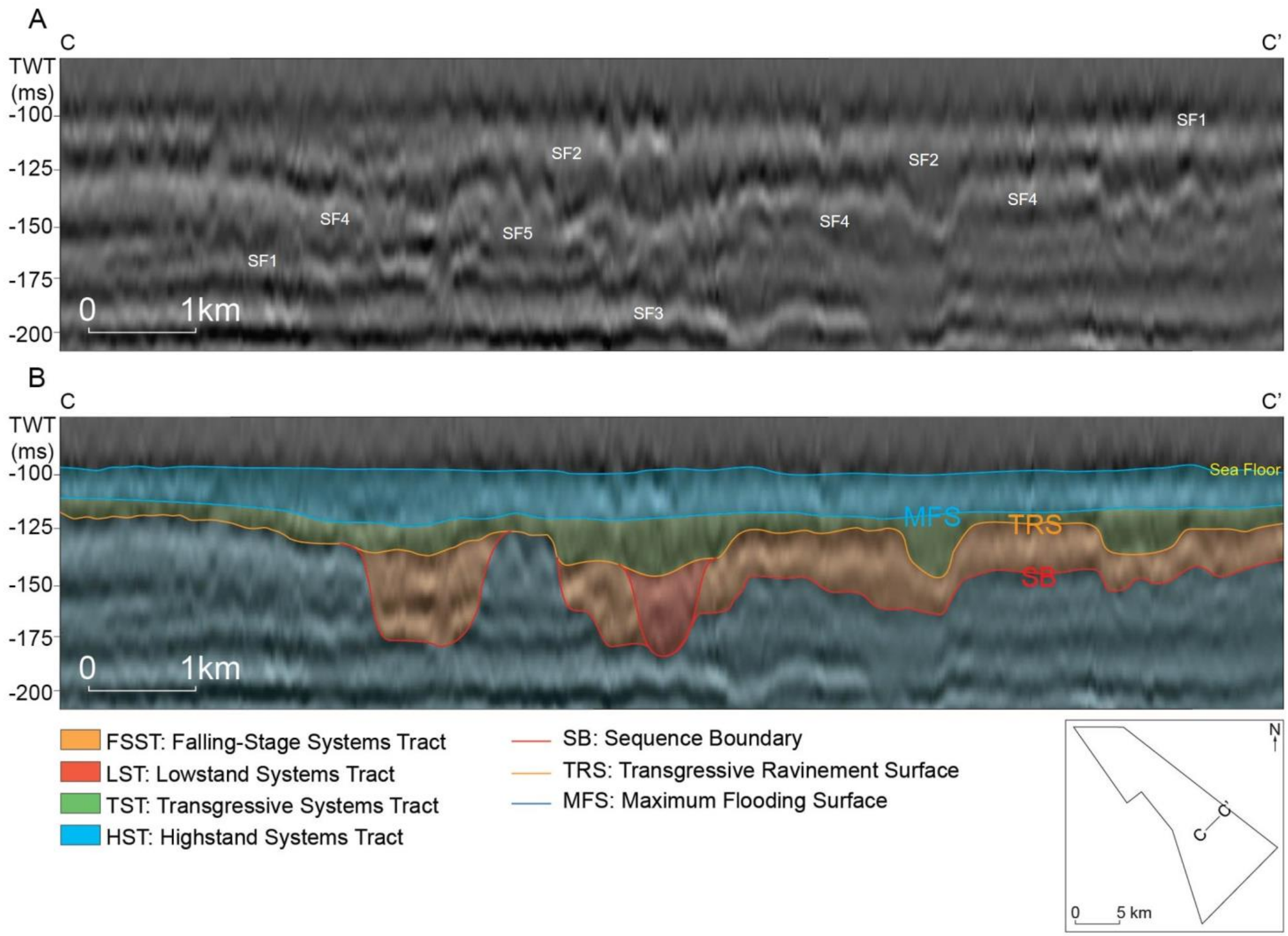

Figure 1.6: Uninterpreted (A) and interpreted (B) seismic profile in the southern part of study area showing the falling-stage systems tract (FSST), lowstand systems tract (LST), transgressive systems tract (TST), and highstand systems tract (HST) bounded by stratigraphic surfaces.

valley morphologies shaped by different styles of infilled channels. Two straight incised valleys are observed in the northern part of the study area (Figure 1.7) and a meandering one developed in the southern part of the study area (Figure 1.8).

(2) Lowstand Systems Tract (LST)

Early base-level rise and shoreline transgression halted channel incision, resulting in aggradational characteristics of LST channels within the incised valleys. In Figure 1.5 and Figure 1.6, the LST channel base lies significantly lower than the base of the point bar of FSST channel, with its lower part showing chaotic, moderate-amplitude reflections. Although genetically related to the FSST channel, the LST channel exhibits reduced cross-sectional area and shifts from lateral accretion to vertical aggradation, marking a clear transition in the depositional process. On seismic slices, LST channels appear as narrow, ribbon-shaped features embedded within the underlying strata (Figure 1.9 and Figure 1.10).

(3) Transgressive Systems Tract (TST)

The transgressive systems tract (TST), bounded by the transgressive ravinement surface (TRS) at the base and maximum flooding surface (MFS) at the top, develops primarily in low-lying areas above the unconformity during the rapid base-level rise. The TRS separates the underlying fluvial channel complex from the overlying marine deposits. Driven by tidal processes, the TRS formed on fluvial terraces within incised valleys and extended upward into interfluvial areas. Even a minor base-level rise could induce far landward shoreline migration on the low-gradient coastal plain, with transgression preferentially occupying lower topographic areas. Weak amplitude onlapping reflections of SF2 along the incised valley walls indicate marine backstepping associated with TST deposition (Figure 1.5 and Figure 1.6). Seismic slices (Figure 1.11 and Figure 1.12) reveal that the interaction between fluvial runoff and tidal processes formed jagged valley margins during the TST. Transgressive deposits over the interfluvial TRS are characterized by dendritic tributary channels that extend perpendicular to the valley margins.

(4) Highstand Systems Tract (HST)

The highstand systems tract (HST) is bounded by the MFS at the base and the seafloor reflection at the top. Continued base-level rise created accommodation for normal regression, producing parallel stacking patterns dominated by aggradation (Figure 1.5 and Figure 1.6). These patterns reflect alternating marine and non-marine successions driven by minor base-level fluctuations, with channels significantly smaller and less abundant than those in the FSST. Figure 1.13 and Figure 1.14 show horizontal slices of HST strata overlying the incised valley, where high-sinuosity, small-scale meandering patterns characterize HST channels.

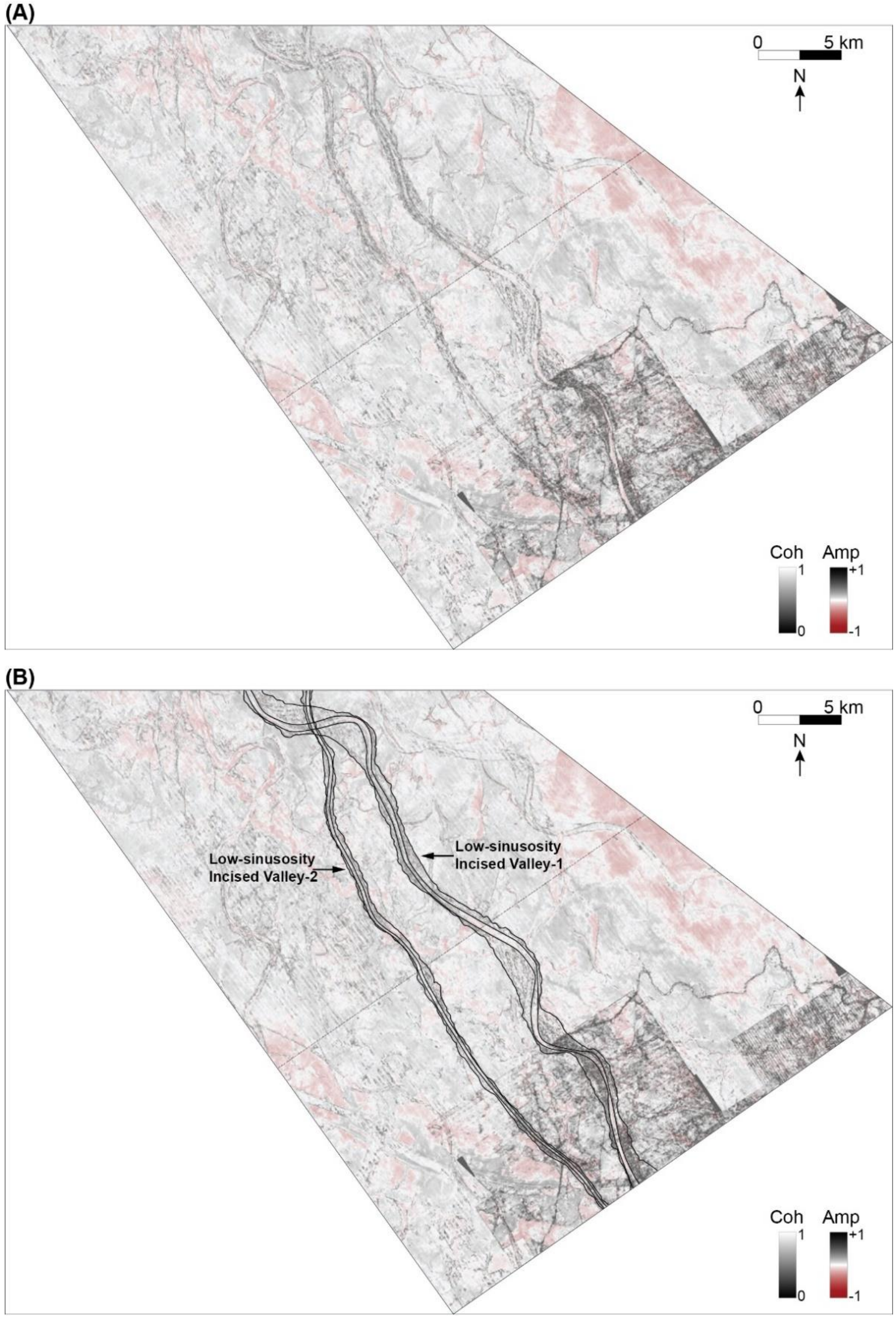

Figure 1.7: Uninterpreted (A) and interpreted (B) seismic horizontal slice through the falling-stage systems tract strata in the northern part of the study area, co-rendering seismic amplitude with coherence, shows two northwest-southeast trending low sinuous incised valleys.

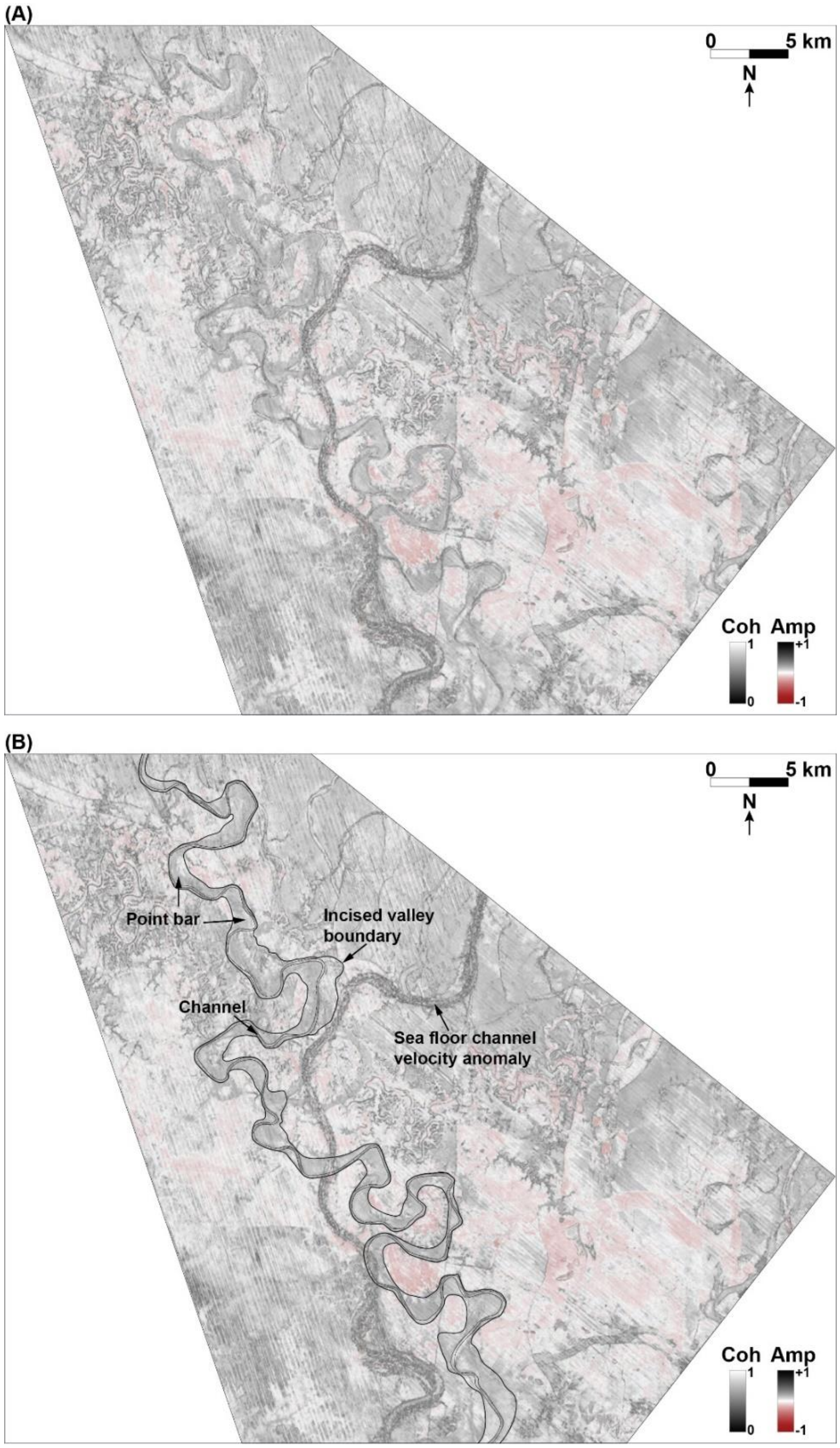

Figure 1.8: Uninterpreted (A) and interpreted (B) seismic horizontal slice through the falling-stage systems tract strata in the southern part of the study area, co-rendering seismic amplitude with coherence, shows one northwest-southeast trending high sinuous incised valley. The broad meandering channel at the center is an artifact caused by velocity anomalies associated with seafloor channel.

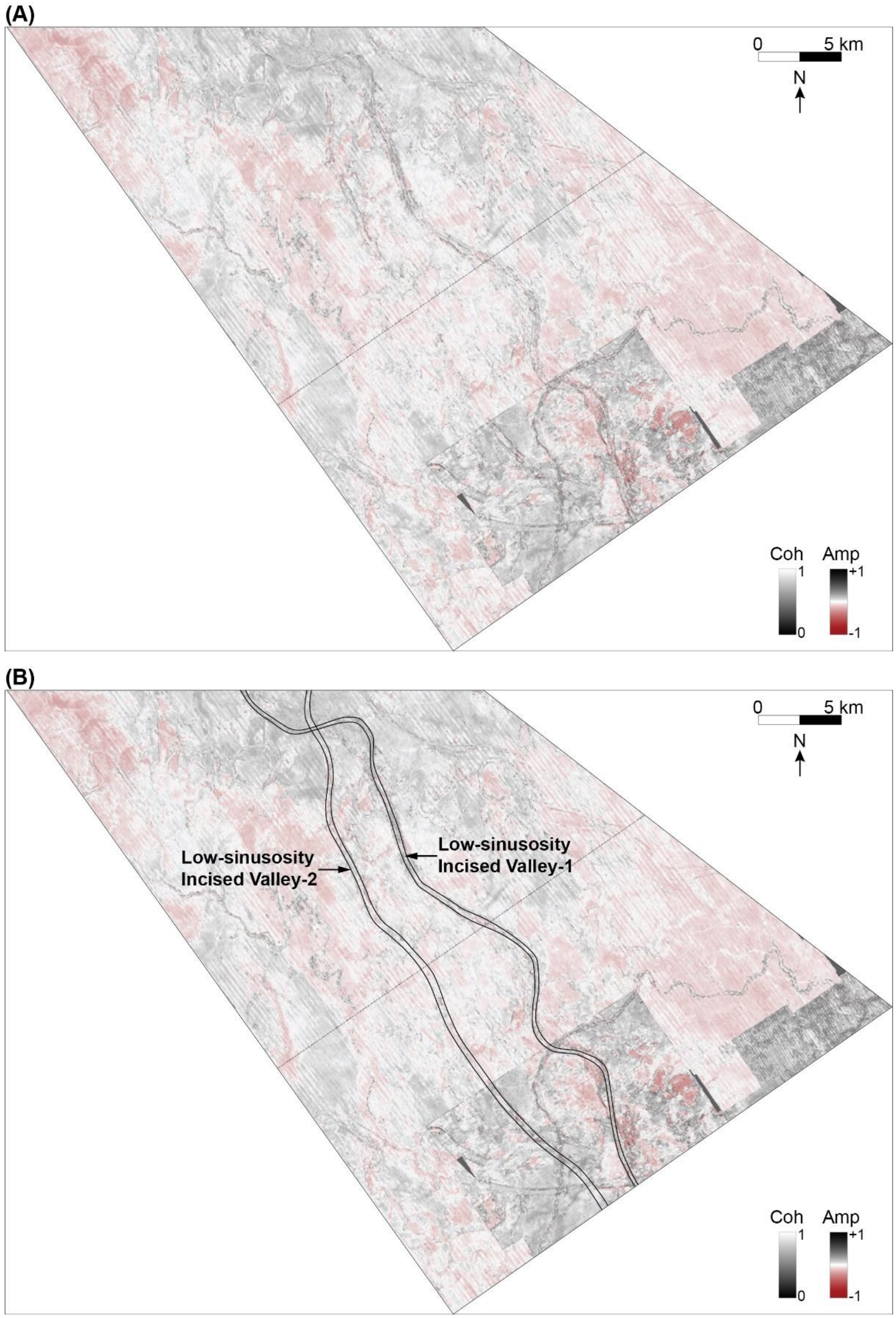

Figure 1.9: Uninterpreted (A) and interpreted (B) seismic horizontal slice through the lowstand systems tract strata in the northern part of the study area, co-rendering seismic amplitude with coherence, shows deepest part of channels within the incised valleys.

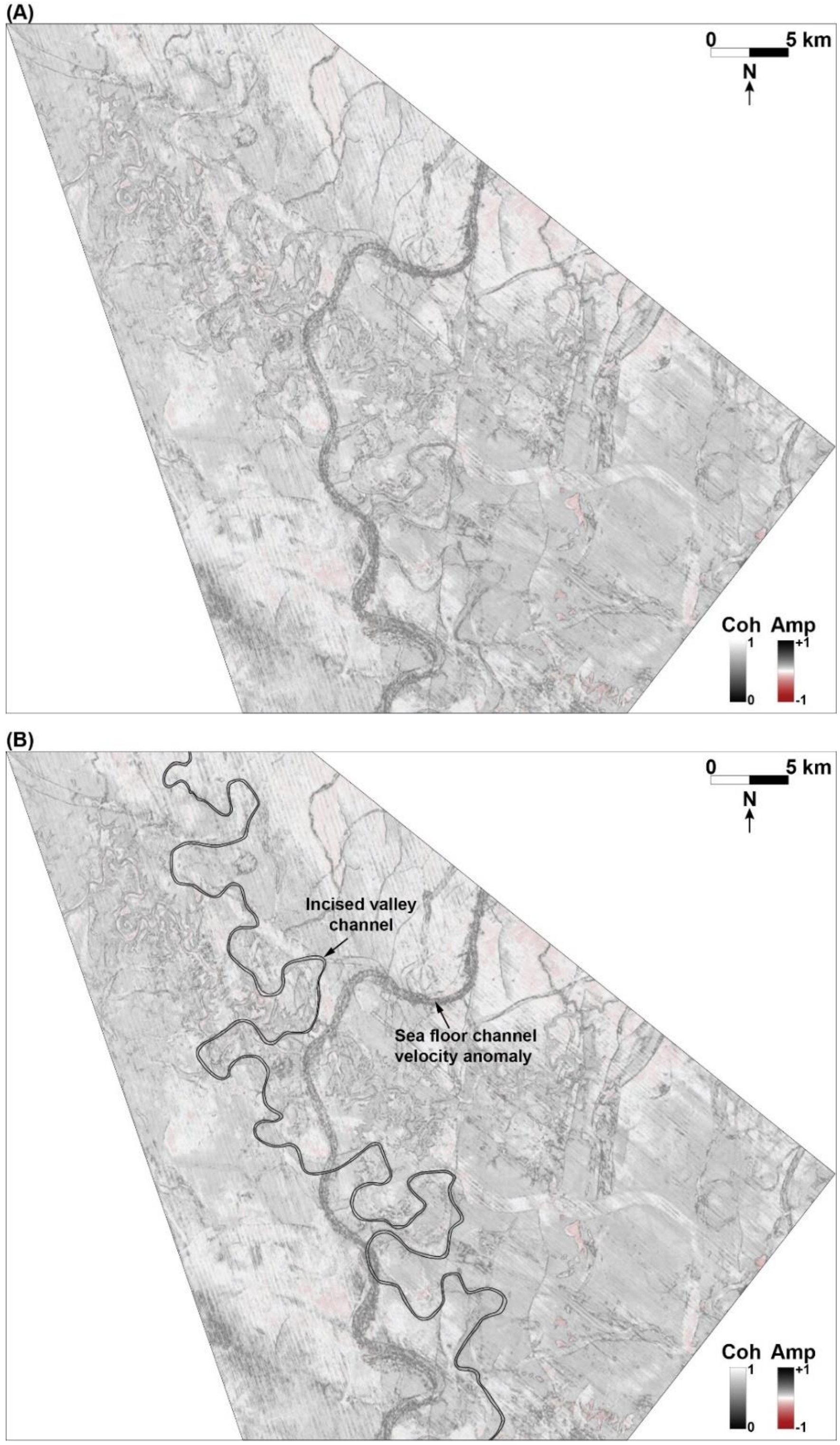

Figure 1.10: Uninterpreted (A) and interpreted (B) seismic horizontal slice through the lowstand systems tract strata in the southern part of the study area, co-rendering seismic amplitude with coherence, shows deepest part of meander channel within the incised valley.

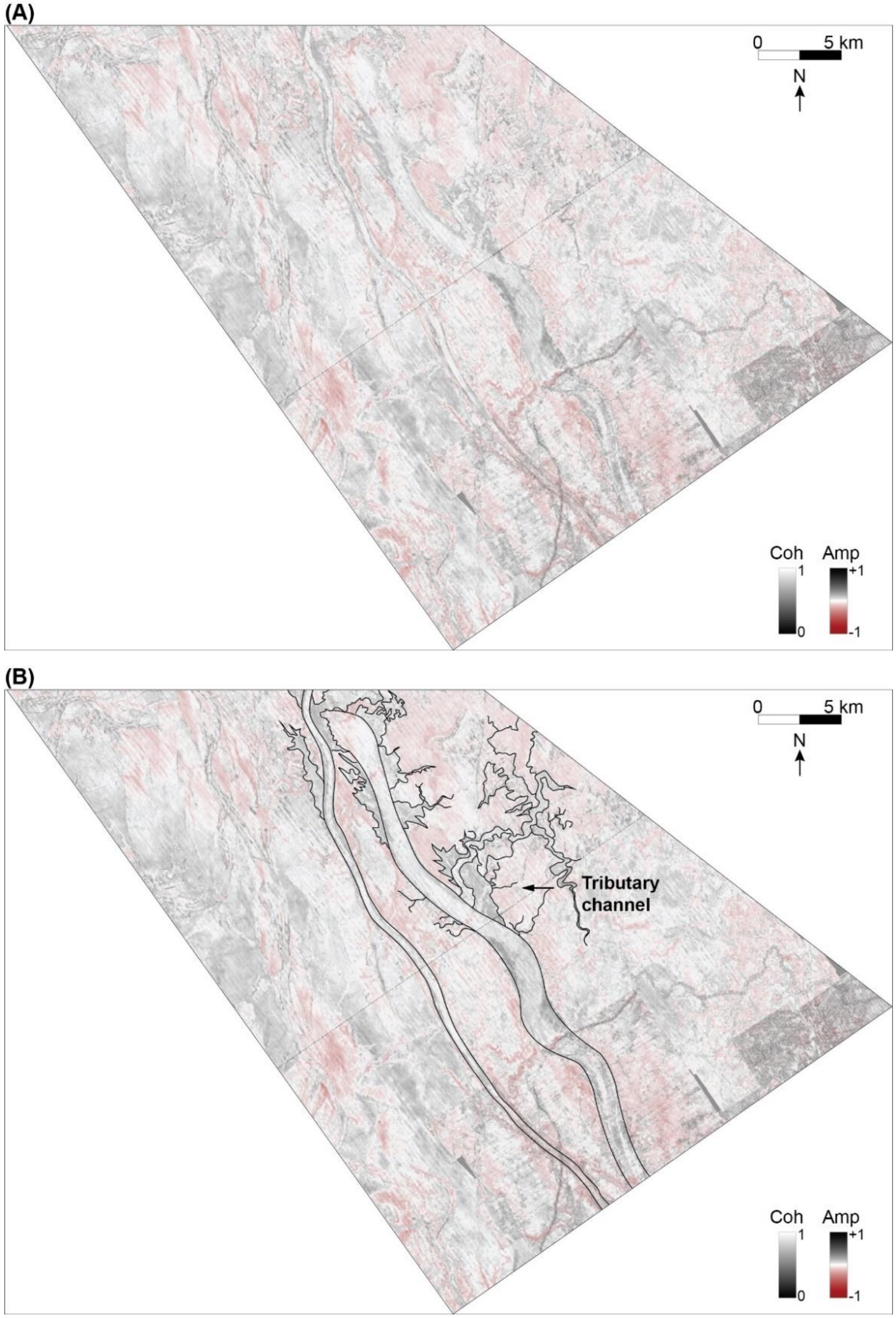

Figure 1.11: Uninterpreted (A) and interpreted (B) seismic horizontal slice through the transgressive systems tract strata in the northern part of the study area, co-rendering seismic amplitude with coherence, shows flooding channels with tidal influenced tributary channels.

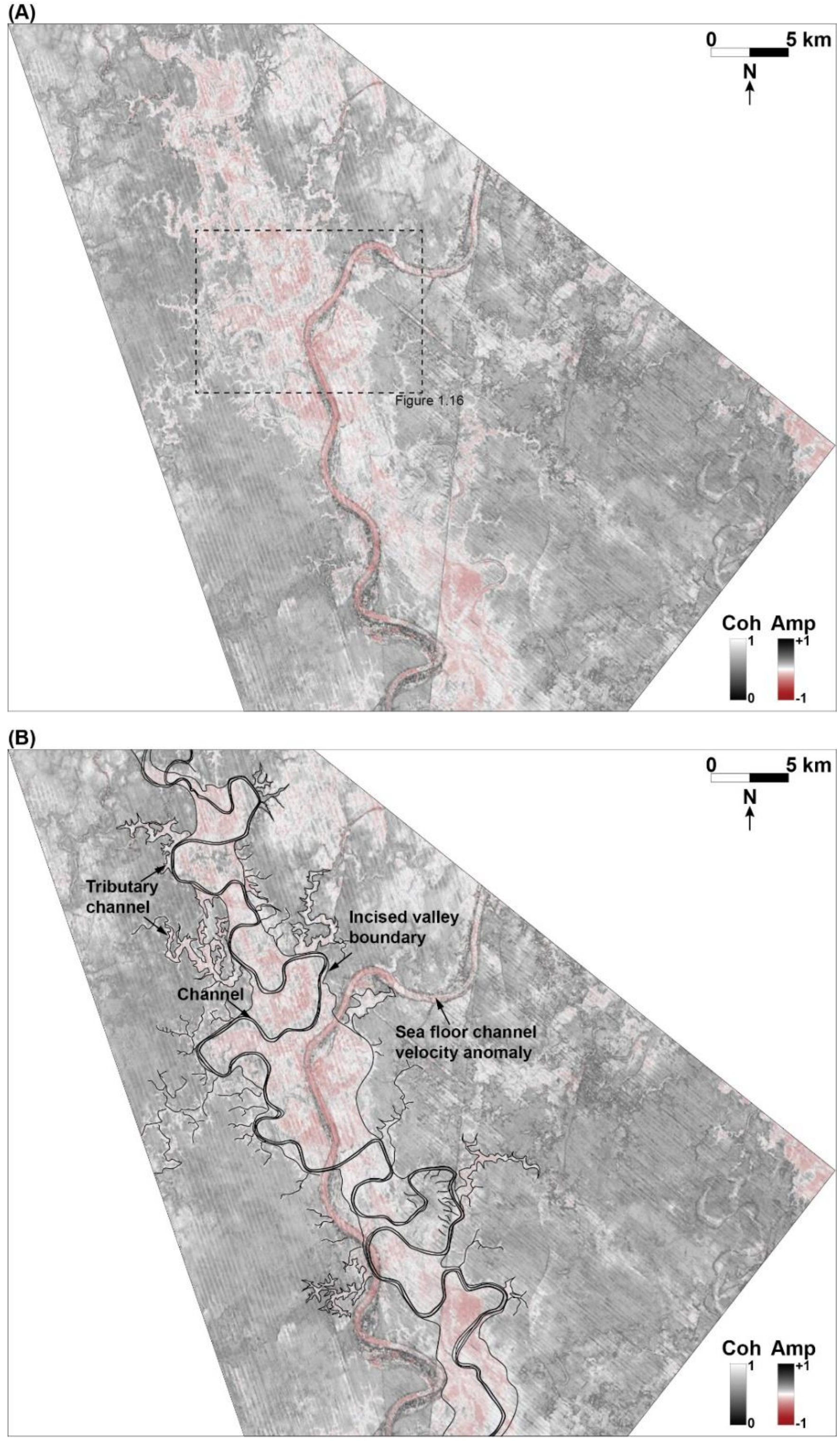

Figure 1.12: Uninterpreted (A) and interpreted (B) seismic horizontal slice through the transgressive systems tract strata in the southern part of the study area, co-rendering seismic amplitude with coherence, shows widened valley with numerous tidal influenced tributary channels.

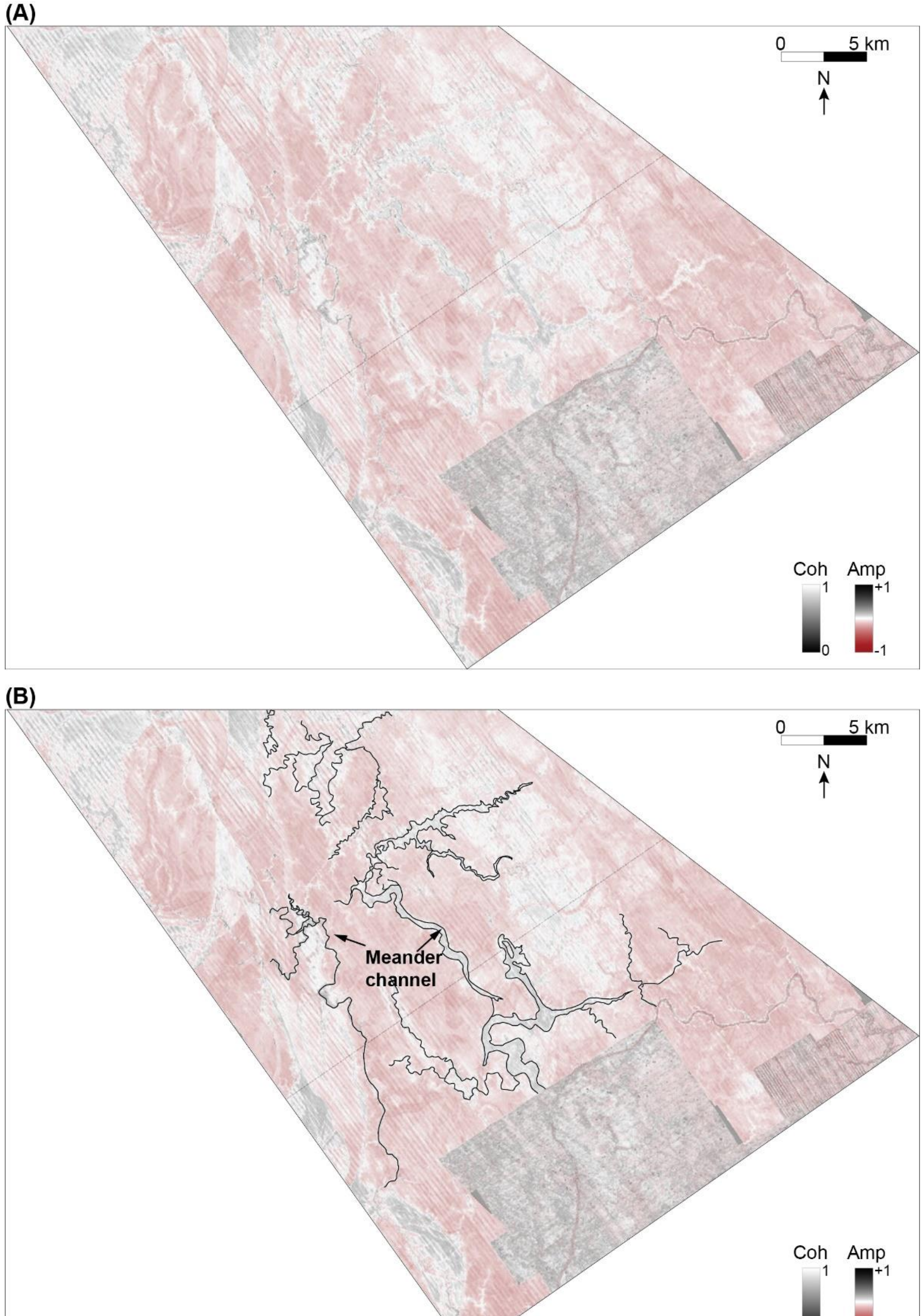

Figure 1.13: Uninterpreted (A) and interpreted (B) seismic horizontal slice through the highstand systems tract strata in the northern part of the study area, co-rendering seismic amplitude with coherence, shows small meander channels.

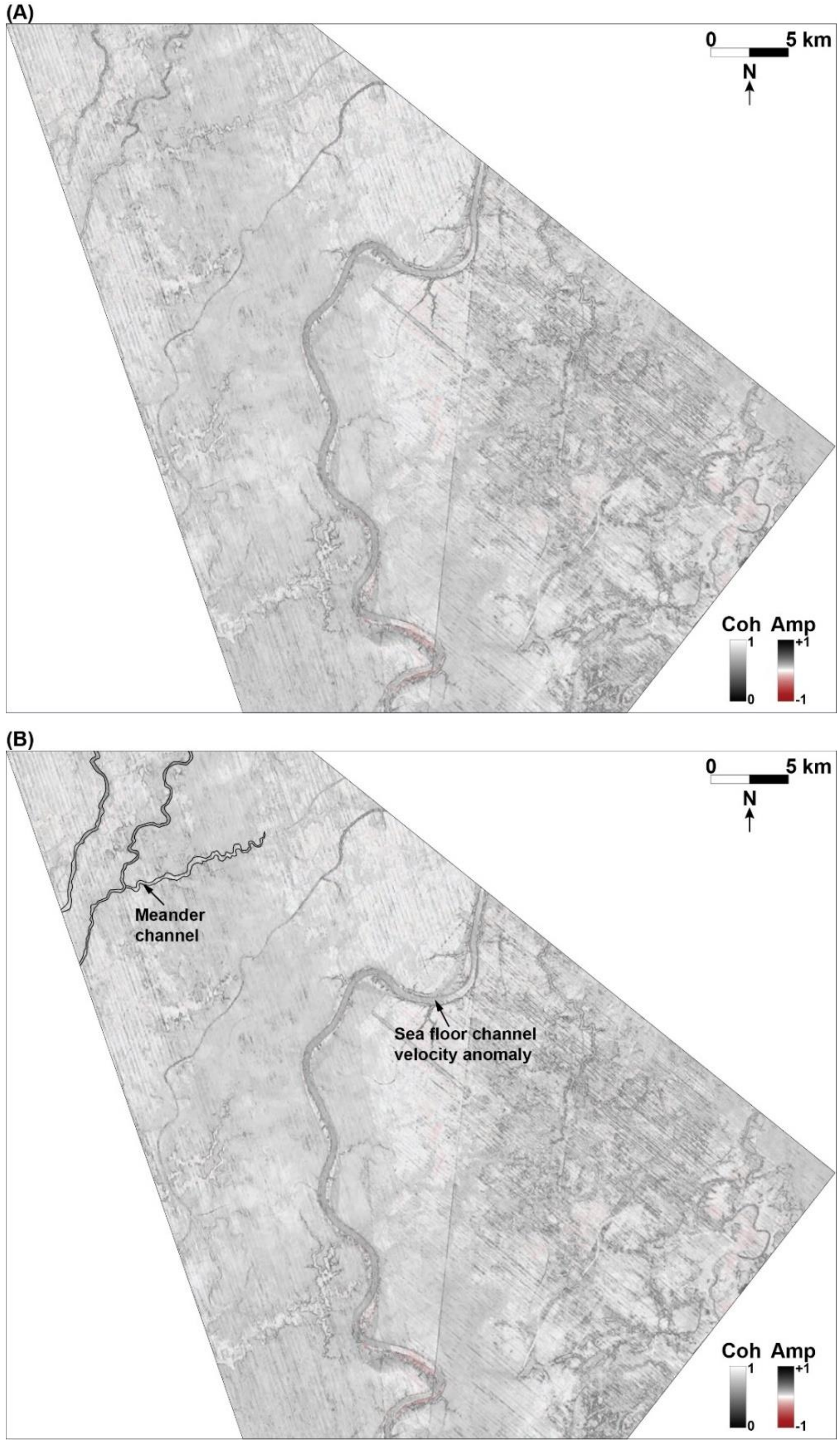

Figure 1.14: Uninterpreted (A) and interpreted (B) seismic horizontal slice through the highstand systems tract strata in the southern part of the study area, co-rendering seismic amplitude with coherence, shows small meander channels. Numerous tidal influenced tributary channels developed at the southeast corner.

1.5.2 The Incised Valleys

Three northeast-southwest trending incised valley systems within the FSST are observed at 130 ms downward, corresponding to approximately 110 m (361 ft) below the seafloor. The two northern valleys exhibit straight morphologies, while the southern valley displays a meandering pattern.

(1) Low-Sinuosity Incised Valley

Seismic profiles (Figure 1.5) show that the two northern incised valleys are deeply incised into the underlying unconformity, with inclined valley floors and steep walls. They are named LSV1 and LSV2. The valley fill comprises multiple seismic facies. The lower part is dominated by channel (high-amplitude, chaotic reflections), point bar (high-amplitude, oblique reflections), and abandoned channel (low-amplitude, transparent reflections). The upper part contains weak-amplitude, structureless reflections, interpreted as transgressive deposits. Seismic horizontal mapping (Figure 1.15) shows that both valleys are confined within sharp, linear margins. Internal channels exhibit very low sinuosity, consistent with the valley geometry. Sparse point bars developed at meander bends, exhibiting scroll bar geometries. These scroll bars are truncated upstream and converge downstream, indicating a north-to-south paleo-flow direction. Slices through the tops of point bars reveal small, shallow dendritic channels extending upstream and perpendicular to the valley margins, indicating tidal modification during transgression. Seismic facies stacking patterns suggest that the underlying unconformity strongly constrained the low-sinuosity valleys. As base-level fell, increased channel energy promoted vertical incision with minimal changes in fluvial style.

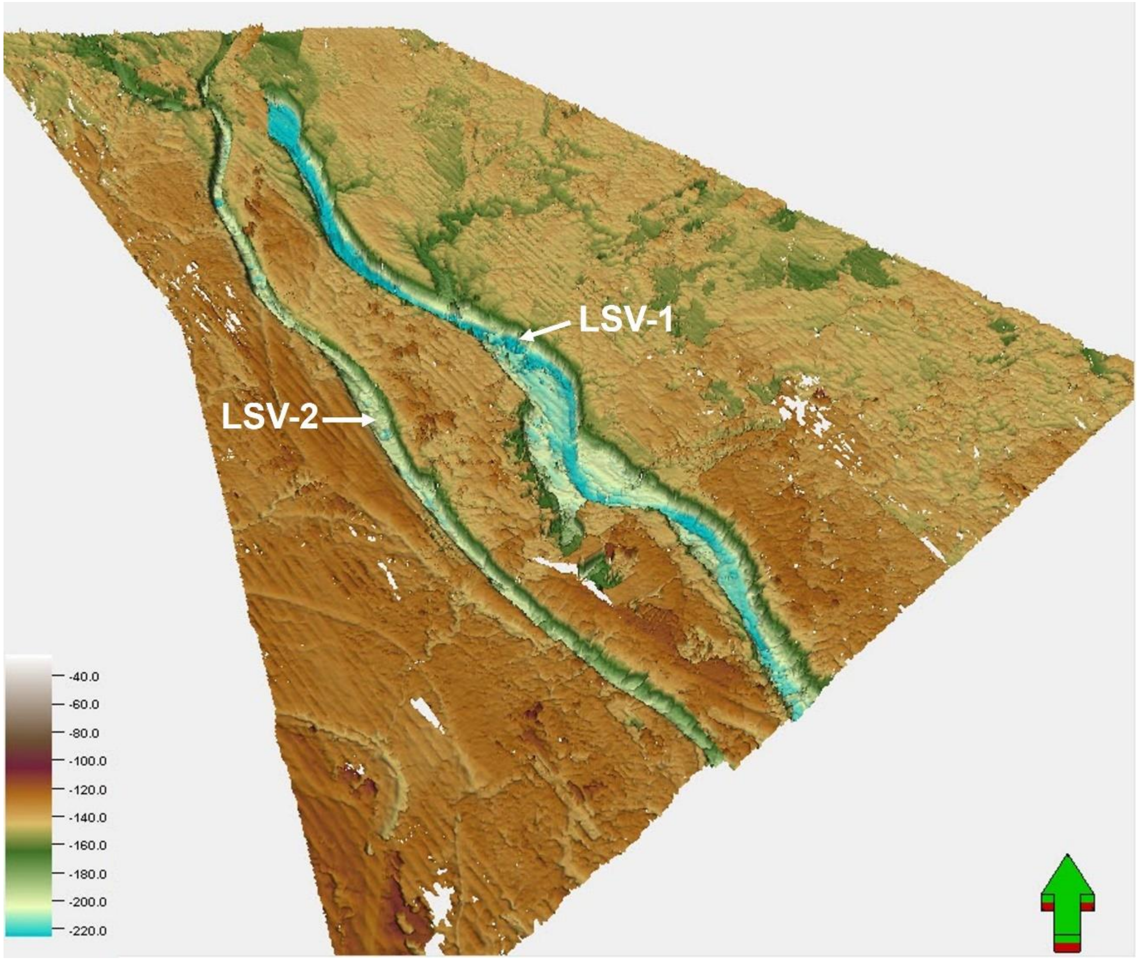

Figure 1.15: Horizontal slice along the unconformity shows that the two low-sinuosity incised valleys have steep valley walls, with channels confined within the valley boundaries.

(2) High-Sinuosity Incised Valley

In contrast, the southern incised valley is broader and filled with many meandering features, including loops and point bars. This system is referred to as the high-sinuosity incised valley (HSV). The HSV base is characterized by high amplitude, fluctuating reflections in seismic profiles (Figure 1.6). Unlike LSV1 and LSV2, HSV lacks steep valley walls, indicating that the unconformity exerted limited lateral control. The lower section is dominated by reflections of SF3 and SF6, with gently inclined tops of internal channels. The upper section contains transgressive deposits represented by continuous, low-amplitude reflections of SF2. Seismic slices (Figure 1.16) show a dominant high-sinuosity channel flanked by numerous size point bars. Valley width variation reflects the lateral expansion of meander bends, with boundaries defined by the outermost channel loops. Horizontal slices through the TST reveal small dendritic channels in interfluvial areas perpendicular to channels (Figure 1.12). The HSV's geomorphology suggests that its internal channel evolved without constraints by the erosional landscape at the initial stage, enabling dynamic adjustment to flow energy. During base-level fall, the channel retained its inherited meandering pattern, with lateral expansion transitioning into a dominant vertical incision.

(3) The Difference Between the Two Types of Incised Valleys

LSV1 and LSV2 each extend approximately 45 km, whereas HSV spans up to 55 km across the study area. Although all three incised valleys formed during the same FSST stage exhibit distinct morphological characteristics, Figure 1.17 presents representative seismic profiles illustrating the internal architecture of the three incised valleys, with their quantitative differences summarized in Table 1.1.

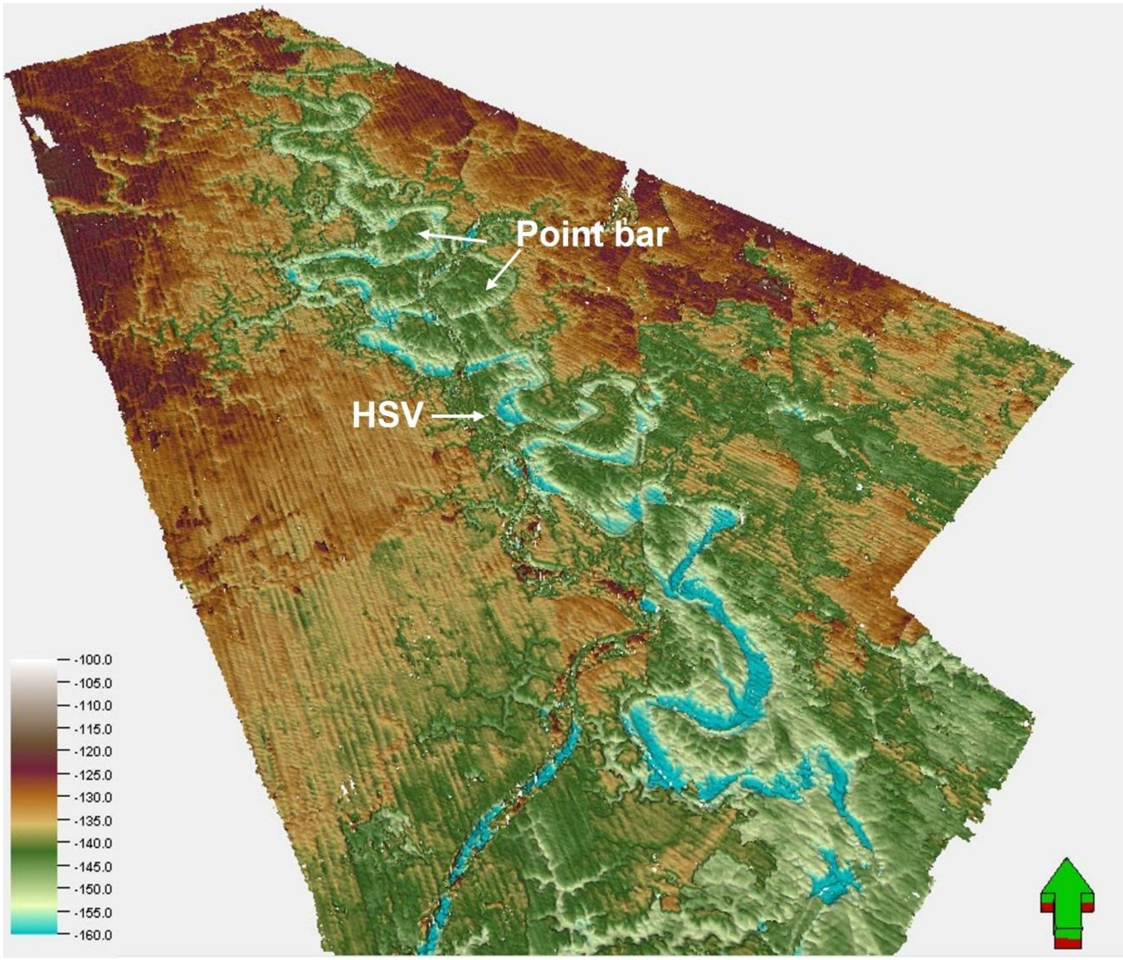

Figure 1.16: Horizontal slice along the unconformity shows that the valley exhibits a high-sinuosity morphology due to the development of meandering channels, which are characterized by numerous point bars.

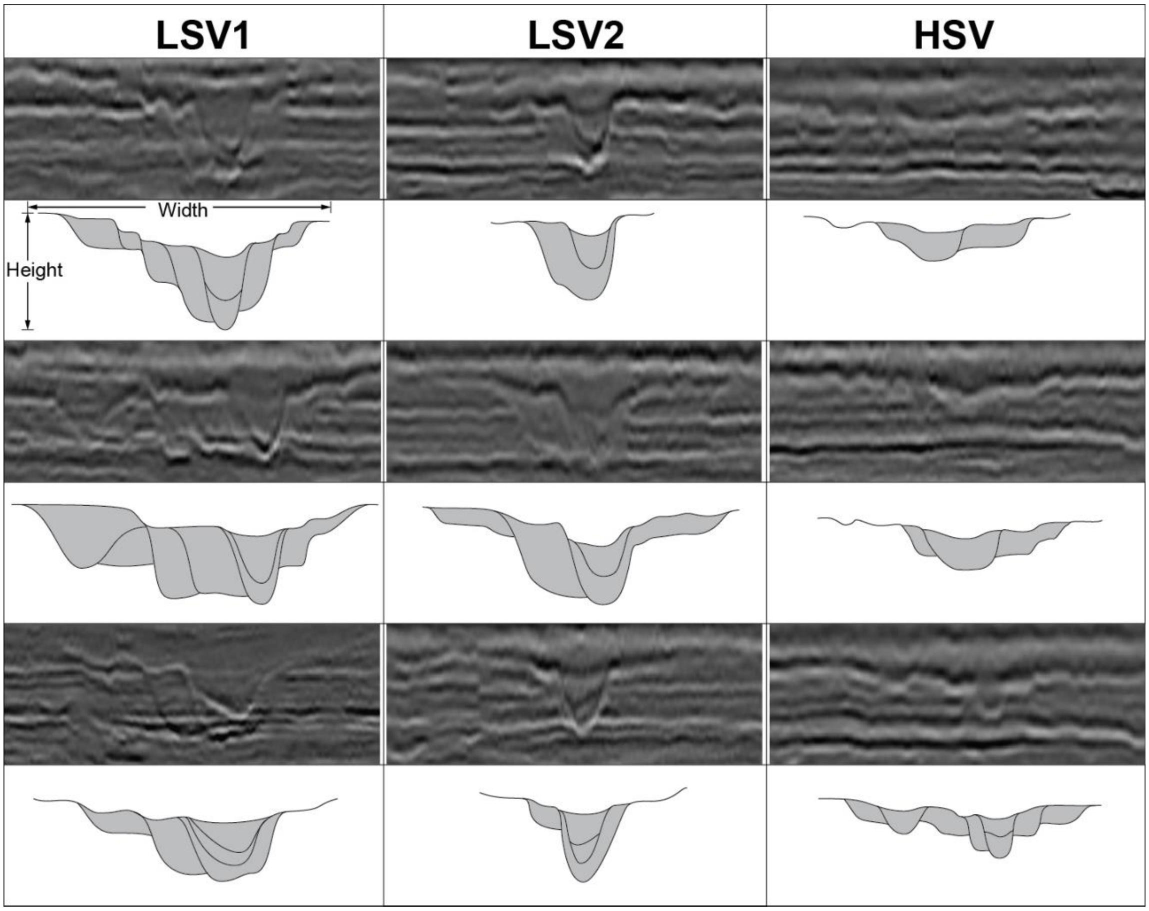

Figure 1.17: The typical cross-sectional morphologies of the three incised valley fills. All exhibits terraced channel deposition features dipping inward into the valley.

Table 1.1: Quantitative geometric characteristics of the three incised valleys.

	Depth (m)		Height (m)		Width (m)		Aspect ratio	Drain area (km^2)
	Min.-Max.	Avg.	Min.-Max.	Avg.	Min.-Max.	Avg.		
LSV1	106.3-119.0	111.8	77.4-86.7	80.6	1280-2100	1565	15-26	621
LSV1	85.0-103.7	95.5	62.9-74.8	68.3	620-1050	736	8-15	418
HSV	56.1-71.4	61	27.2-39.1	37.2	1062-7940	3550	31-202	791

The thalweg of LSV1, defined as the lowest point on the valley's erosional base, ranges from 225 to 240 ms, approximately 106-119 m (349-390 ft) below the sea floor (BSL). The thalweg reaches the deepest point within the straight channel segment, and the valley walls are steepest. Its shallowest point occurs at the meander bend due to increased deposition. LSV2's thalweg fluctuates slightly between 200 and 222 ms, approximately 85-104 m (279-340 ft) BSL, consistent with its low-sinuosity (<1.1), near-linear morphology. In contrast, HSV's thalweg ranges from 166 to 184 ms, approximately 56-71 m (184-234 ft) BSL, with a consistent downstream deepening trend.

The height of LSV1, measured from the valley base to its upper margin, ranges from 45.5 to 51 ms, corresponding to 77.4-86.7 m (253.8-284.4 ft), peaking in the straight channel segment in line with the thalweg depth. LSV2's height ranges from 74 to 84 ms, approximately 62.9-74.8 m (206.4-245.4 ft), lower than LSV1 due to its shallower thalweg despite similar top surface depth. HSV's height ranges from 32 to 46 ms, approximately 27.2-39.1 m (89.2-128.3 ft), with minimum values in the most sinuous segments (sinuosity = 5) and increasing gradually downstream.

The width of LSV1 ranges from 1,280 to 2,100 m (4,199 to 6,890 ft), reaching a maximum at the meander bend. LSV1 drains an area of approximately 621 km^2 (240 mi^2). LSV2, characterized by a highly low-sinuosity internal channel, has minimal width variation between 620 m to 1,050 m (2,034 ft to 3,445 ft). It drains an area of approximately 418 km^2 (161 mi^2). In contrast, HSV shows substantial width variation, from 1,062 m to 7,940 m (3,484 to 26,050 ft), with an average width of 3,550 m (11,647 ft). It reaches a maximum width in areas where channel migration causes diversion. HSV drains an area of approximately 791 km^2 (305 mi^2).

The aspect ratio (width/height) of LSV1 ranges from 15 to 26, peaking at the meander bend. LSV2's aspect ratio ranges from 8 to 15, with an average of 11 and minimal variation. The maximum value of 15 occurs in a slightly sinuous segment. HSV's aspect ratio varies widely from 31 to 202, with several peaks corresponding to valley widening driven by lateral channel migration. The aspect ratios of the three incised valleys follow trends similar to channel width, indicating that valley width, rather than height, is the primary control of the aspect ratio.

1.6 DISCUSSION

1.6.1 FSST: A Missing Link in The Array of Systems Tracts

The FSST is defined by a forced regression stacking pattern formed during shoreline regression. It is bounded at the base by the forced regressive marine surface and at the top by a subaerial unconformity (Hunt and Tucker,1992; Ainsworth, et al., 1994; Plint and Nummedal, 2000; Plint et al., 2001). Although the studied stratigraphic interval developed on the coastal plain consists of alternating shallow marine and non-marine successions, the sequence stratigraphic framework does not conform to this idealized sequence stacking model. Notably, the response to base-level fall differs between interfluvial and intrafluvial areas.

In the interfluvial areas, diagnostic features of the FSST, which are typically expressed as offlapping stacking patterns at the top of the prograding package formed during successive base-level falls, are absent in seismic profiles across broad regions. Instead, the subaerial unconformity directly overlies the HST. This unconformity is characterized by erosional truncation of the underlying strata and irregular, small-scale topographic relief (Figure 1.18A). Horizontal slices along the unconformity surface confirm that these subtle topographic variations correspond to small-scale channels outside major incised valleys. These minor channels display dendritic patterns characteristic of tidally influenced tributary systems (Figure 1.18B). Such features suggest that the unconformity was reworked by transgressive erosion. As tidal processes advanced landward across the low-gradient interfluvial landscape, they modified the unconformity into a transgressive ravinement surface (TRS). The resulting amalgamation of the unconformity and the TRS forms a composite stratigraphic surface. Above this composite

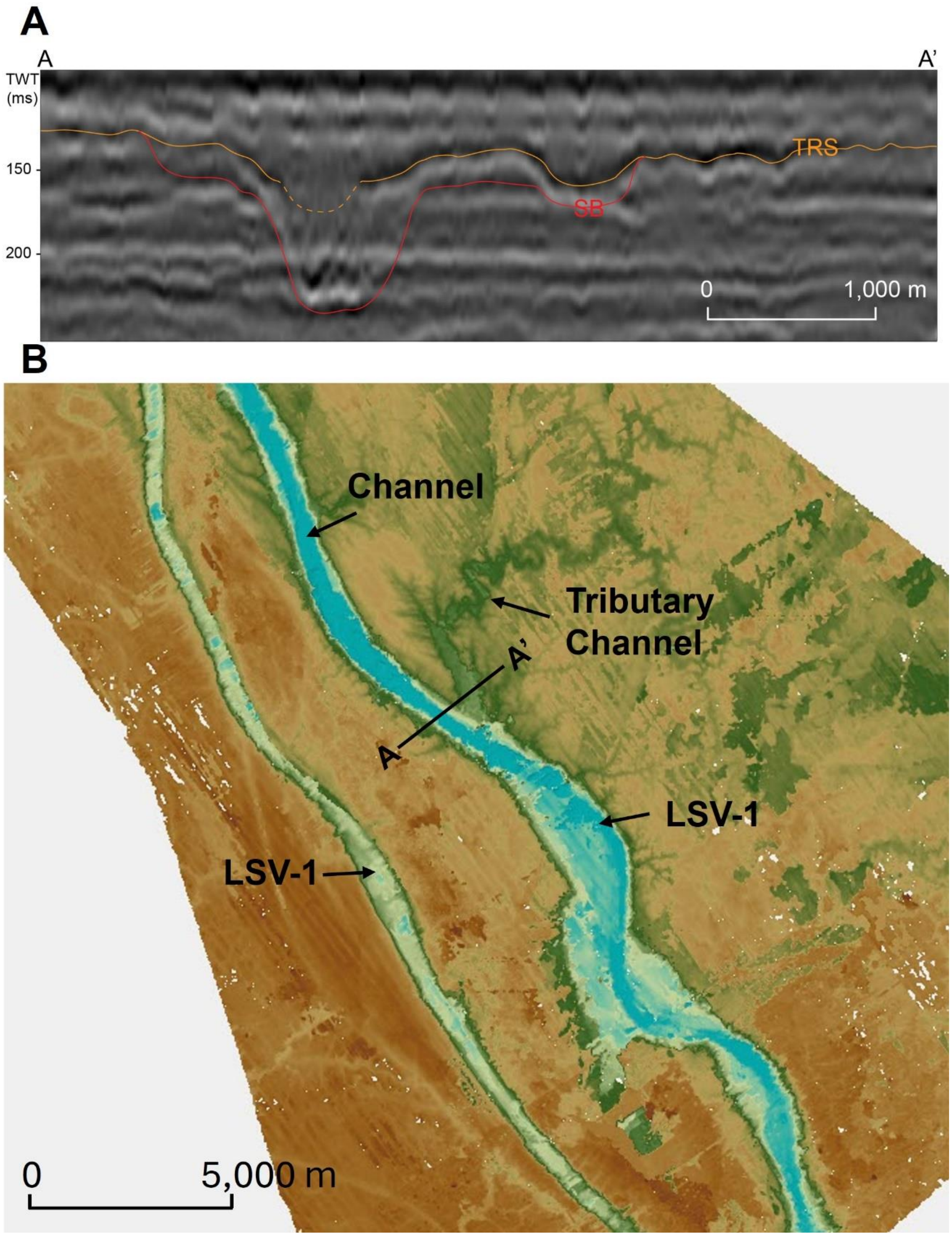

Figure 1.18: (A) In the interfluvial area, the subaerial unconformity merges with the transgressive ravinement surface to form a composite stratigraphic surface. (B) Horizontal slice reveals that this composite surface is overlain by tidal-influenced distributary channels.

surface, large fluvial channels are notably absent, and the weak impedance contrasts sharply with surrounding reflections, indicating that returning marine conditions allowed marine sediments to infill and occupy previously TRS. Consequently, the FSST appears as a missing link within the succession of systems tracts in the interfluvial zone of the coastal plain.

In intrafluvial areas, the expression of base-level fall is relatively subtle and is preserved within the fluvial strata above the subaerial unconformity as discontinuous fluvial terraces. These terraces are interpreted as evidence of staged deposition during FSST. According to sedimentological studies (Snedden et al., 1992; Muto and Steel, 2001, 2004; Anderson et al., 2004), prolonged base-level fall is required to generate significant fluvial incision and sediment bypass, during which stepwise fluvial accumulation may be preserved as terraces that survive subsequent transgression. Within incised valleys, the morphology of these terraces is identifiable in seismic profiles by sharp reflection contrast, particularly where transgressive deposits overlie underlying fluvial features such as channel-fill facies or point bars. These terraces commonly display a stepwise downcutting geometry that marks a regressive surface of fluvial erosion formed through successive episodes of channel incision during base-level fall (Figure 1.6 and Figure 1.17). During the ensuing transgression, tidal ravinement processes partially reworked this erosional surface, producing a composite stratigraphic surface of TRS and erosional surface. This composite surface is especially evident in seismic slices through point bar tops, where tidal reworking is expressed as short, closely spaced scours oriented perpendicular to adjacent channels (Figure 1.19). Additionally, the low-gradient topography of the study area enabled fluvial systems to respond rapidly to minor base-level falls. These adjustments follow the pattern

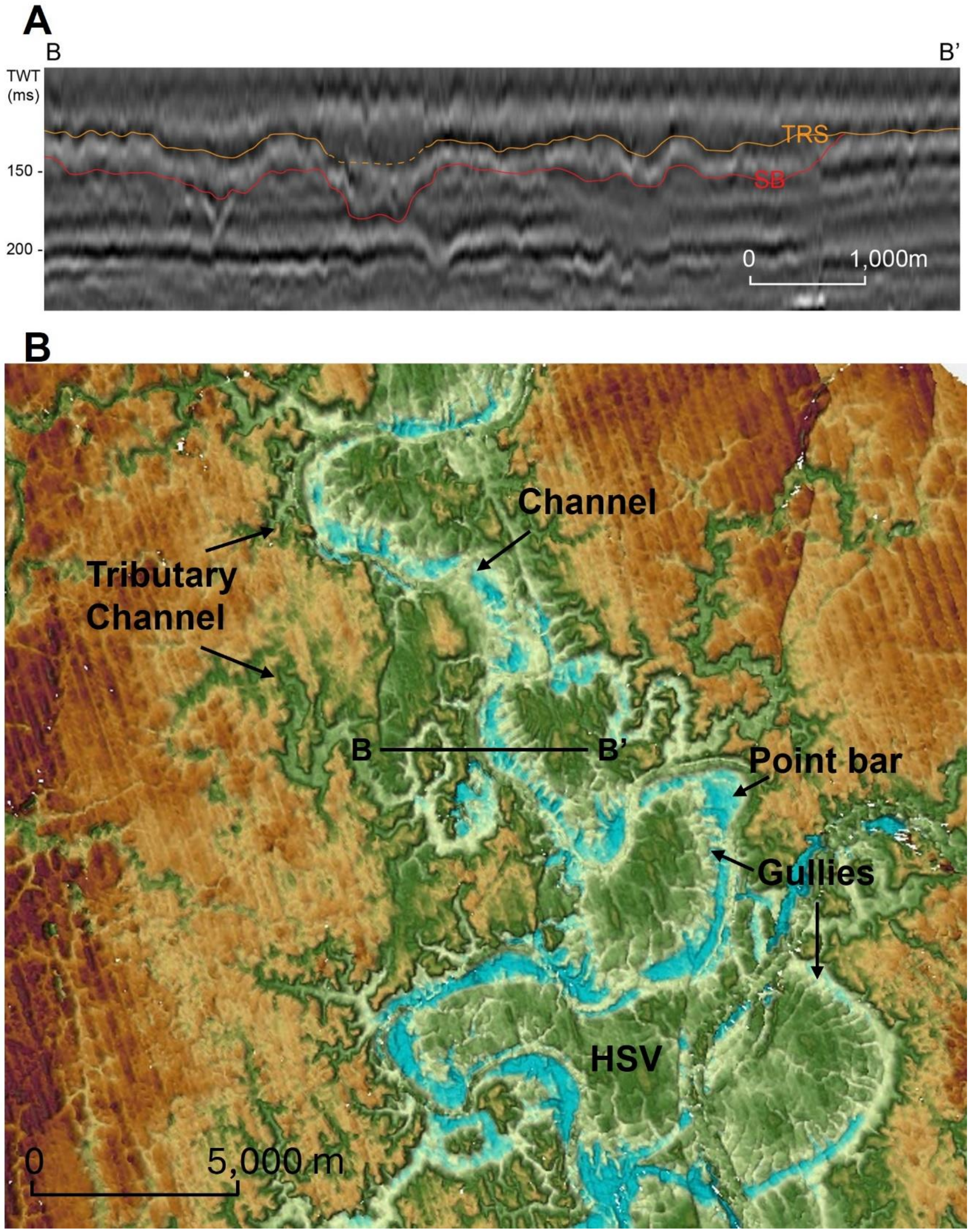

Figure 1.19: (A) In the intrafluvial area, the transgressive ravinement surface developed on the tops of channel deposits is overlain by transgressive marine sediments. (B) Horizon slice reveals that this surface is characterized by tidal-influenced distributary channels and gullies on the tops of point bars.

of the Pleistocene-Holocene sea-level curve (Waelbroeck et al., 2002), which depicts a slow, stepwise fall followed by a rapid rise. Although the exact geological age of these incised valleys is uncertain, their terrace characteristics are consistent with this sea-level pattern. Studies of Quaternary incised valleys on the Sunda Shelf (Hanebuth et al., 2003; Alqahtani et al., 2015, 2017; Twarog et al., 2021; Wetzel et al., 2021) also suggest their formation and infill resulted from glacially driven sea-level changes (approximately 120 m below present), with valley filling occurring during slow, stepwise fall followed by a subsequent rise. The terraced channel deposition preserved between the unconformity and terraces reflects the combined effects of erosion, deposition, and rework associated with base-level fall and subsequent rise. Incised valleys preserve a complete succession of systems tracts in which terraced channel deposits stratigraphically correspond to the missing FSST record in interfluvial areas.

1.6.2 Two Distinct Incised Valley Types Within the FSST

Within the same FSST stage, two straight, deeply incised valleys and one high-sinuosity valley are observed in the study area. The high-sinuosity incised valley is interpreted as inherited morphology from highstand fluvial channels and a relatively proximal location to the paleo-estuary. During the FSST stage, a significant base-level fall caused the channel into a geomorphic disequilibrium in fluvial systems, leading to rapid channel incision (Castelltort and van den Driessche, 2003; Clift, 2006). Low-sinuous incised valleys, LSV1 and LSV2, in the northern part of the study area follow the typical model of initially forming as narrow, straight channels that later deepen and widen (Schumm, 1981). In contrast, high-sinuous incised valley HSV in the southern area exhibits a distinct high-sinuosity pattern that deviates from the conventional model. Given the study area's gentle topography, the HSV is interpreted as an inherited feature from meandering channels formed during the highstand systems tract. During the base-level rise, a gentle coastal plain topography is re-established, providing favorable conditions for the development of high-sinuosity channels (Blum and Törnqvist, 2000; Posamentier, 2001; Blum et al., 2013; Manshor et al., 2022). Seismic slices (Figure 1.13 and Figure 1.14) indicate that fluvial systems in the highstand systems tract are characterized by high-sinuosity meandering channels, typically associated with low-energy depositional environments. Base-level fall induces changes in river gradient and energy, promoting channel incision into the coastal plain and forming incised meander belts that retain the meandering morphology characteristic of highstand systems tract channels. This interpretation is supported by seismic observations showing that lowstand systems tract channels' base lies below the base of adjacent point bars (Figure 1.5). Moreover, there are no frequent channel diversions, and almost all point bars were not subjected to neck cut-off within HSV suggesting that the meandering pattern formed during stable relative sea-level fall stages. Therefore, HSV reflects a continuous evolutionary trajectory inherited from the preceding highstand systems tract.

Another possible explanation for HSV formation is its closer spatial proximity to the estuary relative to LSV1 and LSV2. Facies models (Van Wagoner et al., 1990; Zaitlin et al., 1994; Boyd et al., 2006) and studies of modern incised valleys (Hanebuth and Stattegger, 2004; Reijenstein et al., 2011; Dalrymple et al., 2012; Gugliotta and Saito, 2019) indicate that high-sinuosity channels in an incised valley tend to form upstream of tide-dominated channel mouths or bedload convergence zones with increased sediment loads. HSV exhibited significantly more numerous dendritic tributary channels, indicative of tidal drainage patterns, than LSV1 and LSV2. However, no progradational reflections suggesting deltaic deposits or funnel-shaped channels indicative of estuarine settings were observed in the study area. These characteristics suggest that all incised valleys remained upstream of the estuary, with HSV located closer to the estuarine zone than LSV1 and LSV2. The extensive development of point bars in HSV supports this interpretation. Therefore, HSV's high-sinuosity morphology is best explained as an inherited feature from highstand meandering channels preserved during base-level fall, further influenced by its closer proximity to the paleo-estuary than LSV1 and LSV2.

1.7 LIMITATIONS

The seismic dataset used in this study comprises seven surveys acquired at different times. Two major issues in the shallow seismic data pose significant challenges for accurate interpretation. The first issue involves shallow multiples. A prominent water-bottom multiple, observed at approximately 250 ms in several surveys, mirrors the seafloor reflection. This multiple can obscure real seismic events, distort amplitudes, and significantly degrade data quality (Figure 1.5). The second issue involves velocity anomalies caused by seabed accumulations. Localized low-velocity zones from seabed deposits can create a "push-down" effect on underlying reflections. This effect distorts the vertical positioning of seismic events, creating an illusory sinuous pattern in successive seismic slices (Figure 1.8). Together, these issues critically impact seismic data quality. They can easily result in erroneous geological interpretations without careful attention during processing and interpretation.

1.8 CONCLUSIONS

The Falling-Stage Systems Tract (FSST) is a missing link of the systems tracts within the Pleistocene succession of the North Malay Basin. The FSST strata are absent in interfluvial areas, where the subaerial unconformity is directly overlain by highstand deposits, a more complete FSST record is preserved within incised valley systems. This finding highlights the differential preservation potential of FSST elements in low-gradient coastal plain settings.

The FSST is effectively missing in interfluvial area due to the amalgamation of the subaerial unconformity with a transgressive ravinement surface. This composite surface, shaped by tidal reworking during early transgression, masks the original regressive architecture, resulting in the absence of diagnostic FSST stacking patterns typically observed in continental margin settings.

In contrast, incised valleys provide a stratigraphically complete record of the FSST, manifested as terraced channel fills and stepped erosional surfaces. These features are interpreted as the result of episodic fluvial incision and limited aggradation during prolonged base-level fall, followed by tidal reworking during subsequent transgression. The valley fills thus serve as key repositories for reconstructing the FSST in coastal plain environments.

Two morphologically distinct types of incised valleys are identified. Low-sinuosity valleys (LSV1 and LSV2) exhibit deeply incised, straight to slightly sinuous geometries, indicative of high-energy incision under confined conditions. The high-sinuosity valley (HSV) preserves a meandering morphology, interpreted as inherited from pre-existing highstand fluvial systems. Its limited lateral confinement and proximity to the paleo-estuarine zone facilitated the retention of its sinuous planform during subsequent incisions. The observed variability in incised valley morphology and internal architecture reflects a complex interplay among antecedent topography, fluvial dynamics, sediment supply, and base-level history. In particular, the HSV morphology underscores the influence of inherited channel geometry and proximity to the paleo-estuary in enhancing tidal reworking and point bar development during transgression.

ACKNOWLEDGMENTS

We gratefully acknowledge PTT Exploration and Production Public Company Limited (PTTEP) for providing the data used in this study and granting permission to publish the findings. We also acknowledge the technical support provided by AASPI software from the University of Oklahoma and Petrel software from SLB.

REFERENCES

Ainsworth, R.B. and S. A. Pattison, 1994. Where have all the lowstands gone? Evidence for attached lowstand systems tracts in the Western Interior of North America: Geology, v. 22, no. 5, p. 415–418.

Allen, G.P., and H. W. Posamentier, 1993, Sequence stratigraphy and facies model of an incised valley fill; the Gironde Estuary, France: Journal of Sedimentary Research, v. 63, no. 3, p. 378–391.

Alqahtani, F.A., C. A. L. Jackson, H. D. Johnson, and M. R. B. Som, 2017, Controls on the geometry and evolution of humid–tropical fluvial systems–Insights from 3D seismic geomorphological analysis of the Malay Basin, Sunda Shelf, Southeast Asia: Journal of Sedimentary Research, v. 87, no. 1, p. 17–40.

Alqahtani, F.A., H. D. Johnson, C. A. L. Jackson, and M. R. B. Som, 2015, Nature, origin and evolution of a Late Pleistocene incised valley–fill, Sunda Shelf, Southeast Asia: Sedimentology, v. 62, no. 4, p. 1198–1232.

Anderson, J. B., A. Rodriguez, K. C. Abdulah, R. H. Fillon, L. A. Banfield, H. A. McKeown, and J. S. Wellner, 2004, Late Quaternary stratigraphic evolution of the northern Gulf of Mexico margin–a synthesis, in J. B. Anderson, and R. H. Fillon eds., Late Quaternary Stratigraphic Evolution of the Northern Gulf of Mexico Margin: Society of Economic Paleontologists and Mineralogists, Special Publication, v.79, p. 1–23.

Ardies, G. W., R. W. Dalrymple, and B. A. Zaitlin, 2002, Controls on the geometry of incised valleys in the Basal Quartz unit (Lower Cretaceous), Western Canada Sedimentary Basin: Journal of Sedimentary Research, v. 72, no. 5, p. 602–618.

Bhattacharya, J. P., and B. J. Willis, 2001, Lowstand deltas in the Frontier Formation, Powder River Basin, Wyoming: implications for sequence stratigraphic models. AAPG Bulletin, v. 85, no. 2, p. 261–294.

Blum, M. D., and T. E. Törnqvist, 2000, Fluvial responses to climate and sea-level change: a review and look forward: Sedimentology, v. 47, p. 2–48.

Blum, M., J. Martin, K. Milliken, and M. Garvin, 2013, Paleovalley systems: insights from Quaternary analogs and experiments: Earth–Science Reviews, v.116, p. 128–169.

Bowen, D. W., and P. Weimer, 2003, Regional sequence stratigraphic setting and reservoir geology of Morrow incised–valley sandstones (lower Pennsylvanian), eastern Colorado and western Kansas: AAPG bulletin, v. 87, no. 5, p.781–815.

Boyd, R., R. W. Dalrymple, and B. A. Zaitlin, 2006, Estuarine and Incised–Valley Facies Models, in H. W. Posamentier, and R. G. Walker, eds., Facies Models Revisited: Society of Economic Paleontologists and Mineralogists, Special Publication, no. 84, p. 171–235.

Cartwright, J. and M. Huuse, 2005, 3D seismic technology: the geological 'Hubble': Basin Research, v. 17, no. 1, p. 1–20.

Castelltort, S., and J. Van Den Driessche, 2003, How plausible are high–frequency sediment supply–driven cycles in the stratigraphic record?: Sedimentary geology, v. 157, no.1–2, p. 3–13.

Catuneanu, O., 2006, Principles of Sequence Stratigraphy, Elservier.

Catuneanu, O., V. Abreu, J. P. Bhattacharya, M.D. Blum, R.W. Dalrymple, P.G. Eriksson, C. R. Fielding, W. L. Fisher, W. E. Galloway, M. R. Gibling and K. A. Giles, 2009, Towards the standardization of sequence stratigraphy: Earth–Science Reviews, v. 9, no.1–2, p. 1–33.

Chopra, S., and K. J. Marfurt, 2007, Seismic attributes for prospect identification and reservoir characterization, Chapter 3. Coherence, Society of Exploration Geophysicists, Geophysical Developments, no. 11, p. 45–72.

Chopra, S., and K. J. Marfurt, 2007. Volumetric curvature attributes add value to 3D seismic data interpretation: The Leading Edge, v. 26, no. 7, p. 856–867.

Chopra, S., and K. J. Marfurt, 2008, Emerging and future trends in seismic attributes: The Leading Edge, v. 27, no. 3, p. 298–318.

Clift, P. D., 2006, Controls on the erosion of Cenozoic Asia and the flux of clastic sediment to the ocean: Earth and Planetary Science Letters, v. 241, no. 3–4, p. 571–580.

Dalrymple, R. W., D. A. Mackay, A. A. Ichaso, and K. S. Choi, 2012, Processes, morphodynamics, and facies of tide–dominated estuaries, in R. Davis Jr, and R. Dalrymple, eds., Principles of Tidal Sedimentology. Springer, p. 79–107.

Dalrymple, R.W., 2006. Incised valleys in time and space–An introduction to the volume and an examination of the controls on valley formation and filling, in R. W. Dalrymple, D. A. Leckie, and R. W. Tillman, eds., Incised Valleys in Time and Space: Society of Economic Paleontologists and Mineralogists, Special Publication v.85, p. 5–10.

Darmadi, Y., B. J. Willis, and S. L. Dorobek, 2007, Three–dimensional seismic architecture of fluvial sequences on the low–gradient Sunda Shelf, offshore Indonesia: Journal of Sedimentary Research, v. 77, no. 3, p. 225–238.

De Santis, V., and M. Caldara, 2016, Evolution of an incised valley system in the southern Adriatic Sea (Apulian margin): an onshore–offshore correlation: Geological Journal, v. 51, no. 2, p. 263–284.

Fitzsimmons, R., and S. Johnson, 2000, Forced regressions: recognition, architecture and genesis in the Campanian of the Bighorn Basin, Wyoming, in D. Hunt and R. L. Gawthorpe eds., Sedimentary Response to Forced Regressions: Geological Society of London, Special Publication, no. 172, p. 113–139.

Gibling, M.R., 2006, Width and thickness of fluvial channel bodies and valley fills in the geological record: a literature compilation and classification: Journal of sedimentary Research, v. 76, no. 5, p. 731–770.

Gugliotta, M., and Y. Saito, 2019, Matching trends in channel width, sinuosity, and depth along the fluvial to marine transition zone of tide–dominated river deltas–the need for a revision of depositional and hydraulic models: Earth–Science Reviews, v. 191, p. 93–113.

Hanebuth, T. J., and K. Stattegger, 2003, The stratigraphic evolution of the Sunda Shelf during the past fifty thousand years: Society of Economic Paleontologists and Mineralogists, Special Publication v.76, p. 189–200.

Hanebuth, T. J., and K. Stattegger, 2004, Depositional sequences on a late Pleistocene–Holocene tropical siliciclastic shelf (Sunda Shelf, southeast Asia): Journal of Asian Earth Sciences, v. 23, no. 1, p. 113–126.

Hanebuth, T.J., K. Stattegger, A. Schimanski, T. Lüdmann, and H. K. Wong, 2003, Late Pleistocene forced–regressive deposits on the Sunda Shelf (Southeast Asia): Marine Geology, v. 199, no.1–2, p.139–157.

Holbrook, J.M., and J. P. Bhattacharya, 2012, Reappraisal of the sequence boundary in time and space: case and considerations for an SU (subaerial unconformity) that is not a sediment bypass surface, a time barrier, or an unconformity: Earth–Science Reviews, v.113 no. 3, p. 271–302.

Hunt, D., and Tucker, M.E., 1992. Stranded parasequences and the forced regressive wedge systems tract: deposition during base–level fall. Sedimentary Geology, v. 81 no. 1, p. 1–9.

Kolla, V., H. W. Posamentier, and L. J. Wood, 2007, Deep–water and fluvial sinuous channels – Characteristics, similarities and dissimilarities, and modes of formation: Marine and Petroleum Geology, v. 24 no. 6–9, p. 388–405.

Labaune, C., G. Jouet, S. Berné, B. Gensous, M. Tesson, and A. Delpeint, 2005, Seismic stratigraphy of the Deglacial deposits of the Rhone prodelta and of the adjacent shelf: Marine Geology, v. 222, p.299–311.

Labaune, C., M. Tesson, B. Gensous, O. Parize, P. Imbert, and V. Delhaye–Prat, 2010, Detailed architecture of a compound incised valley system and correlation with forced regressive wedges: Example of Late Quaternary Têt and Agly rivers, western Gulf of Lions, Mediterranean Sea, France: Sedimentary Geology, v. 223, no. 3, p. 360–379.

Madon, M., C. L. Kim, and R. Wong, 2013, The structure and stratigraphy of deepwater Sarawak, Malaysia: Implications for tectonic evolution: Journal of Asian Earth Sciences, v.76, p. 312–333.

Manshor, N. A., M. H. A. Hassan, and M. Madon, 2022, Tidally–influenced fluvial channel systems from the Miocene Malay Basin, Malaysia: Evidence from core facies and seismic geomorphological analyses: Marine and Petroleum Geology, v.135, p. 105384.

Mansor, M.Y., A. H. A. Rahman, D. Menier, and M. Pubellier, 2014, Structural evolution of Malay Basin, its link to Sunda Block tectonics: Marine and Petroleum Geology, v. 58, p. 736–748.

Marfurt, K. J., 2006, Robust estimates of 3D reflector dip and azimuth: Geophysics, v. 71, no. 4, p. 29–P40.

Marfurt, K. J., R. L. Kirlin, S. L. Farme, and M. S. Bahorich, 1998, 3-D seismic attributes using a semblance–based coherency algorithm: Geophysics, v. 63, no. 4, p. 1150–1165.

Mattheus, C.R., and A. B. Rodriguez, 2011, Controls on late Quaternary incised-valley dimension along passive margins evaluated using empirical data. Sedimentology, v. 58, no. 5, p. 1113–1137.

Mellere, D., and R. Steel, 1995, Variability of lowstand wedges and their distinction from forced–regressive wedges in the Mesaverde Group, southeast Wyoming: Geology, v. 23, no. 9, p. 803–806.

Morley, C. K, and A. Racey, 2011, Tertiary stratigraphy, in M. F. Ridd, A. J. Barber, and M. J. Crow, eds., The Geology of Thailand: Geological Society, London, p. 223–271.

Morley, C. K., 2002, A tectonic model for the Tertiary evolution of strike–slip faults and rift basins in SE Asia: Tectonophysics, v. 347, no. 4, p. 189–215.

Muto, T., and R. J. Steel, 2001, Autostepping during the transgressive growth of deltas: results from flume experiments: Geology, v. 29, no. 9, p. 771–774.

Muto, T., and R. J. Steel, 2004, Autogenic response of fluvial deltas to steady sea–level fall: Implications from flume–tank experiments: Geology, v. 32, no. 5, p. 401–404.

Nummedal, D., G. W. Riley, and P. L. Templet, 1993, High–resolution sequence architecture: a chronostratigraphic model based on equilibrium profile studies, in H. W. Posamentier, C. P. Summerhayes, B. U. Haq and G. P. Allen, eds., Sequence Stratigraphy and Facies Associations, International Association of Sedimentologists Special Publication 18, p. 55–68.

Plint, A. G., and D. Nummedal, 2000, The falling stage systems tract: recognition and importance in sequence stratigraphic analysis, Geological Society, London, Special Publications, v.172, p. 1–17.

Plint, A. G., P. J. McCarthy, and U. F. Faccini, 2001, Nonmarine sequence stratigraphy: updip expression of sequence boundaries and systems tracts in a high–resolution framework, Cenomanian Dunvegan Formation, Alberta foreland basin, Canada. AAPG Bulletin, v. 85, no. 11, p. 1967–2001.

Plint, A.G., 1996. Marine and nonmarine systems tracts in fourth-order sequences in the Early–Middle Cenomanian, Dunvegan Alloformation, northeastern British Columbia, Canada: Geological Society, London, Special Publications, v. 104, p.159–191.

Plint, A.G., and B. Norris, 1991. Anatomy of a ramp margin sequence: facies successions, paleogeography, and sediment dispersal patterns in the Muskiki and Marshybank formations, Alberta Foreland Basin: Bulletin of Canadian Petroleum Geology, v. 39, no. 1, p. 18–42.

Plint, A.G., C. K. Wilgus, B. S. Hastings, H.W. Posamentier, C. A. Ross, and J. C. Van Wagoner, 1988, Sharp–based shoreface sequences and "offshore bars" in the Cardium Formation of Alberta: their relationship to relative changes in sea level, in C. K., Wilgus, B. S. Hasting, C. G. St. C. Kendall, H. W. Posamentier, C. A. Ross, and J. C. Van Wagoner, eds., Sea-level changes: An Integrated Approach, Society of Economic Paleontologists and Mineralogists, Special Publication, no. 42, p. 357–370.

Posamentier, H. W., 2001, Lowstand alluvial bypass systems: incised vs. unincised: AAPG Bulletin, v. 85, no. 10, p. 1771–1793.

Posamentier, H. W., 2002, Ancient shelf ridges—a potentially significant component of the transgressive systems tract: case study from offshore northwest Java: AAPG Bulletin, v. 86, no. 1, p. 75–106.

Posamentier, H. W., 2004, Seismic geomorphology: imaging elements of depositional systems from shelf to deep basin using 3D seismic data: implications for exploration and development, in R. J. Davies, J. A. Cartwright, S. A. Stewart, M. Lappin and J. R. Underhill, eds., 3D Seismic Technology: Geological Society, London, Memoirs, v. 29, p, 11–24

Posamentier, H. W., and Morris, W. R., 2000, Aspects of the stratal architecture of forced regressive deposits, in D. Hunt, and R. L. Gawthorpe eds., Sedimentary Responses to Forced Regressions, Geological Society, London, Special Publications, v.172, p. 19–46.

Posamentier, H. W., and V. Kolla, 2003, Seismic geomorphology and stratigraphy of depositional elements in deep–water settings: Journal of sedimentary research, v. 73, no. 3, p. 367–388.

Posamentier, H. W., and Vail, P. R., 1988, Eustatic controls on clastic deposition II—sequence and systems tract models, in C. K., Wilgus, B. S. Hasting, C. G. St. C. Kendall, H. W. Posamentier, C. A. Ross, and J. C. Van Wagoner, eds., Sea–level changes–An Integrated Approach: Society of Economic Paleontologists and Mineralogists, Special Publication, no. 42, p. 125–154.

Posamentier, H. W., R. D. Erskine, and R. M. Mitchum Jr, 1991, Models for submarine–fan deposition within a sequence–stratigraphic framework, in P. Weimer, and M. H. Link, eds., Seismic facies and sedimentary processes of submarine fans and turbidite systems, Springer, New York, p. 127–136.

Posamentier, H. W., V. Paumard, and S. C. Lang, 2022, Principles of seismic stratigraphy and seismic geomorphology I: Extracting geologic insights from seismic data: Earth–Science Reviews, v. 228, p.103963(1–57).

Pubellier, M., and C. K. Morley, 2014, The basins of Sundaland (SE Asia): Evolution and boundary conditions: Marine and Petroleum Geology, v. 58, p. 555–578.

Reijenstein, H. M., H. W. Posamentier, and J. P. Bhattacharya, 2011, Seismic geomorphology and high–resolution seismic stratigraphy of inner–shelf fluvial, estuarine, deltaic, and marine sequences, Gulf of Thailand: AAPG Bulletin, v. 95, no.11, p. 1959–1990.

Schumm, S.A., 1981, Evolution and response of the fluvial system, sedimentologic implications, in F. G. Ethridge, and R. M. Flores, eds., Recent and Ancient Nonmarine Depositional Environments: Models for Exploration: Society of Economic Paleontologists and Mineralogists, Special Publication, v. 31, p. 19–29.

Shanley, K.W., and P. J. McCabe, 1994, Perspectives on the sequence stratigraphy of continental strata, AAPG bulletin, v. 78, no. 4, p. 544–568.

Simms, A. R., J. B. Anderson, Z. P. Taha, and A. B. Rodriguez, 2006, Overfilled versus underfilled incised valleys: examples from the Quaternary Gulf of Mexico: Society of Economic Paleontologists and Mineralogists, Special Publication, v. 85, p. 117–139.

Snedden, J.W., and D. Nummedal, 1992, Origin and geometry of storm-deposited sand beds in modern sediments of the Texas continental shelf, in D. J. P. Swift, G. F. Oertel, R. W. Tillman, and J. A. Thorne, eds., Shelf sand and sandstone bodies: Geometry, facies and sequence stratigraphy, International Association of Sedimentologists Special Publication, no. 14, p. 283–308.

Strong, N., and C. Paola, 2008. Valleys that never were–time surfaces versus stratigraphic surfaces: Journal of Sedimentary Research, v. 78, no. 8, p. 579–593.

Suter, J. R., 2006, Facies models revisited–clastic shelves, in H. W. Posamentier, and R. G., Walker, eds., Facies models revisited: Society of Economic Paleontologists and Mineralogists, Special Publication, no. 84, p.339–397.

Twarog, M. R., S. J. Culver, D.J. Mallinson, E. Leorri, B. Donovan, E. I. Harrison, H. Hindes, D. Reed, E. Horsman, N. A. M. Shazili, and P. R. Parham, 2021, Depositional environments and sequence stratigraphy of post–last glacial maximum incised valley–fill, Malay Basin, northern Sunda Shelf: Marine Geology, v. 436, p. 106457.

Vail, P. R., 1987, Seismic stratigraphy interpretation using sequence stratigraphy: Part 1: Seismic stratigraphy interpretation procedure, in A. W. Bally, eds., Atlas of Seismic Stratigraphy: AAPG Studies in Geology, no. 27, p. 1–10.

Van Wagoner, J. C., H. W., Posamentier, R. M. Mitchum. Jr., P. R. Vail, J. F. Sarg, T. S., Loutit, and J. Hardenbol, 1988, An overview of sequence stratigraphy and key definitions. In C. K. Wilgus, B. S. Hastings, C. G. St. C. Kendall, H. W. Posamentier, C. A. Ross and J. C. Van Wagoner, eds., Sea Level Changes–An Integrated Approach, Society of Economic Paleontologists and Mineralogists, Special Publication, no. 42, p. 39–45.

Van Wagoner, J. C., R. M. Mitchum Jr, H. W. Posamentier, and P. R. Vail, 1987, Seismic stratigraphy interpretation using sequence stratigraphy: Part 2: Key definitions of sequence stratigraphy, in A. W. Bally eds., Atlas of Seismic Stratigraphy: American Association of Petroleum Geologists, Studies in Geology, no. 27, v. 1, p. 11–14.

Van Wagoner, J.C., R. M. Mitchum, K. M. Campion, and V. D. Rahmanian, 1990, Siliciclastic sequence stratigraphy in well logs, cores, and outcrops: concepts for high–resolution correlation of time and facies: American Association of Petroleum Geologists, Methods in Exploration, no. 7, p.1–55.

Waelbroeck, C., L. Labeyrie, E. Michel, J. C. Duplessy, J. F. Mcmanus, K. Lambeck, E. Balbon, and M. Labracherie, 2002, Sea–level and deep water temperature changes derived from benthic foraminifera isotopic records: Quaternary science reviews, v. 21 no. 1, p. 295–305.

Wellner, R. W., and L. R. Bartek, 2003, The effect of sea level, climate, and shelf physiography on the development of incised–valley complexes: a modern example from the East China Sea: Journal of sedimentary research, v. 73, no. 6, p. 926–940.

Wellner, R.W., B. L. Varban, X. Roca, J. A. Flaum, E. K. Stewart, and M. D. Blum, 2018, Simple is better when it comes to sequence stratigraphy–The Clearwater Formation of the Mannville Group reinterpreted using a genetic body approach: AAPG Bulletin, v. 102, no. 3, p. 447–482.

Wetzel, A., A. Feldens, D. Unverricht, K. Stattegger, and R. Tjallingii, 2021, Late Pleistocene sea–level changes and the formation and fill of bent valleys incised into the shelf of the western South China Sea: Journal of Asian Earth Sciences, v. 206, p. 104626.

Yakzan, A. M., A. Harun, B. M. Nasib, and R. J. Morley, 1996, Integrated biostratigraphic zonation for the Malay Basin: Bulletin of the Geological Society of Malaysia, v. 39, p. 157–184.

Zaitlin, B. A., R.W. Dalrymple, and R. O. N. Boyd, 1994. The stratigraphic organization of incised–valley systems associated with relative sea–level change: Society of Economic Paleontologists and Mineralogists, Special Publication, no. 51, p. 45–61.

APPENDIX

The eigenstructure ratio coherence is based on the eigenvectors and eigenvalues of the covariance matrix of a local windowed segment of multichannel data. The main idea is to compare the dominant eigenvalue to the sum of all eigenvalues, as a measure of similarities and dissimilarities among the seismic wavelets. An M-trace seismic amplitude volume, the covariance matrix, C, is constructed by comparing each sample vector to itself and all of its neighbors.

$$C_{mn} = \frac{1}{K}\sum_{k=1}^{K}[d(t_k, x_m, y_m)d(t_k, x_n, y_n) + d^H(t_k, x_m, y_m)d(t_k, x_n, y_n)] \quad \text{(A-1)}$$

Where, C_{mn} is element of the spatial covariance matrix between traces m and n. K is number of samples in the analysis window. $d(t_k, x_m, y_m)$ is complex data value at time t_k and spatial location (x_m, y_m). d^H is Hilbert transform of d.

The principal component structure-oriented filtering is first used to construct a covariance matrix from the 2K+1 sample vectors and then computes eigenvectors prior to cross correlating it with the target sample vector, filtered version of the data, d_{pc} and d_{pc}^H. The total energy attribute is simply the sum of the energy of the weighted analytic traces (with tapers, w_k and w_m) used to compute the covariance matrix:

$$E_{total} = \sum_{k=-K}^{+K} w_k^2 \sum_{m=1}^{+M} w_m^2 \{[d(t_k, x_m, y_m)]^2 + d^H(t_k, x_m, y_m)^2\} \quad \text{(A-2)}$$

The coherent energy attribute is the sum of the energy of the corresponding weighted filtered traces:

$$E_{coh} = \sum_{k=-K}^{+K} w_k^2 \sum_{m=1}^{+M} w_m^2 \{\left[d_{pc}(t_k, x_m, y_m)\right]^2 + d_{pc}^H(t_k, x_m, y_m)^2\} \quad \text{(A-3)}$$

Energy-ratio coherence is then defined as:

$$C_{ER} = \frac{E_{coh}}{E_{total}} \quad \text{(A-4)}$$

Chapter 2: 3-D Seismic Geomorphology of Abandoned Channels, North Malay Basin, Gulf of Thailand

*This chapter has been accepted for publication in the journal *Interpretation*

Zhai, R., 2025, 3-D seismic geomorphology of abandoned channels, North Malay Basin, Gulf of Thailand.

*This chapter was presented by invitation at the IMAGE 2020 Annual Convention and Exhibition.

Zhai, R., and J. D. Pigott, 2020, 3D seismic geomorphology of the abandoned channel for insight into a more complete fluvial reservoir characterization: IMAGE 2020 Annual Convention and Exhibition.

ABSTRACT

Abandoned channels are ubiquitous and important sedimentary units in fluvial sedimentary systems. Their fine-grained muddy matrix often forms a barrier to fluid flow in hydrocarbon reservoirs. However, these mud-filled abandoned channels are frequently ignored in seismic geomorphology interpretation, as attention focuses on sandstone-prone architectural elements rather than mudstone-rich deposits. To better characterize abandoned channels in the study area of the North Malay Basin, Gulf of Thailand, high-resolution 3-D seismic data are employed to image paleo geomorphologic features of the Pliocene to Pleistocene meandering river system over 600 km^2 (232 mi^2). The 3-D energy-ratio coherence and continuous wavelet transform data reveal various fluvial system patterns, including the incised channel belt, the single channel belt, and the compound channel belt, ranging from 480 m (1576 ft) to over 8 km (5 mi) wide. In contrast to sandstone-prone channel deposits, mudstone-prone abandoned channels result from channel degradation processes, encased in channel belt sandstone with widths ranging from 120 to 385 m (394 to 1263 ft). Four types of abandoned channels are identified: the low-sinuosity abandoned channel, the high-sinuosity single abandoned channel, the neck cutoff abandoned channel, and the bifurcation abandoned channel. These abandoned channels complicate lithological heterogeneity and reduce the connectivity of fluvial channel belt sandstones. This study outlines recognition criteria for abandoned channels and links their seismic and geomorphic expressions, promoting improved fluvial geomorphology interpretation and subsurface lithology distribution assessment.

2.1 INTRODUCTION

The study of abandoned channels within fluvial systems is becoming a critical focus in fluvial geomorphology, as these features record significant responses to fluvial style changes, variations in paleo-discharge, and the intensity of paleo-flooding driven by autogenic dynamics (Macklin and Lewin, 2003; Constantine et al., 2010; Erkens et al, 2011). Moreover, there has been increasing interest in identifying subsurface abandoned channels as fine-grained sedimentary architectural units that critically impact hydrocarbon reservoir heterogeneity (Ghinassi et al., 2016; Simon and Gibling, 2017; Cosma et al., 2019). Abandoned channels are topographic depressions representing the geomorphologic expression of channel migration and extinction processes on the floodplain (Allen, 1965; Lewis and Lewin, 1983; Shields and Abt, 1989). Hydrologically, the waterbodies within abandoned channels remain separate from active channel flows, appearing as former rivers, oxbows, swamps, billabongs, and bayous (Phillips, 2013; Rhoad, 2020). Studies have examined the mechanisms driving this transition from permanently flowing channels to abandoned channels, emphasizing factors such as diversion angle, flow separation zones, and bedload aggradation (Hooke, 2004; Constantine et al., 2008; Toonen et al., 2012). The loss of water flow and reduced flow energy allow the abandoned channel to be predominantly filled with fine-grained materials from the overbank flooding of the main channel (Walker and Cant, 1984; Miall, 1996). Depositional records in abandoned channels are referred to as mud plugs, preserve important information for reconstructing channel discharge and flood intensity (Gray et al., 2016; Dépret et al., 2017) and depositional environments (Kasse et al., 2005; Bos et al., 2008). The abandoned channel mud plugs act as a barrier to fluid flow, significantly impacting hydrocarbon accumulation and distribution in fluvial reservoirs (Lynds and Hajek, 2006; Snedden, 2013; Colombera et al., 2017). Although the importance of abandoned channels in determining the connectivity of fluvial depositional sandbodies is acknowledged, and some progress has been made in understanding their impacts on sediment transport and sedimentation patterns in modern rivers, research on the geomorphological variation of abandoned channels remains limited due to spatial data constraints.

Advances in geophysical imaging approaches have intensified research on 3-D seismic geomorphology of subsurface fluvial depositional systems (Kolla et al., 2007; Posamentier et al., 2007; Wood et al., 2009). Recent studies in fluvial seismic geomorphology provide a visualized understanding of geomorphological characteristics and architectural units through 3-D seismic-derived plan view images (Darmadi et al.,2007; Manshor et al., 2022). Some studies utilizing high-resolution seismic data have identified the presence of abandoned channels and noticed their considerable proportion in fluvial sedimentary records (Reijenstein et al.,2011; Speed et al., 2023). However, detailed investigations into their spatial distribution, geomorphological characteristics, and impact on channel fill connectivity remain underexplored.

This study aims to enhance understanding of geomorphological patterns and spatial distribution of abandoned channels by investigating the stratigraphic expression and geomorphological form of meandering channels within the Pliocene to Pleistocene stratigraphy in the North Malay Basin, Gulf of Thailand. The objectives of this study are to (1) quantitatively identify and interpret the characteristics of abandoned channels in fluvial sedimentary strata; (2) characterize abandoned channel geometry and its relationship to channel sandstone; and (3) evaluate their potential impact on channel sandstone connectivity. Analysis of the 3-D seismic geomorphology in the study area provides new insights into further deepening the understanding of the heterogeneity of fluvial reservoirs in similar settings.

2.2 TECTONIC AND STRATIGRAPHIC SETTING

The North Malay Basin is the northern part of the Grand Malay Basin, located in the center of the Gulf of Thailand (GoT) and east of the Malay Peninsula (Figure 2.1. A). This basin stretches approximately 300 km (186 mi) in length and 100 km (62 mi) in width, with a northwest-southeast tectonic orientation protruding northward into basement highs. The North Malay Basin is one of a series of Cenozoic intracratonic rift basins in the GoT (Morley et al., 2011; Mansor et al., 2014), known for its fluvial-dominated huge thick deposits with sedimentary succession reaching up to 12 km (7.5 mi) in the basin center (Madon et al., 2006).

The thick terrigenous fills in the North Malay basin directly relate to four tectonic deformation episodes: rifting, rapid subsidence, compressional inversion, and basin sag (Figure 2.1. C). During the Late Eocene to Late Oligocene rifting stage, the collision of the Indo-Australian Plate with the Eurasian Plate caused northwest-southeast left-lateral shearing across the north-central Sunda Block, forming the north-south trending North Malay Basin with extensive half-grabens. These fault-bounded half-grabens provided ample accommodation for the accumulation of terrigenous detrital deposits, reaching up to 4 km (2.5 mi) of syn-rift deposits in the basin center. After the cessation of extensional rifting, the basin rapidly subsided due to the hot lithosphere, and sediment loads drove lower crustal flow toward the highlands during the Early to Middle Miocene, creating more accommodation for terrigenous sediment fluxes. Basin inversion occurred during the Middle to Late Miocene, as the northward dive of the Indo-Australian Plate beneath the Sunda Block led to right-lateral shearing across the GoT. Transpression uplifted and tilted the North Malay Basin northwestward, forming a regional Mid-Miocene unconformity.

Transgressions from south to north diminished the terrigenous clastic supply to the south of the basin. In the final evolutionary stage, the basin subsided without significant tectonic disturbance throughout the Pliocene, forming a broad, shallow sag that was eventually submerged by transgression covering the entire GoT (Kornsawan and Morley, 2002; Searle and Morley, 2011; Pubellier and Morel, 2014).

The stratigraphy of the North Malay Basin is divided into five third-order sequences, Sequence I to Sequence V, from oldest to youngest, in response to the basin's tectonic evolution (Madon et al., 2006; Kessler et al., 2020). Another established stratigraphic subdivision scheme known as Groups utilizes alphabetical nomenclature from Group A to Group P (Figure 2.1. C). Sequence I consists of syn-rift and early post-rift strata deposited during the Late Eocene to Early Miocene. The syn-rift strata accumulated axial and transverse sediment influxes related to fault activity within the half-grabens, where lacustrine sediments interbedded with alluvial fan and fluvial-deltaic sandstone overlying the basement, capped by early post-rift lacustrine shale at the top. Sequence II was deposited in the rapid subsidence post-rift stage in the Early Miocene. The former lake formed extensive wetlands, and fluvial systems carried large amounts of sediments from the northern margin flow into the basin, resulting in thick successions of fluvial sandstone and floodplain shale. Sequence III was deposited during the Middle Miocene, characterized by slow basin subsidence and rapid transgression. This sequence is dominated by fluvial sandstone, siltstone with thick lacustrine shale, and occasional marginal marine deposits associated with significant transgressive events. Sequence IV was formed during the regression stage resulting from basin inversion from the late Middle to Late Miocene, featuring a regional unconformity at the top. The strata comprised interbedded sandstone, siltstone, and shale with coals primarily deposited in coastal plain and floodplain environments. Sequence V corresponds to the late thermal subsidence stage of the basin from the Late Miocene to Pliocene, with episodic marine transgressions. The increasing marine influence developed a succession of interbedded sandstones, siltstones, and shales (Yakzan et al., 1996; Morley and Westaway, 2006; Morley and Racey, 2011).

This study focuses on the fluvial succession of Sequence V (Groups A and B) along the northwestern flank of the North Malay Basin (Figure 2.1. C). Source tracing across the Sunda shelf reveals that the GoT transitioned into a tropical climate, leading to increased erosion of the basin surroundings since the early Miocene and the continuous influx of abundant terrigenous sediments from the north through fluvial systems into the North Malay Basin (Chaiwongsaen et al., 2019; Bidorn et al., 2021).

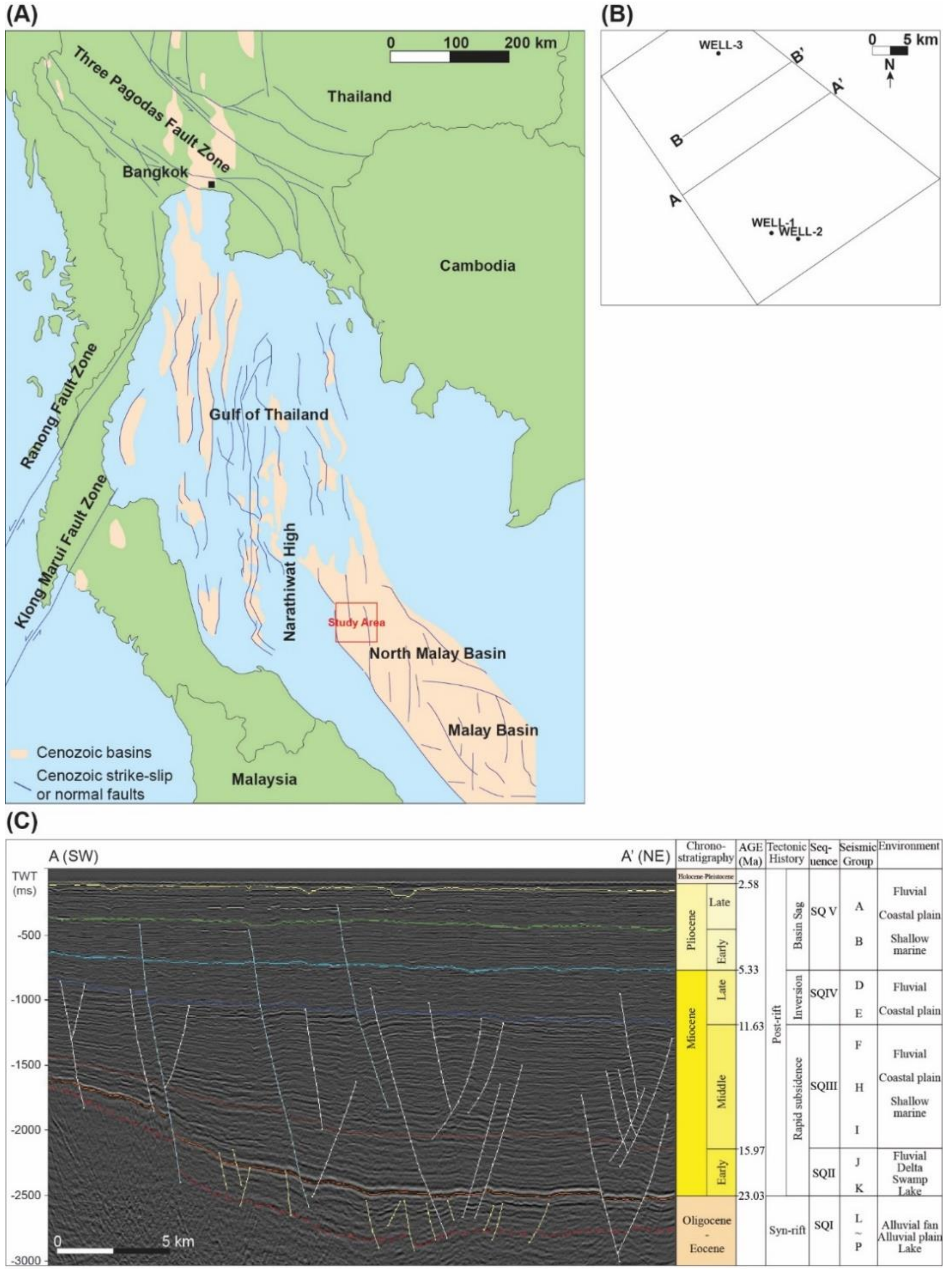

Figure 2.1: Overview of the study area and regional geological framework. (A) Cenozoic rift basins in the Gulf of Thailand (GoT) and the location of the study area (modified from Morley et al., 2011). The GoT is part of the Sunda Shelf; the Cenozoic rift basins in the GoT form an N-S striking zone. The Eocene-Oligocene NW-SE trending rifts formed the North Malay Basin in the central GoT. (B) The study area is located on the northwest flank of the North Malay basin, with the 3-D Seismic data surveys covering approximately 600 km^2 (232 mi^2). (C) Seismic cross section and chronostratigraphy of the North Malay Basin. Following tectonic inversion during the Late Miocene, regional subsidence and transgressions form the thick alternating strata of fluvial and shallow marine deposits since the Pliocene. This study focuses on an interval with increased fluvial depositional systems in the uppermost 500 ms of seismic data.

2.3 METHODS AND DATASET

3-D seismic geomorphology methods (Posamentier et al., 2007; Wood and Mize-Spansky, 2009) are used to identify and interpret seismic reflection characteristics in fluvial sedimentary strata within the Late Miocene to Pleistocene study interval. This method emphasizes the analysis of landforms extracted from various 3-D seismic data and the integration with seismic stratigraphy to derive comprehensive stratigraphic insights (Posamentier et al., 2022). Following this fundamental principle, this study focuses on those workflows and seismic attributes that yield the most valuable results for identifying and interpreting fluvial architectural elements; several key steps in the seismic geomorphological interpretation process involve: (1) interpreting critical stratigraphic surfaces. This step entails identifying key stratigraphic surfaces, such as sequence boundaries and maximum flooding surfaces, by analyzing reflection terminations in 3-D seismic data. Seismic unconformities are recognized to delineate sequence boundaries, enabling the construction of successive seismic units (SUs), where each SU represents the highest-order seismic sequence stratigraphic unit (Posamentier et al., 1988). (2) Identifying seismic facies. Within each SU, groups of reflections characterized by amplitude intensity, continuity, and geometric configurations are used to define distinct seismic facies (SF) (Mitchum et al., 1977; Vail, 1987). (3) Calculating 3-D seismic attributes. 3-D seismic coherence and spectral decomposition are employed to visualize seismic reflection anomalies. (4) Constructing seismic stratal slices through 3-D seismic attributes to identify and interpret fluvial depositional units in plan view (Zeng et al., 1998, 2007). The relatively flat seafloor reflection and two maximum-flooding surfaces serve as reference surfaces for generating seismic stratal slices. (5) Identifying and interpreting geometry, dimensions, and stratigraphic variability of abandoned channels.

Precise seismic geomorphological interpretations of seismic data require that seismic attributes reflect patterns related to depositional features. Two primary 3-D seismic attributes, energy-ratio coherence and continuous wavelet transform spectral decomposition, are utilized to visualize lateral variations in seismic waveforms and amplitudes. Various coherence algorithms provide reliable methods for measuring seismic character variation and play a significant role in delineating faults (Marfurt et al., 1998; Gersztenkorn and Marfurt, 1999; Kington, 2015; Wu, 2017; Chopra and Marfurt, 2018; Wu and Guo,2018). This study employs the energy-ratio coherence method to highlight the waveform differences produced by lateral variations in lithology within fluvial sedimentary strata. This method calculates the ratio between coherent energy and the total energy of seismic traces within the analysis window. Marfurt (2006) provides details on constructing a covariance matrix to calculate coherent energy from principal-component filtered seismic traces and their Hilbert transform, and total energy from original seismic traces and their Hilbert transform. We take several key steps to ensure the quality of results, including (1) calculating the volumetric dip, the coherence is performed based on accurate estimates of the structural dip; (2) constructing the covariance matrix, a 3-trace by 3-trace covariance matrix is assigned for filtered seismic data calculations; and (3) defining the analysis window size, set to 20 ms based on the waveform structure and its variation range to encompass the complete wavelet envelope and minimize stratigraphic mixing. Finally, channel geometry and edge are identified using the co-rendered display of energy-ratio coherence and amplitude on seismic slices.

To further validate the reliability of the observed seismic patterns, the continuous wavelet transform (CWT) in spectral decomposition is applied to improve the visualization of channels and their internal architectural units. The CWT derives the seismic spectrum by convolving seismic traces with the complex conjugate of scaled wavelets at each time location, decomposing the non-stationary seismic signals into spectral magnitude and spectral phase components (Goupillaud et al., 1984; Castagna and Sun, 2006; Mallat, 2009; Chopra and Marfurt, 2016; Russell and Han, 2016). The spectral magnitude at each frequency reflects the energy distribution of seismic signals, correlates with bed thickness, and has been widely used to delineate geological features below seismic resolution (Partyka et al., 1999; Sinha et al., 2005; Kazemeini et al., 2009; Lapins et al., 2020). In this study, we use the Morlet wavelet as the mother wavelet to perform CWT, applying a 5 Hz spectral sampling interval within the effective bandwidth of seismic data (10–80 Hz) to capture detailed frequency variations. Low-frequency components (20-35 Hz) are used to reveal thicker, continuous channel belts, mid-frequency components (40-55 Hz) are applied to delineate internal architectural units by balancing the imaging continuity and seismic resolution, and high-frequency components (60-80 Hz) are selected to highlight the fine details of depositional features. Then, these three frequency components are combined using RGB blending to generate composite images that visually accentuate geological features on seismic slices. The selection of frequency components is an iterative process of inspecting how different architectural units appear at various frequencies in RGB blending images to determine the optimal combination.

This study utilizes nearly 600 km^2 (232 mi^2) of 3-D seismic data to observe and interpret seismic geomorphology. The dataset comprises multiple offshore 3-D seismic surveys with a bin size of 25 m × 25 m (82 ft × 82 ft) and a sample rate of 2 ms. The dominant frequency of seismic data is 70 Hz, with an effective bandwidth of 8 to 80 Hz. The target formation has an average interval velocity of 1,700 m/s (5,577 ft/s), derived from sonic log data after well-seismic calibration. This velocity is used to estimate the depth of geological features in the study interval. As a result, this seismic data can resolve strata approximately 6.1 m (20 ft) thick, with a horizontal resolution of 25 m (82 ft) determined by the bin size. Using this high-resolution seismic dataset, we identified the smallest identifiable seismic stratigraphic units within the uppermost 500 ms.

2.4 RESULTS

2.4.1 Seismic Units

Five regional seismic discontinuities are identified based on reflection terminations, characterized by strong fluctuating reflections that downcut and truncate underlying parallel moderate to weak reflections. From the seafloor reflection at 100 ms down to 500 ms, the shallow stratigraphic records are divided into five seismic stratigraphic units labeled SU-1 to SU-5 from the deepest to the seafloor (Figure 2.2). Seven seismic facies are identified within these seismic stratigraphic units based on variations of external configuration and internal reflection continuity and intensity on seismic sections (Figure 2.3). These seismic facies include SF-1: high-amplitude, undulating or discontinuous reflections; SF-2: low to moderate amplitude, parallel continuous reflections; SF-3: U-shaped high-amplitude configuration; SF-4: high-amplitude, shingled parallel reflections; SF-5: high amplitude, hummocky to chaotic reflections; SF-6: high-amplitude, undulating, or discontinuous reflections; and SF-7: low amplitude, concave-down reflections. These seismic facies describe the seismic stratigraphy and geomorphic characteristics of depositional units within a seismic stratigraphic framework.

The study succession shows a vertical stacking pattern of stratigraphic units with similar reflection characteristics. A key characteristic is that the lower parts of each seismic stratigraphic unit are primarily composed of high amplitude discontinuous reflections (SF-1) that contain various configurations: fluctuant to concave up stratified (SF-3), U-shaped (SF-4), sigmoidal dipping (SF-5), and hummocky to chaotic reflections (SF-6). These reflections appear as independent U-shaped forms or combinations restricted in depressions above sequence boundaries. A strong continuous reflection typically drapes these depressions, indicating the transition to the overlying lateral continuous reflections, defined as maximum flooding surfaces (MFS). Extending from the MFS upward to the next sequence boundary, the middle to upper interval of each seismic stratigraphic unit consists mainly of moderate amplitude, subparallel to parallel, stratified seismic reflections (SF-5), occasionally interspersed with smaller internal channel forms (SF-1). Another key feature of the seismic stratigraphic unit is the recognizable separation of the upper and lower strata, with the upper parallel strata being considerably thicker than the lower channel-form assemblages.

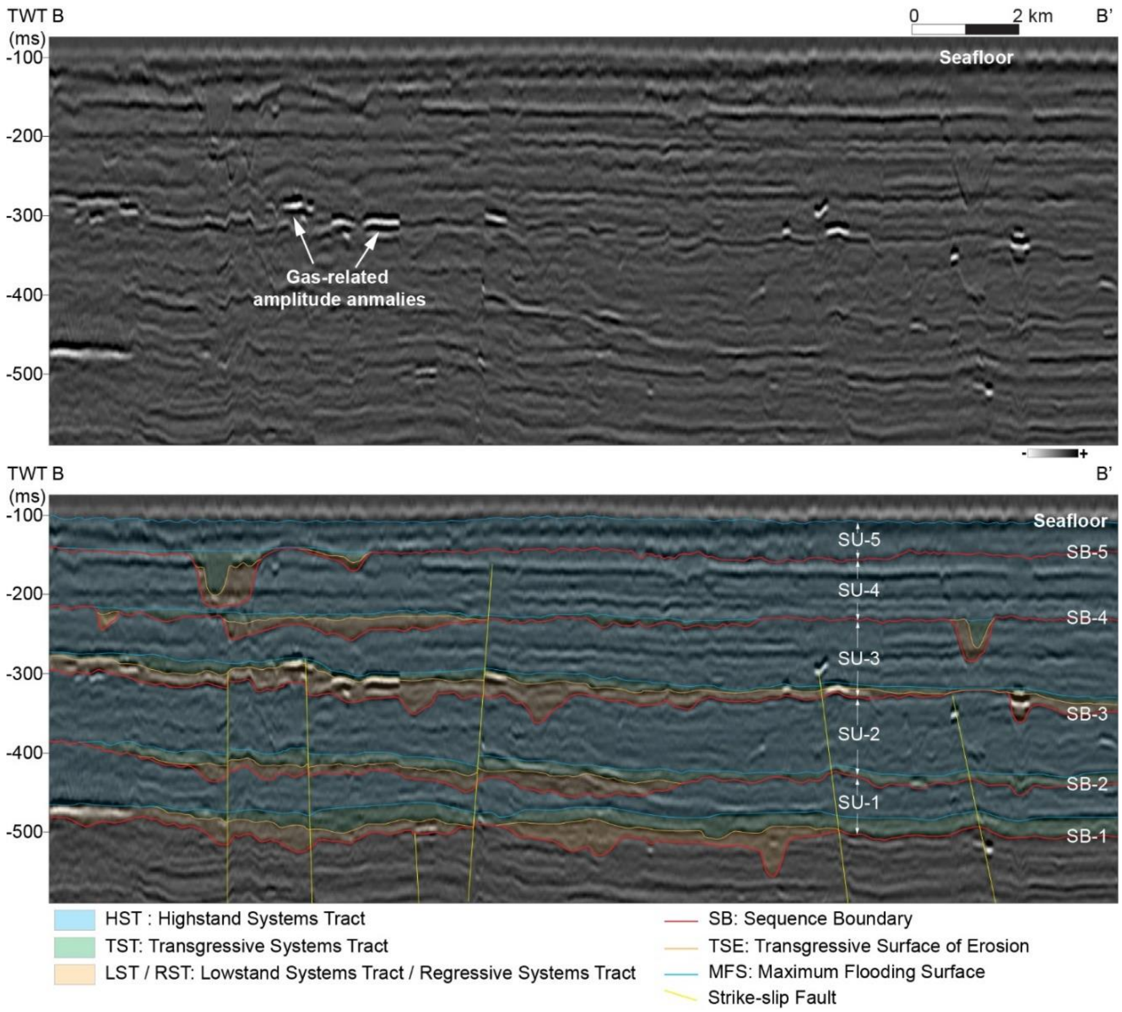

Figure 2.2: (A) Uninterpreted and (B) interpreted seismic cross-section of the uppermost 500 ms (two-way time) seismic data reveal five regional seismic discontinuities (SB-1 to SB-5). These discontinuities and the top seafloor reflection define five seismic stratigraphic units (SU-1 to SU-5). The location of this section is shown in Figure 2.1(B).

Seismic Facies		Reflection Characteristics
SF-1	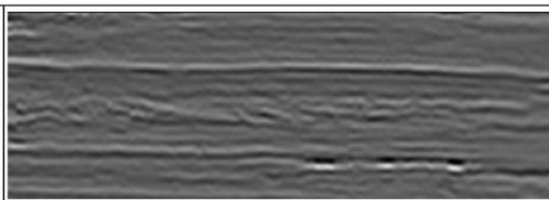	High-amplitude, undulating or discontinuous reflections sandwiched between parallel reflections
SF-2	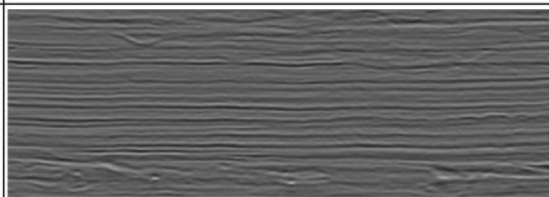	Low to moderate amplitude, parallel or subparallel continuous reflections
SF-3	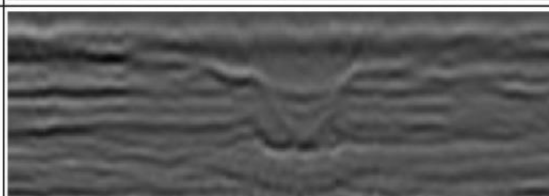	U-shaped high-amplitude configuration, truncates the underlying parallel reflections
SF-4	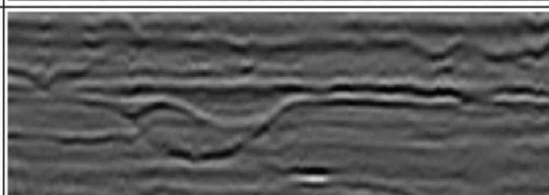	High-amplitude, continuous fluctuant base reflection, and concave-down, low-amplitude top reflection
SF-5	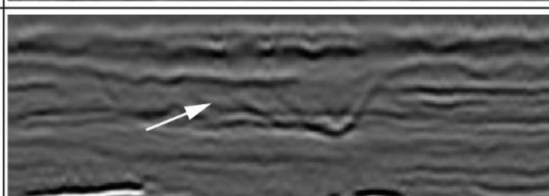	High-amplitude, shingled or oblique parallel reflections, downdip to the high-amplitude reflections
SF-6	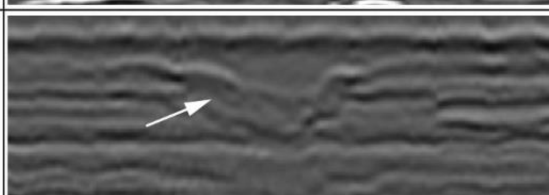	High amplitude, hummocky to chaotic reflections in low-amplitude context
SF-7	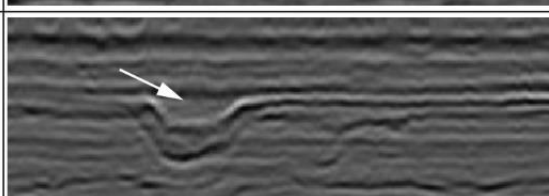	Small-scale, low amplitude, concave-down uniform reflections

Figure 2.3: Seven typical seismic facies are identified within the study interval based on seismic reflection patterns differentiated by reflection geometric configuration, continuity, and intensity. SF-1 and SF-2 represent the seismic reflection patterns of successions; SF-3, SF-4, SF-5, SF-6, and SF-7 depict the reflection patterns within SF-1 and SF-2.

2.4.2 Seismic Geomorphology

Successive stratal slices extracted from seismic stratigraphic units exhibit different varied fluvial geomorphic features. Five representative seismic stratal slices containing abundant seismic facies are selected to illustrate distinct seismic geomorphic features in different vertical positions of seismic stratigraphic units. The slices through the lower parts of seismic stratigraphic units primarily reveal dense channel development above the sequence boundary, exhibiting broad, interwoven channel belts. Figure 2.4 displays a north-south cluster of channels closely aligned with the base of SU-1. For the most part, only a pattern of crossing channel fragments is observed, with few features identifiable as complete channel forms. These entangled channel forms result from superimposed channel belts in closely spaced vertical intervals concentrated above the seismic stratigraphic boundaries. Consequently, geomorphic features of asynchronous channel fragments coexist within the same seismic slice. The intertwining and nesting of channels and variations in width and sinuosity make it challenging to trace individual channel boundaries, leaving only broad, complex channel belts visible. Figure 2.5 shows a slice extracted at the lower parts of SU-3, where a broad meander belt consisting of multiple channels emerges above the sequence boundaries, delineating another typical pattern of channel assemblage. A series of highly sinuous channels are observed to amalgamate into a broader compound belt on this slice. On the northeast corner of the slice, one well-preserved, highly sinuous channel is observed on the western flank of this channel belt, exhibiting a progressive eastward migration. These channels vary in width and combine to form a broad channel belt. A particular type of low-sinuosity incised channel has been observed within the lower parts of the seismic stratigraphic units, as shown in Figure 2.6, a slice extracted near the base of SU-5, where two northwest-southeast oriented low-sinuosity incised channels are distinguished by their limited lateral migration within channel banks and a relatively constant channel width.

In the middle to upper interval of seismic stratigraphic units, the development of fluvial channels is relatively sparse, typically characterized by medium-scale, highly sinuous morphologies. Figure 2.7 shows a slice through the upper part of SU-4; one medium-scale, highly sinuous meander channel can be observed running in an east-west orientation through the northern portion of the slice. This channel is characterized by pronounced lateral migration and the expansion of point bars and is commonly associated with seismic facies SF-2 in cross-sections. The highly sinuous geomorphic features form an extensive channel belt. Figure 2.8 exhibits one distinctive narrow, highly sinuous channel observed in the slice through the middle part of SU-5. The north-south trending channel remains a relatively consistent width but contributes to a broad channel belt.

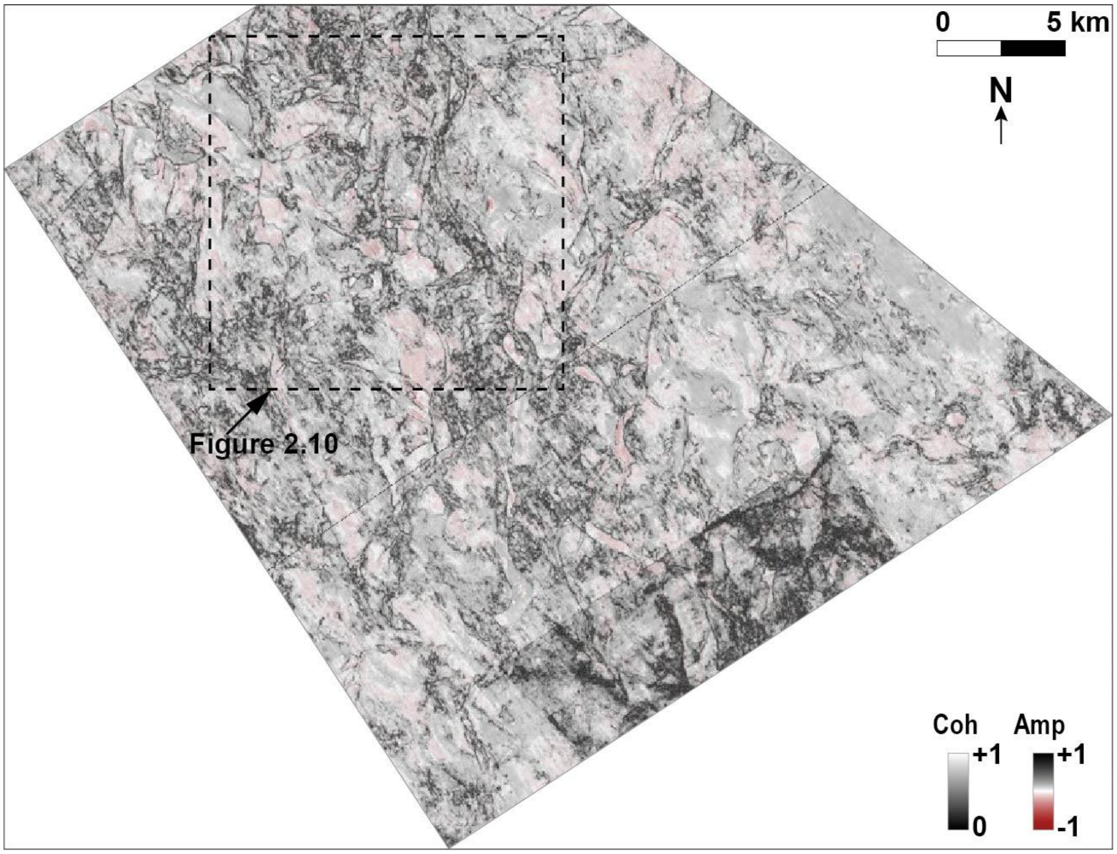

Figure 2.4: One seismic slice extracted from the lower part of SQ-1, co-rendering seismic amplitude with coherence, shows multiple northwest-southeast trending sinuous channel forms intersecting to form a broad channel belt.

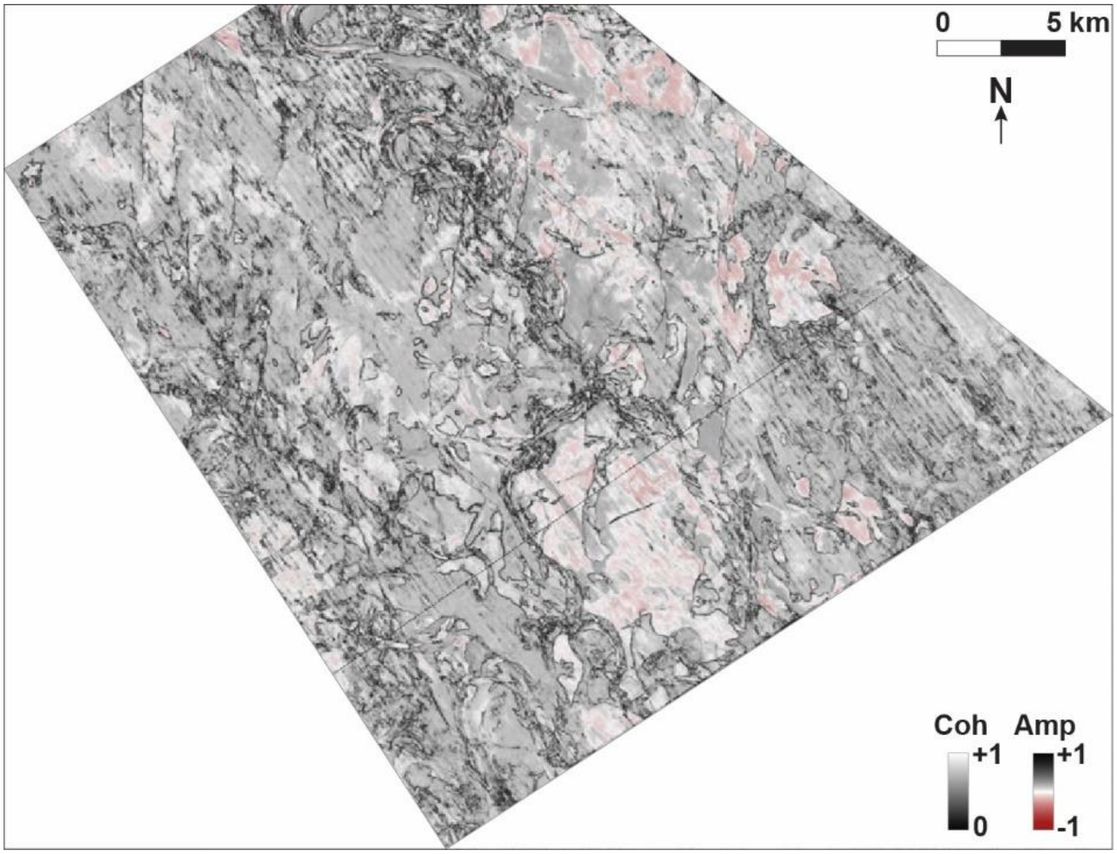

Figure 2.5: One seismic slice extracted from the lower part of SQ-3, co-rendering seismic amplitude with coherence, displays several discontinuous, highly sinuous channel forms or meander loops. Note that lighter tones are associated with amplitude anomalies induced by gas infill. They are common seismic responses in the shallow formations of the Gulf of Thailand.

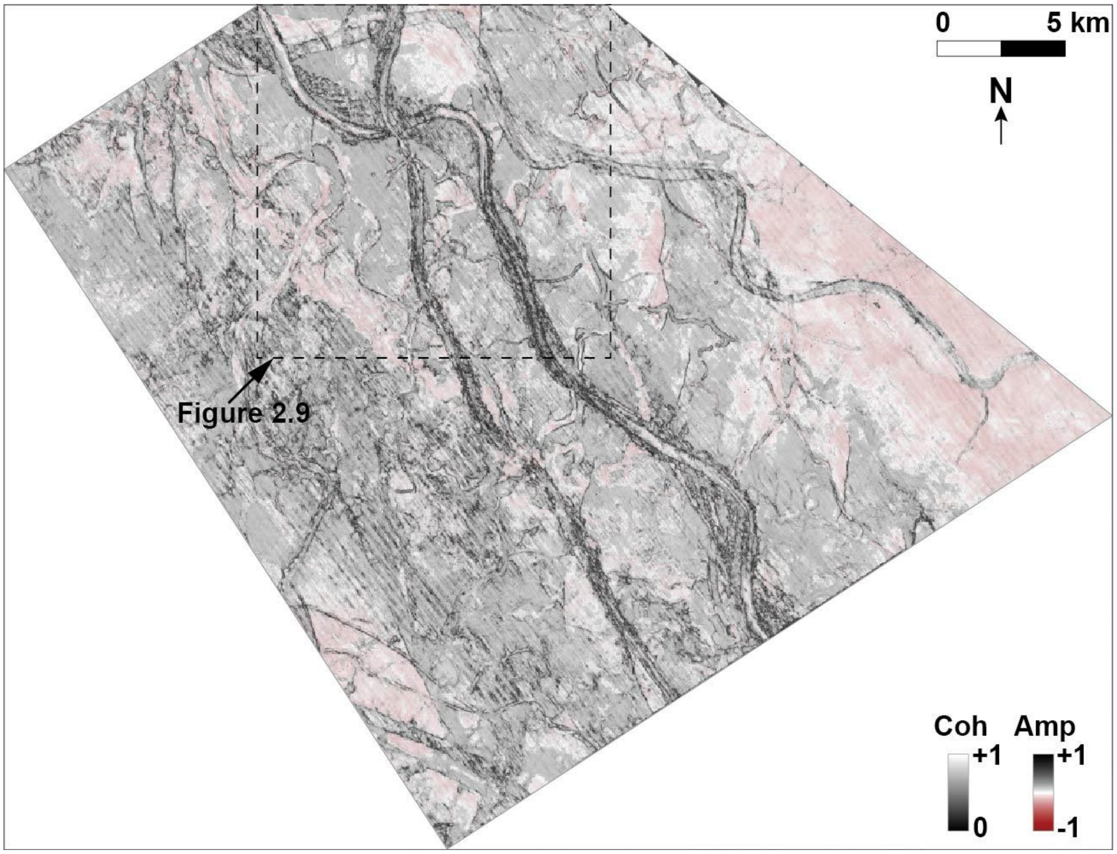

Figure 2.6: One slice extracted approaching the base of SQ-5, co-rendering seismic amplitude and coherence, shows two distinct NW-SE trending low sinuous channel belts running through the whole slice.

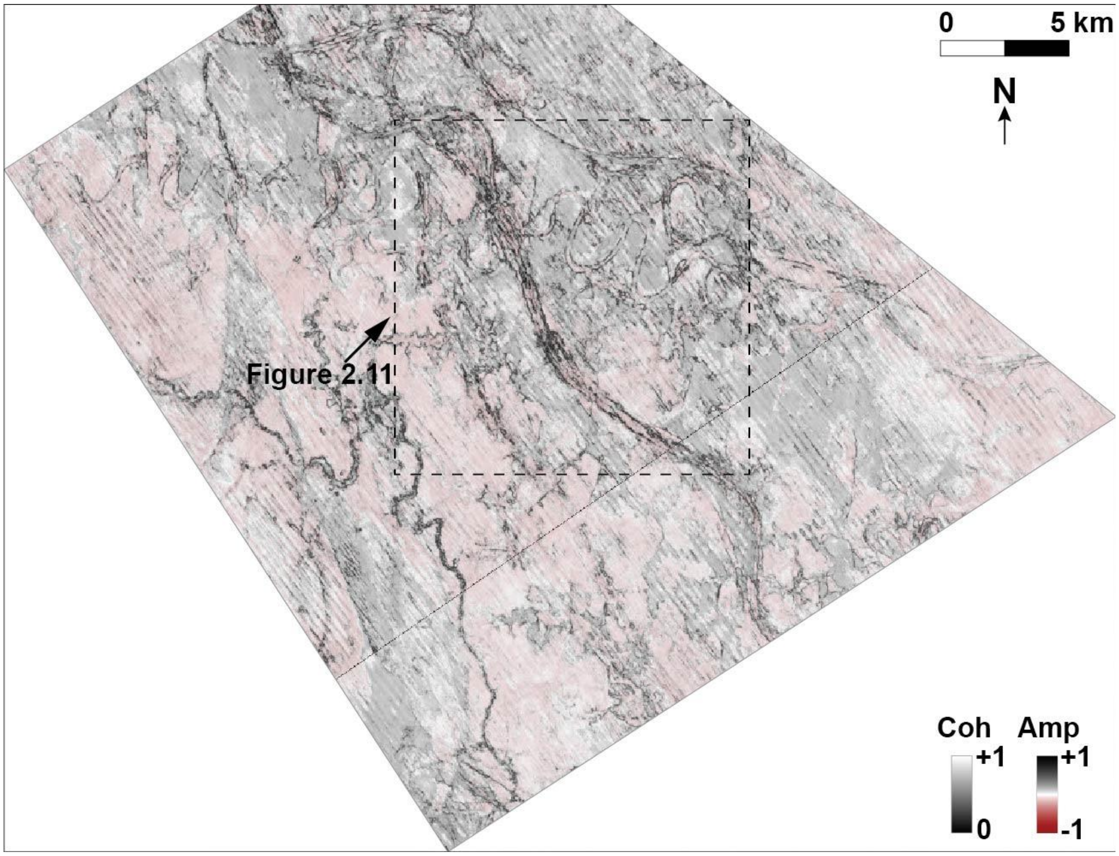

Figure 2.7: One slice extracted from the upper middle of SQ-4, co-rendering with seismic amplitude and coherence, displays one continuous, highly sinuous E-W trending channel form with well-developed side-attached point bars. Note that the two overlying channel belts from SQ-5 (shown in Figure 2.6) are superimposed in this slice; they are non-isochronous and have a high sinuous channel form.

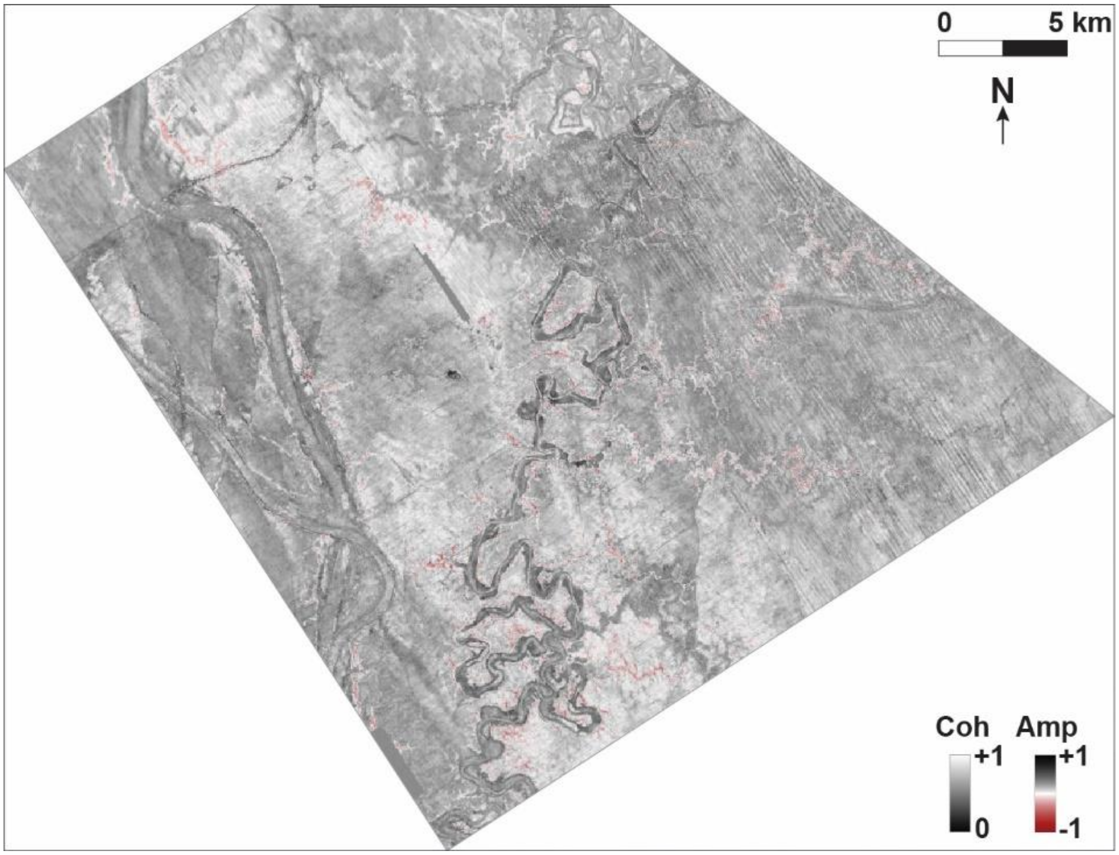

Figure 2.8: One slice extracted from the upper of SQ-5, co-rendering seismic amplitude with coherence, shows one highly sinuous N-S trending channel.

2.5 INTERPRETATIONS

2.5.1 Seismic Sequence Stratigraphy

Five seismic stratigraphic units represent successive stacks of aggradational fluvial succession with marine succession in the study interval from Pliocene to Pleistocene. Each stratigraphic unit corresponds to the smallest seismically identifiable sequence stratigraphic unit, averaging approximately 68 m (223 ft) in thickness. In each seismic sequence stratigraphic unit, the Lowstand Systems Tract (LST) comprises fluvial sedimentary strata above the sequence boundary. They are considered to be deposited in the process that the relative sea-level drops below the coastal plain drive channel incision and lateral migration to create accommodation for sediments, forming broad channel belts or incised channels (Figures 2.4, 2.5, and 2.6). The thickness of fluvial succession varies from 15 to 35 m (49 to 115 ft), and localized position can exceed 50 m (164 ft) corresponding to the deeply incised channels. Subsequent transgressions lead to marine deposits overlaying the fluvial deposits, filling the uppermost part of the fluvial landform depression. These deposits form the thin Transgressive Systems Tract (TST) characterized by confined, laterally continuous weak seismic reflections, typically less than 12 m (39 ft) thick. Continuous parallel reflections above the TST are interpreted as the Highstand Systems Tract (HST), located in the middle to upper parts of the seismic stratigraphic unit. The HST stratigraphic records contain fewer fluvial deposition, and its uppermost section is generally eroded by the base boundary of the subsequent stratigraphic unit, resulting in limited preservation of the late HST. The thickness of the HST ranges from 35 to 70 m (115 to 230 ft), greater than the average fluvial succession thickness, which suggests sustained aggradation of the coastal plain.

The repetition of the stratigraphic evolution process and the well-preserved fluvial depositional strata suggest that the relative sea-level variations primarily control sequence formation in the studied section, which lies in a tectonically stable subsidence setting. This is supported by the stratigraphic characteristic that each seismic stratigraphic unit is constituted by one nearly complete stratigraphic cycle, characterized by fluvial incision and localized accumulation concentrated in local areas of sequence boundaries during the relative sea-level falls, followed by coastal plain aggradation during the relative sea-level rises. Additionally, the vertical stacking of stratigraphic cycles driven by relative sea-level fluctuations introduces another distinctive stratigraphic characteristic, the vertical separation between fluvial deposits and the overlying strata caused by sustained coastal plain aggradation. This is evidenced by significantly greater HST thickness than LST thickness within each unit, with no sequence boundary eroding into the base of the underlying stratigraphic unit. This suggests that significant transgressions allowed coastal plain deposits to accumulate sufficiently thick for channel incision, creating a pronounced vertical separation between the HST and the LST. The low-gradient setting in the study area also contributes to the vertical separation of strata. Studies of paleo river systems in similar environments suggest that river systems across a low-gradient exposed setting likely remain non-incised over large areas when the relative sea-level fall is insufficient to expose the shelf edge (Posamentier et al., 2001; Holbrook et al., 2006). Meander systems above sequence boundaries, as observed in Figure 2.4 and Figure 2.5, would have a longer extension distance and could drive the coastal plain aggradation as the coastline regresses.

2.5.2 Channel Forms and Channel Fills

Successive seismic slices, co-rendering coherence with amplitude, reveal diverse geomorphologic features of the buried fluvial system within stratigraphic units. Based on the style and scale of these features, the observed channel patterns are categorized into three types: incised channel belt, compound channel belt, and single channel belt.

Seismic slices reveal the incised channel belt as a single low-sinuosity channel (sinuosity < 1.2) deeply incised into the underlying strata along the sequence boundary, forming a continuous, nearly straight belt in response to limited lateral migration. Figure 2.9 exhibits two slightly sinuous to straight incised channel belts with average widths of 500 m (2,460 ft) and 750 m (6,562 ft) and an approximate thickness of 50 m (164 ft), associated with U-shaped seismic facies (SF-3) in the cross sections. Incised channel belts commonly have well-defined boundaries and distinct internal channel forms. The geomorphic features within channel belt boundaries reveal three main depositional units: channel fill, point bar, and abandoned channel. Strong to chaotic reflections between the channel belt boundaries and internal channel forms are interpreted as the seismic response of sandy channel bedform fills. Meander scroll trajectories in slices and the sigmoidal reflections (SF-5) in cross-sections indicate point bar clinoforms, suggesting well-preserved point bars. The internal channel forms are interpreted as abandoned channels, resulting from remnant channels filled with fine-grained sediments (Reijenstein et al., 2011). The abandoned channels are characterized by the continuous weak response on slices and concave-down uniform reflections (SF-7) on cross-sections (Toonen et al., 2012; Alqahtani et al., 2015). As an essential part of the fluvial deposit, the abandoned channel retains geomorphic relics of the former channel that formed the channel belt.

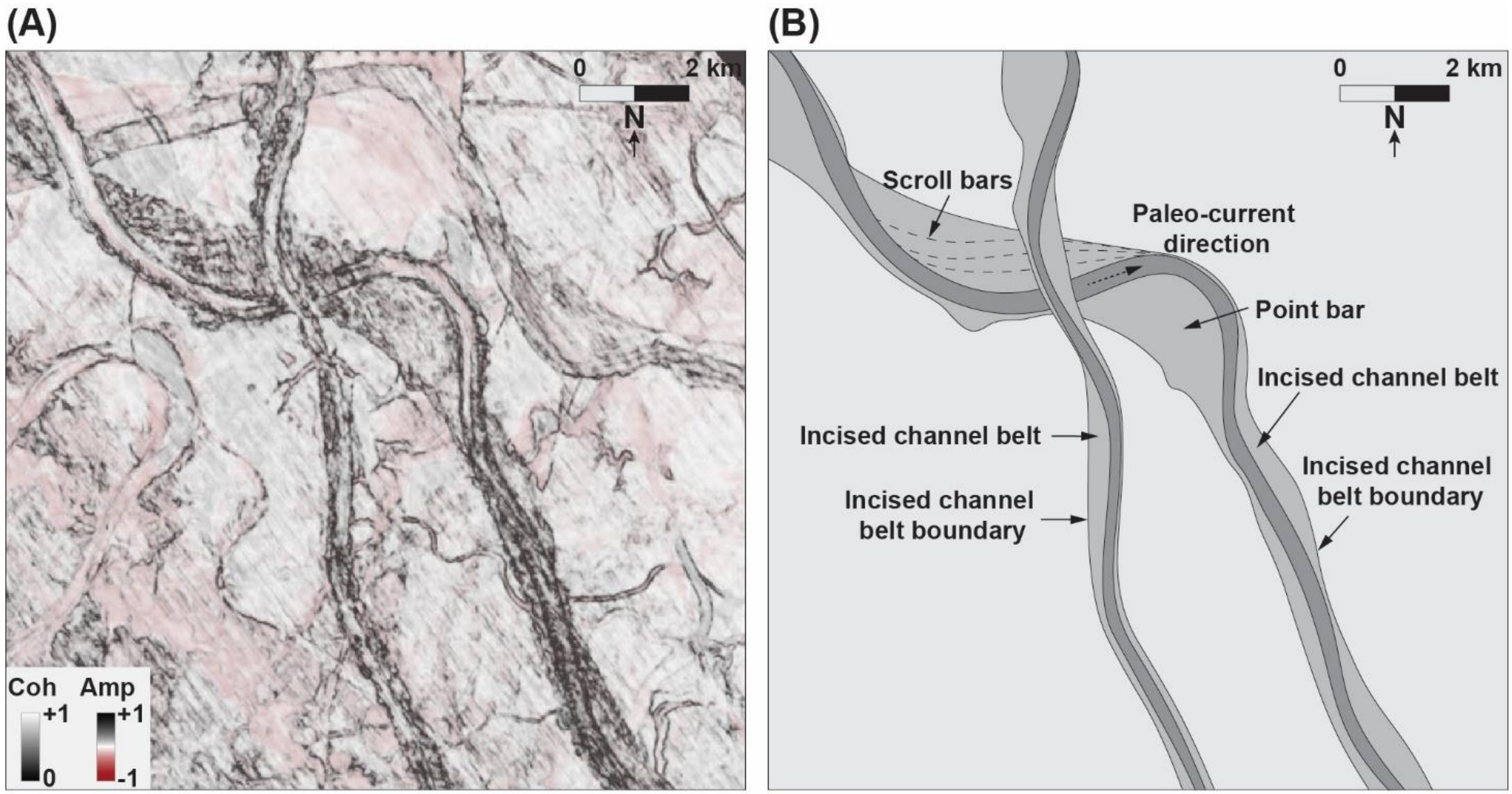

Figure 2.9: (A) A compound channel belt consisting of a cluster of channels superimposed on each other above the sequence boundary of SQ-1. Refer to Figure 2.6 for the location of this slice. (B) An interpretive map delineating the major geomorphic characteristics and seismic geomorphological units.

The compound channel belt is characterized by multiple meander channels in close proximity that intersect and cut through one another. These entangled channels form a broad, low-sinuosity compound channel belt within LST strata. Seismic geomorphic features within channel belt boundaries exhibit irregular, disconnected internal channel forms surrounding bar forms, recorded as channels entangling laterally. Figure 2.10 shows a compound channel belt over 8 km (5 mi) wide and 26 m (85 ft) thick. Half-oval-shaped features in slices, associated with hummocky to chaotic seismic facies (SF-6) in cross sections, are interpreted as point bars formed through lateral accretions. Crescent-shaped geomorphic features surrounding point bars, associated with low-amplitude concave down seismic facies (SF-7) in cross sections, are interpreted as abandoned meander loops that indicate channel expansion and downstream migration. These geomorphic features resemble point bar and oxbow lake landforms in the modern coastal plain meander systems.

The single channel belt represents the sedimentary records of lateral migration of one highly sinuous meandering channel within HST strata. In Figure 2.11, one continuous, high-sinuosity internal channel form with numerous side-attached point bars comprises a slightly sinuous single channel belt of approximately 2 kilometers (1.2 miles) wide. This internal channel form is interpreted as a well-preserved abandoned channel whose geomorphic features conform to the classic meander pattern. Amplitude contrasts accentuate diverse geometries of point bars within the meander loops, including symmetrical, asymmetrical, or elongated forms with a span width of 500 to 2,000 m (1,640 to 6,562 ft).

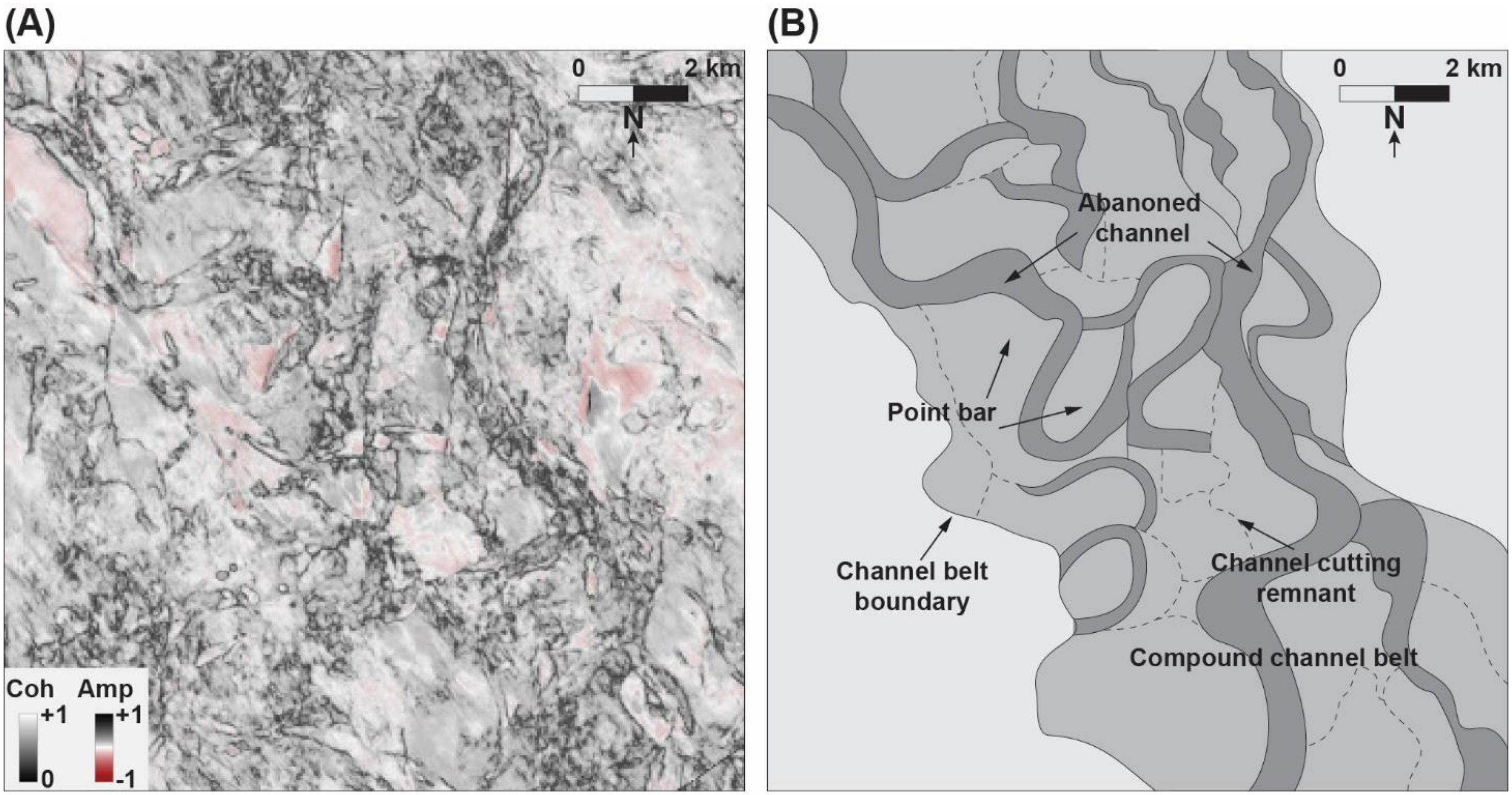

Figure 2.10: (A) Two channel belts incise downward from the base of SQ-5, consisting of channel fills, point bars, and abandoned channels. Refer to Figure 2.4 for the location of this slice. Note that residual scroll bars truncated upstream and converged downstream of the point bar indicate the N-S paleo-current direction. (B) An interpretive map delineating the channel belt geomorphic characteristics and seismic geomorphological units.

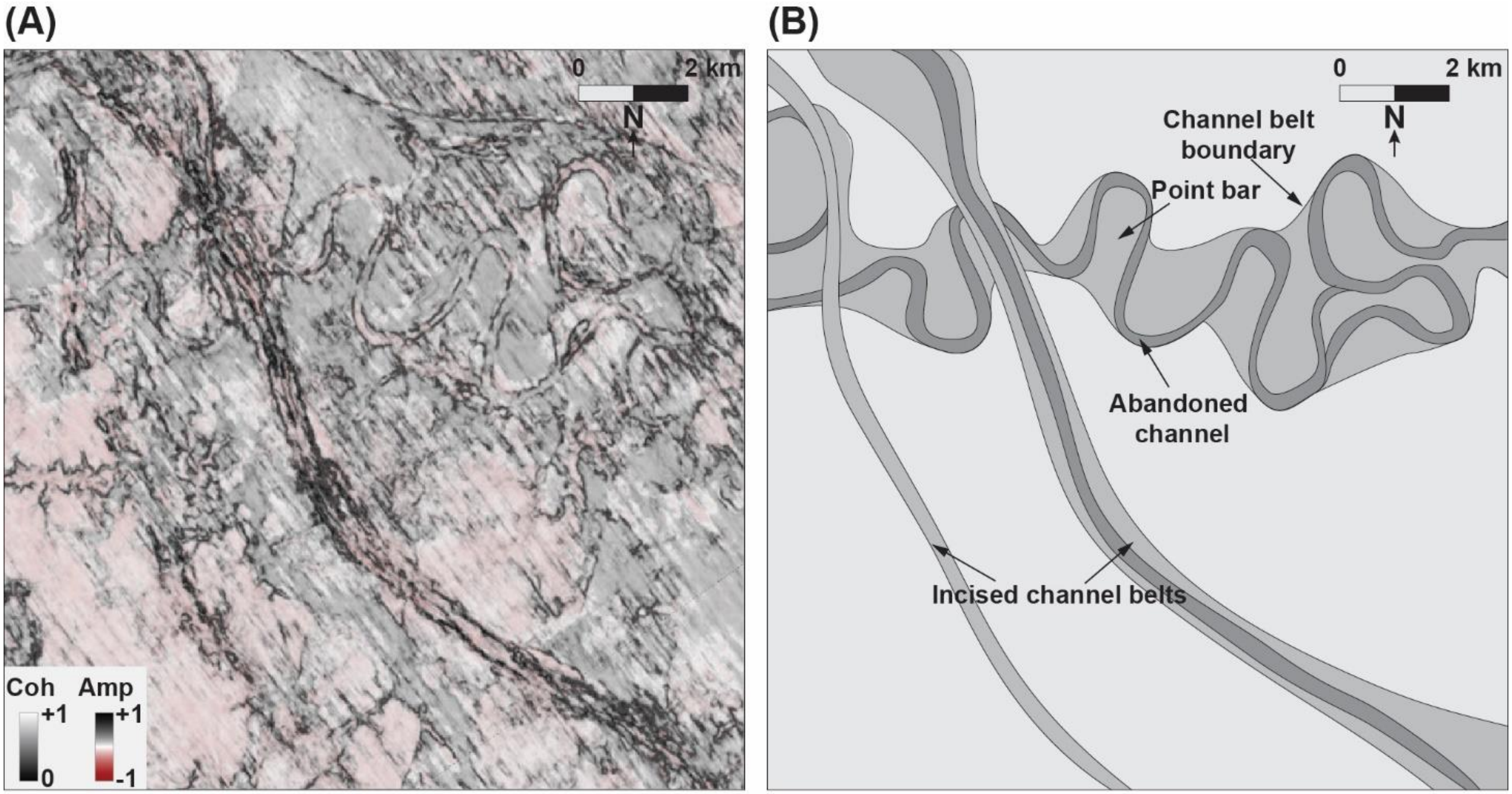

Figure 2.11: (A) A single channel belt containing a continuous, highly sinuous abandoned channel and numerous side-attached point bars. Refer to Figure 7 for the location of this slice. (B) An interpretive map delineating the channel belt geomorphic characteristics and seismic geomorphological units.

2.5.3 Abandoned Channels

Seismic slices reveal the widespread presence of abandoned channels in various channel belts in the study area. Following channel abandonment, flow gradually decreases, and these channels are re-occupied only during overbank flooding from the main channel or transgression events. This is reflected in the channel sedimentary sequence by developing fine-grained sediments preserved as mud plugs in stratigraphic records. On seismic slices (Figure 2.12.A), abandoned channel mud plugs exhibit distinctive continuous channel forms or discontinuous crescent shapes resulting from acoustic impedance contrasts and seismic waveform differences caused by lateral lithologic variations between sandy channel fills and mud plugs. Figure 2.12.B shows the well log calibration results for the abandoned channel on seismic slices, multiple discontinuous crescent-shaped channel forms in a compound channel belt, a mud plug of 8 m (26 ft) thick, encased in 15 m (49 ft) thick channel belt sandstones, produces a localized weak-amplitude concave-down reflection corresponding to internal channel form on the slice (Figure 2.12.C and Figure 2.12.D). Additionally, the cutting relationship with the adjacent channel suggests that this abandoned channel resulted from a path change and subsequent abandonment as the channel migrated southward. The results demonstrate that the seismic geomorphic characteristics of abandoned channel mud plugs are particularly informative, as they provide valuable indicators of channel evolution.

Based on geomorphic characteristics from coherence and spectral decomposition slices, observed abandoned channels are classified into four types: the low-sinuosity single abandoned channel, the high-sinuosity single abandoned channels, the neck-cutoff abandoned channel, and the bifurcation abandoned channel. Referring to the seismic

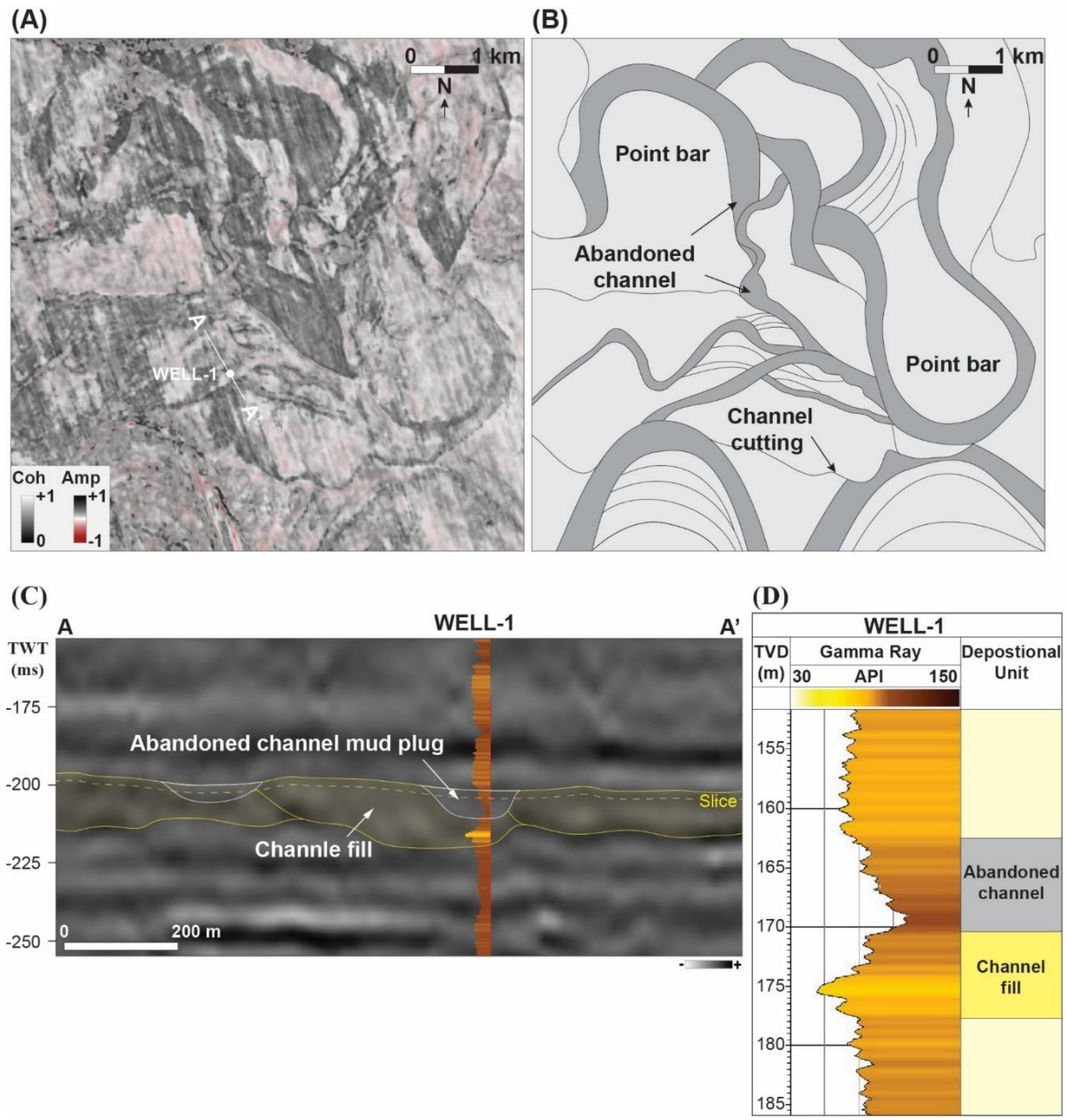

Figure 2.12: (A) Various meander loops and channel forms within a compound channel belt are imaged using co-rendered seismic coherence and amplitude, which highlights the boundaries of abandoned channel mud plugs. (B) An interpretive map delineating the abandoned channels. (C) The seismic cross-section through the well site shows a small-scale channel form with uniform, weak amplitude reflections associated with abandoned channel mud plugs. (D) The well calibration reveals a typical depositional sequence of channel fills with a bell-shaped gamma ray motif, indicating a fining-up sequence. The interval of high gamma ray values aligns with the weak reflections in the seismic cross-section, and the low gamma ray values interval correlates with the strong reflections of the lower part of the channel fill.

geomorphic analysis of the channel (Wood, 2007; Wood and Mize-Spansky, 2009), the ratio of the abandoned channel width (W_{ac}) to the channel belt width (W_{cb}), and the ratio of point bar width (W_{pb}) to abandoned channel width (W_{ac}) are used to quantitatively characterize variations among different types of abandoned channels. The W_{ac}/W_{cb} ratio evaluates the development level of abandoned channels, and the W_{pb}/W_{ac} ratio quantifies the contribution of channel width to its side-attached point bar dimensions before abandonment (Table 2.1).

Table 2.1: Dimensions of abandoned channels and geomorphic features.

	Width (m)	Thick (m)	W_{ac}/W_{cb}	W_{pb}/W_{ac}	
				Avg	Max
Low-sinuosity single abandoned channel	205-385	28-40	0.42	4.66	-
High-sinuosity single abandoned channel	185-230	6-8	0.13	7.84	13.68
Neck cutoff abandoned channel	195-275	6-8	0.20	9.52	11.23
Bifurcation abandoned channel	120-160	5-6	0.27	3.04	6.47

W_{ac}: the abandoned channel width

W_{cb}: the channel belt width

W_{pb}: the ratio of point bar width

(1) Low-sinuosity single abandoned channel

The low-sinuosity abandoned channel is associated with the incised channel on the sequence boundary, which retains low-sinuosity geomorphic features through the entire filling of the incised channel at the last position. The mud plug shows consistently weak seismic responses compared to the varied responses of sandy sedimentary units. Unlike the incised channel belt with varied widths, the low-sinuosity abandoned channel maintains a relatively constant width and ribbon-shaped form within the channel belt. In Figure 2.13, a seismic spectral decomposition slice exhibits two northeast-southwest low-sinuosity (sinuosity <1.2) abandoned channels with relatively constant widths preserved in their incised channel belts of 18 km (11 mi) length. The width of the eastern low-sinuosity abandoned channel remains approximately 285 m (935 ft), while the width of the channel belt expands from 650 to 1,805 m (2,133 to 5,292 ft) in response to point bar development. The average W_{ac}/W_{cb} ratios for the eastern and western low-sinuosity abandoned channels are 0.35 and 0.48, respectively, indicating that mud plugs make up a significant proportion of channel belt deposits. The W_{pb}/W_{ac} ratio is 4.66 for the only point bar on this slice, suggesting that the incised channel primarily acted as a sediment bypass, and the extension of the point bar is limited.

On seismic sections, the low-amplitude (nearly transparent) seismic facies of the U-shaped abandoned channel contrast sharply with the high-amplitude oblique seismic facies associated with lateral accretions of point bar deposits (Figure 2.14). The top of abandoned channels typically shows a concave-up reflection, while localized high amplitudes at the base are likely associated with channel lag deposits. Occasional visible weak chaotic reflections within the abandoned channel represent stratification of the abandoned channel fill, interpreted as products from episodic flooding pulses during the abandonment process (Winkels et al., 2022). The mud plug thickness varies significantly along the paleo-flow thalweg. At the meander bend apex, the low-sinuosity abandoned channel delimits the edge of the channel belt, with a thickness of approximately 28 m (92 ft). Downstream of the meander bend, the thickness of mud plugs increases to approximately 32 m (150 ft). The maximum thickness of approximately 40 m (131 ft) occurs in the straight reach, where the base of the abandoned channel is close to the channel belt base.

(2) High-sinuosity single abandoned channel

The high-sinuosity single abandoned channel is another type of entire abandonment fill formed by one single meandering channel that is filled during the subsequent transgression. The high-sinuosity single abandoned channel shows continuous narrow ribbon-shaped weak seismic responses encased in a slightly sinuous broader channel belt in seismic slices. A significant geomorphic feature of the high-sinuosity single abandoned channel is its coexistence with numerous point bars, which are restricted to elongated string-of-bead geometry by the spatial continuous mud plugs. Figure 2.15 shows a single highly sinuous (sinuosity = 2.8) abandoned channel with a width between 184 and 230 m (604 to 755 ft), encircling at least 11 asymmetrical point bars within a channel belt of 15.4 km (9.6 mi) length. The measurement results at each point bar position show that the channel belt width ranges from 915 to 3,085 km (0.6 to 1.9 mi), with an average of 1,931 m (1.2 mi). High sinuosity results in an average W_{ac}/W_{cb} ratio of 0.13 and an average W_{pb}/W_{ac} ratio of 7.84, indicating intense lateral expansion capability of the channel before abandonment. The mud plug is approximately 6 to 8 m (20 to 26 ft) thick and partitions the upper part of the

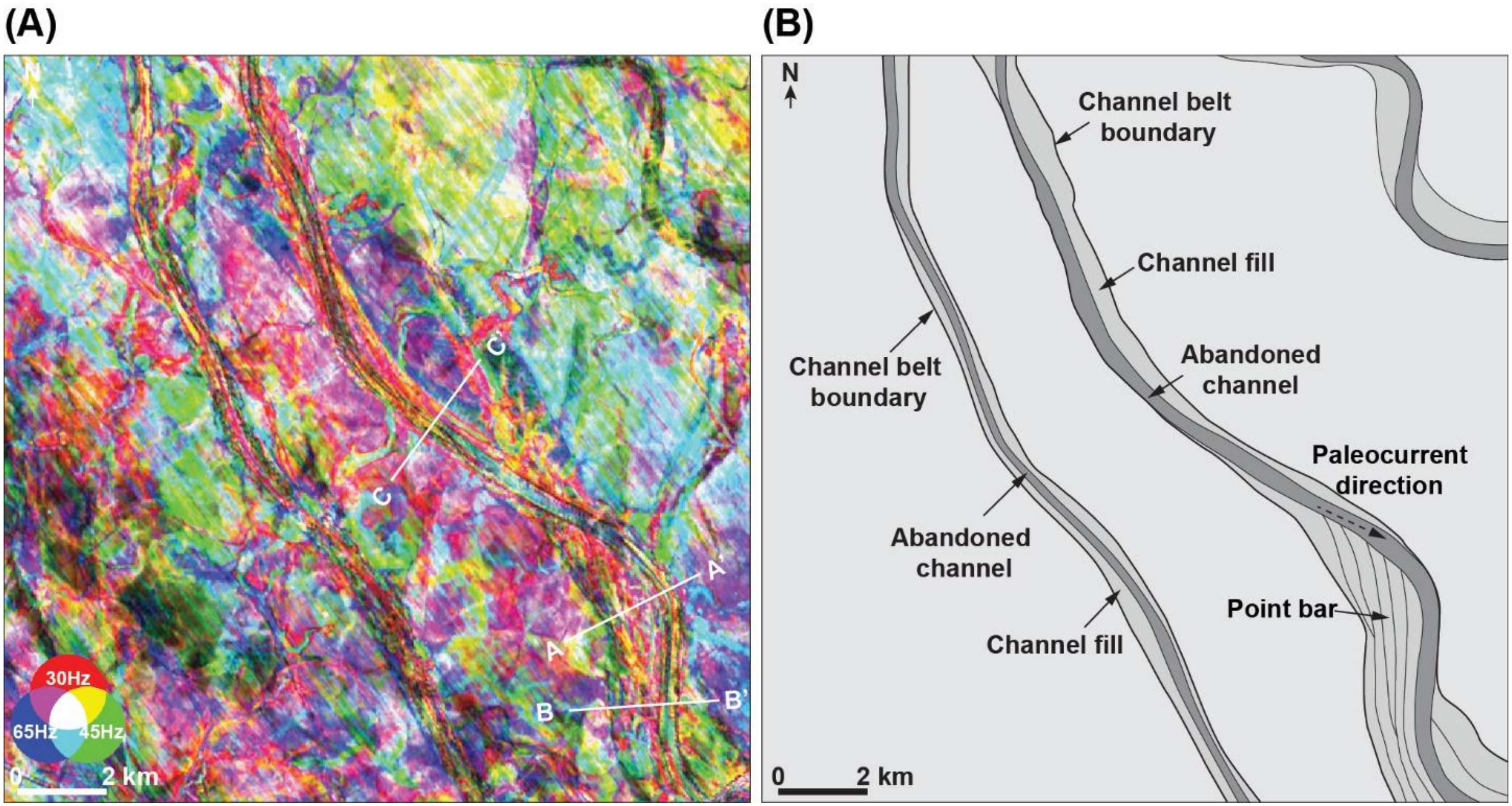

Figure 2.13: (A) Two low-sinuosity single abandoned channels are imaged using RGB blending of 30 Hz, 45 Hz, and 65 Hz frequency components from spectral decomposition. (B) An interpretive map illustrates seismic geomorphological units. Variations in seismic geomorphological units' seismic responses highlight channel fill, abandoned channels, point bars, scroll bars, and channel belt boundaries. The response of the abandoned channel mud plugs appears as continuous ribbon shapes within the channel belt boundaries.

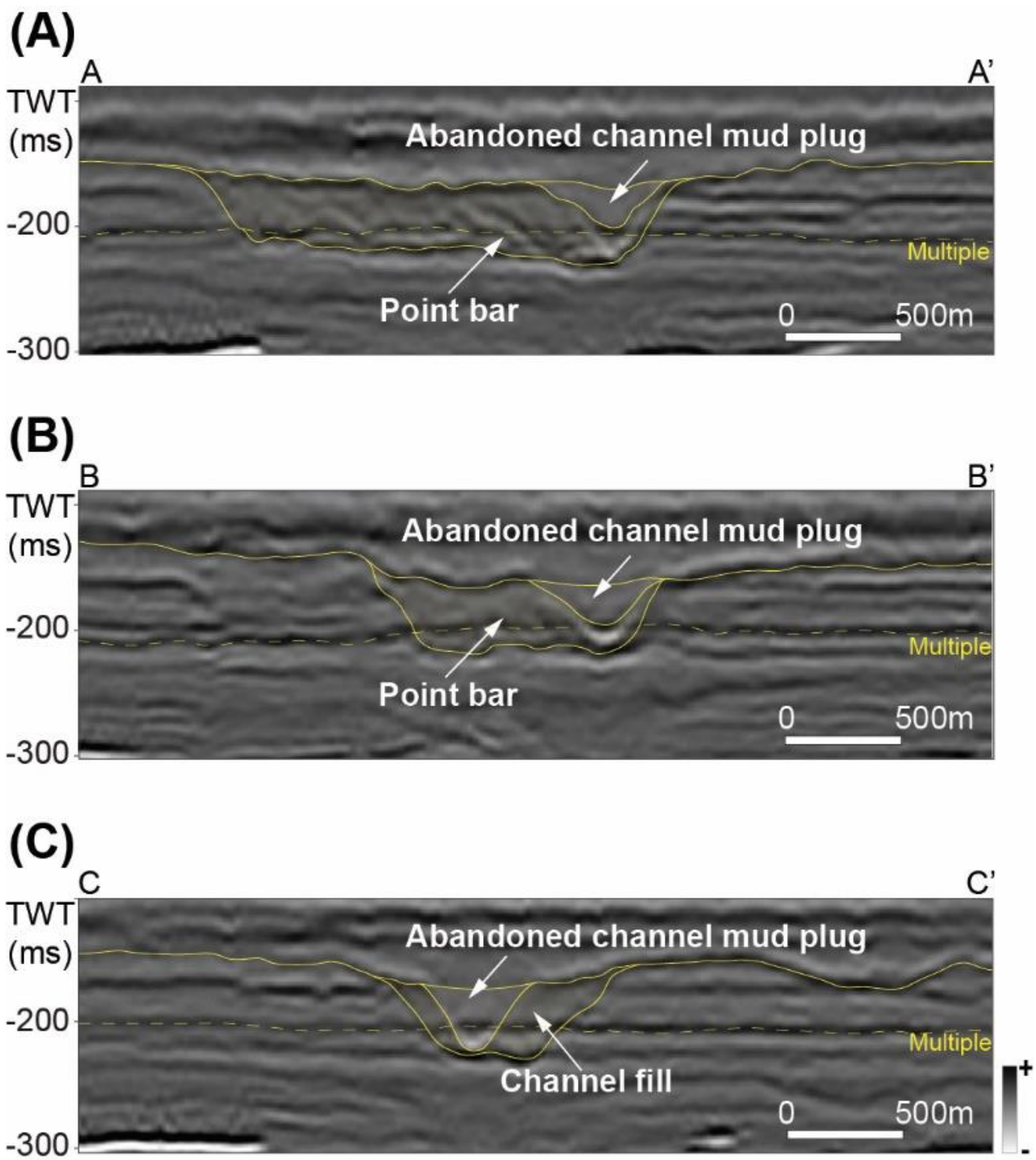

Figure 2.14: Variation in thickness of the abandoned channel mud plugs at different sites along the meander bend. Refer to Figure 13 for the location of sections. (A) At the apex of the meander bend, the base of the abandoned channel mud plugs is approximately 1/2 depth down from the top of the channel belt. (B) At the inflection point, the base of the abandoned channel mud plugs deepens slightly. (C) In the straight reach, the base of the abandoned channel mud plugs approaches the channel bed.

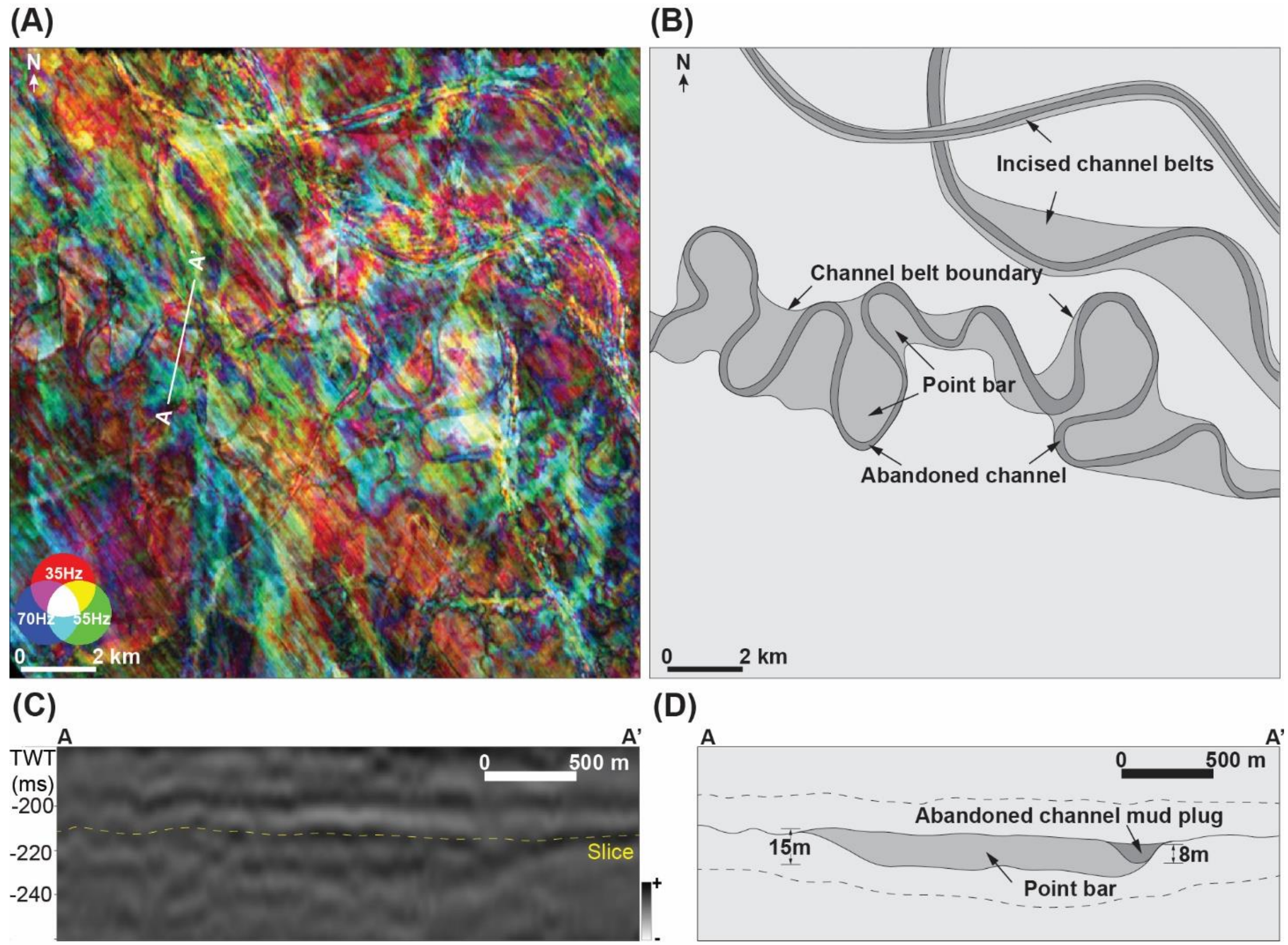

Figure 2.15: (A) A high-sinuosity single abandoned channel is imaged using RGB blending of 35 Hz, 55 Hz, and 70 Hz frequency components from spectral decomposition. (B) An interpretive map illustrates the abandoned channel and side-attached point bars, exhibiting a highly sinuous, continuous ribbon shape. (C) Uninterpreted and (D) interpreted cross-section through the channel belt show the base of the abandoned channel mud plugs positioned approximately 1/2 depth down from the top of the channel belt.

channel belt sandstone with 15 m (43 ft) thick.

(3) Neck cutoff abandoned channel

Seismic decomposition slices indicate that the neck cutoff is the most common type of channel avulsion abandonment in compound channel belts developed above sequence boundaries. As meander channels migrate, the current breaches the meander bend and cuts off the neck to form a new path, leaving the former channel abandoned. These abandoned channels fill with fine-grained material through subsequent overbank processes and transgressions, eventually preserved as mud plugs (Toonen et al., 2012; Durkin et al., 2017). On seismic slices, the neck cutoff abandoned channels appear as discontinuous crescent-shaped or S-shaped meander loops, delimiting the lenticular point bars. Figure 2.16 illustrates numerous crescent-shaped neck cutoff abandoned channels encircling point bars, constituting a compound channel belt over 9 km (5.6 mi). These neck cutoff abandoned channels appear as meander loops that constrain and mirror the size and shape of adjacent point bars. Most point bars exhibit an asymmetrical downstream-migrating pattern, and the axial direction of the neck cutoff abandoned channels indicates the elongation direction of point bars. Measurements of 12 relatively complete meander loop forms show that the neck cutoff abandoned channels are 185 to 335 m (607 to 1,099 ft) wide, and the average W_{ac}/W_{cb} ratio is 0.20. Well-preserved point bars span 1,470 m to 2,905 m (0.9 to 1.8 mi), with a maximum W_{pb}/W_{ac} ratio of 11.23. These two ratios suggest that even though abandoned channel mud plugs constitute a significant proportion of the channel belt, they can form abundant, large-scale point bars before abandonment. The neck cutoff mud plugs are generally 6 to 8 m (20 to 26 ft) thick and primarily occupy the upper part of the 10 m (33 ft) thick compound channel belt sandstone.

(4) Bifurcation abandoned channel

The bifurcation abandoned channel represents another avulsion abandonment observed in HST fluvial records. It occurs when rapid avulsive channel shifting causes the active channel to split into two pathways, abandoning the former branch as flow shifts into a new route (Kleinhans et al., 2013). Unlike the neck cutoff abandoned channel, which encloses only one point bar, the bifurcation abandoned channel contains multiple point bars because of the abandonment of one reach. In Figure 2.17, two extremely sinuous (sinuosity > 10) narrow ribbon-shaped bifurcation abandoned channels with an average width of 130 m (427 ft) surrounding multiple point bars formed two high-sinuosity channel belts of average 511 m (1,677 ft) wide. Measurements at 12 meander loop sites show that the average W_{ac}/W_{cb} ratio is 0.27, and the average W_{pb}/W_{ac} ratio is 3.04. The mud plugs of the bifurcation abandoned channel are approximately 5 to 6 m (16 to 20 ft) thick, occupying two-thirds of the upper part of its 10 m (33 ft) thick channel belt sandstone. The cross-section shows that these mud plugs are slightly thinner than those of the subsequent abandoned channel that avulsed them, likely due to the higher energy of the later channel.

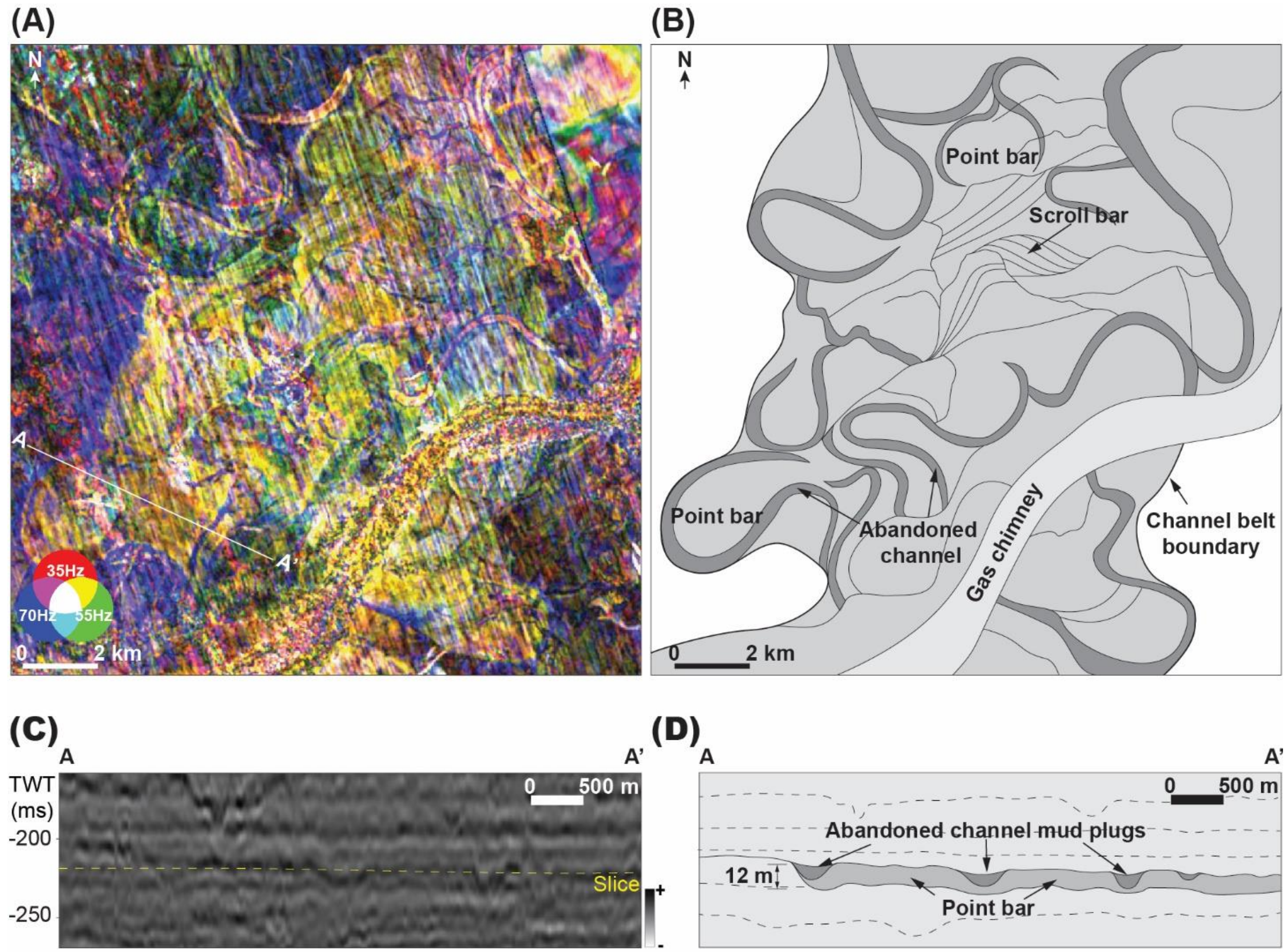

Figure 2.16: (A) Numerous neck cutoff abandoned channels are imaged by RGB blending of 30 Hz, 50 Hz, and 70 Hz frequency components from spectral decomposition. (B) An interpretive map illustrates that the abandoned channel exhibits discontinuous, crescent-shaped forms encased within the channel belt. (C) An uninterpreted and (D) interpreted cross-section through the channel belt shows that the abandoned channel mud plugs occupy the upper part of the channel belt.

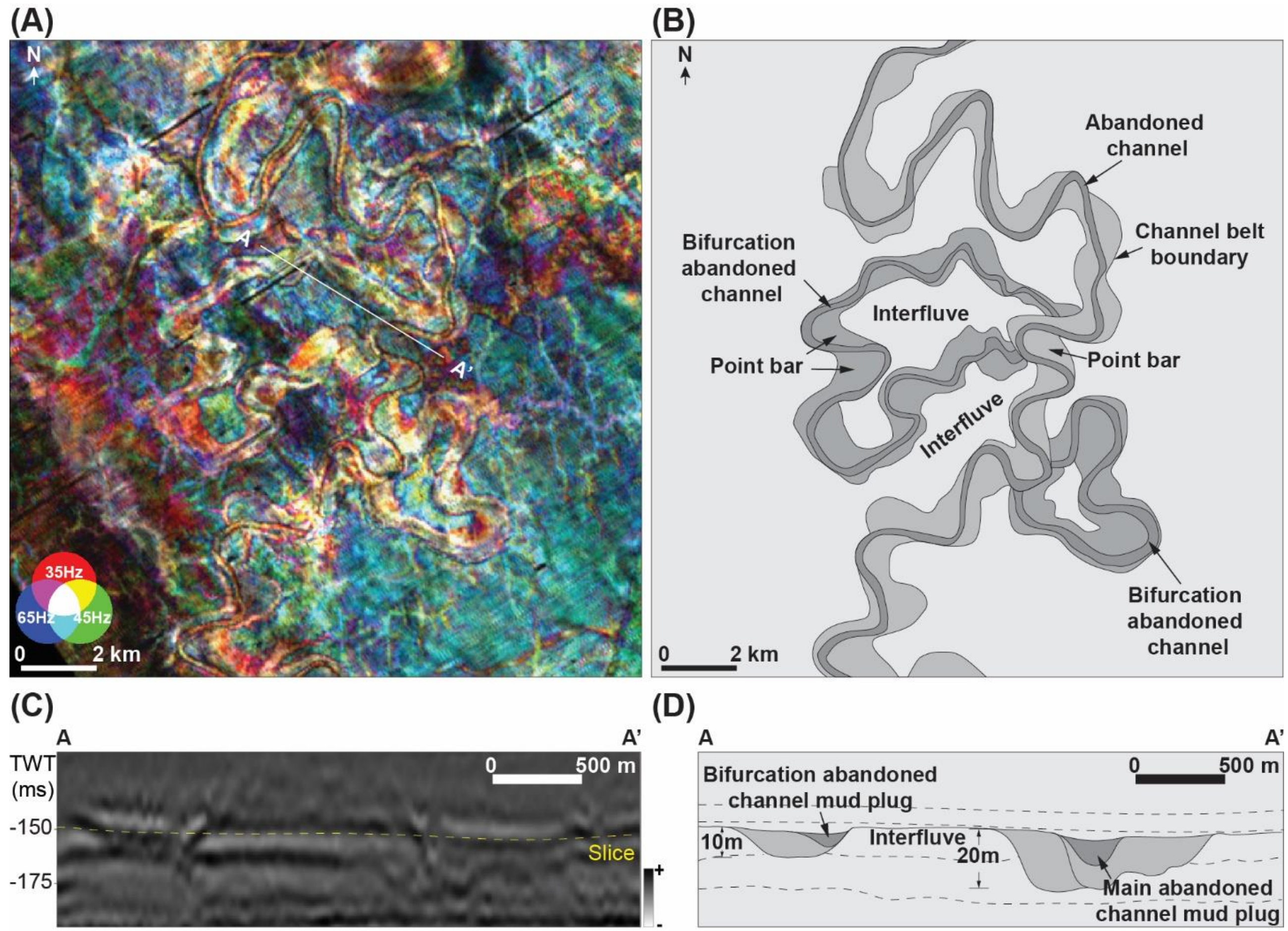

Figure 2.17: (A) Two bifurcation abandoned channels are imaged using RGB blending of 35 Hz, 45 Hz, and 65 Hz frequency components from spectral decomposition. (B) An interpretive map shows that the bifurcation abandoned channels exhibit a continuous ribbon shape and encircle multiple point bars. (C) an uninterpreted and (D) interpreted cross-section through the channel belt shows that the abandoned channel mud plugs occupy the upper half of the channel belt.

2.6 DISCUSSION

2.6.1 Recognition of Abandoned Channel

The seismic visibility of abandoned channels relies on data availability and the completeness of their imaging in seismic slices. Data availability refers to the extracted seismic attributes that can highlight the contrast in acoustic impedance or waveform between the abandoned channel mud plugs and the context of channel belt sandstone (Figure 2.12). This study utilizes the feature that the horizontal dimensions of mud plugs are much larger than their vertical dimensions, which increases their visibility on seismic attribute slices, to address the challenge of their subtle seismic response of being difficult to recognize on seismic profiles because of their smaller scale (Zeng et al., 2007, 2010). Imaging completeness requires that seismic slices capture as many seismic geomorphic characteristics of mud plugs as possible, enabling comparisons with depositional modes (Ghinassi et al., 2016; David et al., 2019) and satellite imagery of modern abandoned channels. Based on seismic geomorphological observation, four recognition criteria can be used to identify abandoned channels:

(1) On seismic slices, abandoned channel mud plugs appear as continuous sinuous channel forms or as discontinuous meander loops and crescent shapes encased in low-sinuosity channel belts. The geometric contrast between the abandoned channels and the channel belt frequently makes the higher sinuous abandoned channels prominent.

(2) On seismic slices, abandoned channel mud plugs exhibit a relatively consistent width compared to channel belts with variable lateral extents. This consistency enhances the identifiability of abandoned channels, particularly in single and incised channel belts.

(3) On seismic sections, abandoned channel mud plugs are evident as U-shaped features consistently positioned in the middle to upper parts of channel belt responses. Laterally, they are adjacent to the downdip terminations of oblique or chaotic reflections.

(4) Abandoned channel mud plugs show weak or transparent seismic responses in contrast to the variable continuity and intensity of reflections from sandy channel fills. On seismic sections, subtle waveform variations within the continuous strong reflections from channel belt sandstone can serve as a reference for identifying abandoned mud plugs.

A common pitfall in 3-D seismic interpretation of fluvial systems is assuming that channel patterns imaged on seismic data are homogeneous sand-prone depositional units. This study reveals that the channel forms within channel belts in the study area tend to be mud plugs. This finding provides valuable insights for interpreting seismic geomorphology in conventional seismic data with low resolution. In floodplain fluvial depositional systems, frequent overbank events significantly reduce the impedance difference between the channel fills and interfluve deposits. In contrast, the impedance difference between abandoned channel mud plugs and channel fills is more pronounced, causing mud plugs to appear as discontinuous channel forms on conventional seismic data.

2.6.2 Abandoned Channel Preservation Potential

The variety of abandoned channel types observed suggests a high preservation potential for abandoned channel mud plugs in the study area. Low-gradient topography and long-term transgression in the study area are considered to be critical factors enhancing the preservation potential of abandoned channels. Seismic interpretation reveals that the study section is formed in a stable tectonic subsidence setting, the topographic slope is less than 1 degree, dipping slightly to the southeast, and the paleo shelf edge is located several hundred kilometers downstream southeast of the study area. This means minor relative sea-level fluctuations can have a greater horizontal impact on stratigraphic deposition and lead to significant shoreline shifts in a low-gradient setting. In the study area, fluvial aggradation has not experienced considerable erosion during rapid shoreline shifts, either seaward with the relative sea-level fall or landward with the relative sea-level rise. This is evidenced by the absence of some key indicators in the study section, including sedimentary records related to tidal action, or delta-related progradation reflections between marine deposits and fluvial deposits in each seismic sequence stratigraphic unit. The stratigraphic architecture of the studied section shows that fluvial deposits are primarily concentrated at sequence boundaries, which extend laterally from the base of channel belts through the interfluves and merge upward into the maximum flooding surface. The TST deposits are confined to the tops of fluvial low landforms at the sequence boundaries and are overlain by thick HST deposits. These characteristics suggest that marine deposition primarily drives stratigraphic aggradation during relative sea-level transgressions. The high-frequency sea-level curve from the Pliocene to the present (Miller et al., 2020) exhibits a pattern of rapid sea level rises followed by slow falls, with falling stages lasting longer ages. Although there is no valid data correlating seismic stratigraphic units with the sea level curve, the stratigraphic architecture suggests a similar pattern to the sea-level curve. Thus, long-term transgression in the study area increases the preservation potential of abandoned channels.

2.6.3 Implications for Reservoir Heterogeneity

This study indicates that various abandoned channel mud plugs strongly impact the lateral heterogeneity of reservoir lithology. These mud plugs constitute a significant proportion of the incised and compound channel belt sandstones, with a more substantial impact on the lateral lithologic heterogeneity than interfluve muddy deposits. In the incised channel belt, abandoned channel mud plugs make up a significant portion of channel belt deposits and show high continuity, significantly increasing the heterogeneity of the channel belt sandstones. As shown in Figure 2.13, the only point bar in this slice has a moderate W_{pb}/W_{ac} ratio of 4.66, suggesting the development abundance and extent of point bars are limited. In contrast, continuous abandoned mud plugs have an average W_{ac}/W_{cb} ratio of up to 0.42, giving rise to strong lithologic heterogeneity. In compound channel belts, numerous neck cutoff abandoned channel mud plugs and the high W_{pb}/W_{ac} ratio usually indicate intense lateral channel migration and constitute a large proportion of channel belt sandstones. As exhibited in Figure 2.15, the neck cutoff abandoned channels have an average W_{pb}/W_{ac} ratio of 9.52 and an average W_{ac}/W_{cb} ratio of up to 0.20, and their discontinuous distribution further complicates sandstone heterogeneity. Bifurcation abandonment expands the lateral extent of high-sinuosity channel belts, whereas mud plugs and interfluve deposits significantly increase channel belt sandstone heterogeneity. As shown in Figure 2.17, although the bifurcation abandoned channels extend the belt width to 2.7 km (1.7 miles), they also yield additional interfluve area. The lower average W_{pb}/W_{ac} ratio of 3.04 suggests that the extension of point bars is limited, and the average W_{ac}/W_{cb} ratio of 0.27 indicates that mud plugs further intensify lateral lithologic heterogeneity.

Building on studies of modern deposits and outcrops (Donselaar and Overeem, 2008; Dépret et al., 2017), this study reveals that most abandoned channel mud plugs within various channel belts act as partial barriers, significantly reducing the connectivity of the upper half to two-thirds of channel belt sandstones. This impact is more pronounced in incised channel belts, where mud plugs can sometimes form nearly complete barriers. In compound channel belts, numerous discontinuous crescent-shaped mud plugs are encased in the middle to upper parts of channel belts, acting as lateral barriers to adjacent sandy point bars (Figure 2.12.C, Figure 2.16.C, and Figure 2.16.D). The lower parts of the channel belt sandstones remain connected through channel floor sandstones. Consequently, the connectivity of the channel belt sandstones is significantly reduced as they are partitioned into partially isolated lenticular sandbodies. In high-sinuosity channel belts, mud plugs, despite only occupying the upper half of sandstones, exhibit excellent continuity, leading to the separation of the upper part of point bars into oval-shaped sandbodies and significantly impacting their connectivity (Figure 2.15.C and Figure 2.15.D). In the incised channel belts, the impact of abandoned mud plugs on connectivity is not confined to the upper parts of channel belt sandstones. In some straight reaches, the mud plugs approach the channel bed, with a thickness slightly less than that of channel belt sandstones, where the mud plugs act as barriers, partitioning the channel belt sandstones into nearly isolated ribbon-shaped sandbodies, significantly reducing their connectivity (Figure 2.14.C). The results of this study highlight the impact of abandoned channel mud plugs on the complexity of fluvial systems and serve as a valuable reference for characterizing reservoir heterogeneity and reservoir modeling.

2.7 CONCLUSIONS

The Pliocene to Pleistocene strata in the North Malay Basin contain plenty of fluvial systems deposited in a low-gradient coastal plain setting. Abandoned channel mud plugs, as a crucial component of the fluvial depositional system, constitute a significant portion of the channel belt sandstones. This study integrates seismic sequence stratigraphy interpretation with seismic geomorphic analysis of high-resolution 3-D seismic data, employing seismic coherence and spectral decomposition data to evaluate the characteristics and dimensions of abandoned channel mud plugs.

A detailed interpretation of the uppermost 500 ms of the seismic data reveals five seismic sequence stratigraphic units that allow image seismic geomorphology of fluvial depositions associated with different systems tracts, each averaging approximately 68 m (223 ft) thick. A large number of abandoned channels are preserved as mud plugs in the stratigraphic records. Four distinct types of abandoned channels are interpreted: (1) Low-sinuosity single abandoned channels commonly occur as continuous, low-sinuosity, ribbon-shaped channel forms within low-sinuosity incised channel belts, measuring about 205 to 385 m (673 to 1263 ft) wide and 28 to 40 m (92 to 131) thick. These mud plugs account for a significant proportion of the channel belt sandstones, with a W_{ac}/W_{cb} ratio of 0.42, but correspond to a relatively low level of point bar development, indicated by the W_{pb}/W_{ac} ratio of 4.66. (2) High-sinuosity single abandoned channels occur as continuous, narrow, high-sinuosity ribbon-shaped channel forms within broad low-sinuosity channel belts. Their mud plugs are typically approximately 200 m (656 ft) wide and 8 m (26 ft) thick, with a smaller W_{ac}/W_{cb} ratio of 0.13. Almost every meander loop of mud plug encircles a point bar, with a high average W_{pb}/W_{ac} ratio of 7.84. (3) Neck cutoff abandoned channels, as the most common form of abandonment, are widely developed within compound channel belts. Discontinuous, crescent-shaped mud plugs significantly complicate the channel belt sandstones. The mud plugs exhibit variable dimensions, ranging from less than 195 to 275 m (640 to 902 ft) wide and less than 8 m (26 ft) thick. The W_{ac}/W_{cb} ratio can reach 0.20, and the W_{pb}/W_{ac} ratio can be as high as 11.23. (4) Bifurcation abandoned channels are exclusively found in high-sinuosity single channel belts, characterized by abandoning a channel belt segment containing multiple point bars. Mud plugs of bifurcation abandoned channels are less than 160 m (525 ft) wide and 6 m (20 ft) thick, with an average W_{ac}/W_{cb} ratio of 0.27 and an average W_{pb}/W_{ac} ratio of 3.04.

Abandoned channel mud plugs constitute a significant portion of channel belt sandstones in the study area. Most abandoned channel mud plugs act as partial barriers, significantly impacting the connectivity of the upper half to two-thirds of the channel belt sandstones. This barrier effect is more pronounced in incised channel belt sandstones, where they can form complete barriers in specific straight channel segments. Consequently, abandoned channel mud plugs greatly complicate the connectivity of channel sandstones and significantly impact the intermediate-scale reservoir heterogeneity.

ACKNOWLEDGMENTS

We sincerely thank PTT Exploration and Production Public Company Limited (PTTEP) for providing data for this study and for permission to publish this paper. We also extend our grateful gratitude to Dr. John D. Pigot for his valuable guidance, and to Dr. Matthew J. Pranter for his initial review. We appreciate the technical support provided by AASPI software from the University of Oklahoma and Petrel software from SLB.

REFERENCES

Allen, J. R. L., 1965, A review of the origin and characteristics of recent alluvial sediments: Sedimentology, v. 5, p. 89–191.

Alqahtani, F. A., H. D. Johnson, C. A. L. Jackson, and, M. R. B. Som, 2015, Nature, origin and evolution of a Late Pleistocene incised valley–fill, Sunda Shelf, Southeast Asia: Sedimentology, v. 62, p. 1198–1232.

Bidorn, B., K. Sok, K. Bidorn, and W. C. Burnett, 2021, An analysis of the factors responsible for the shoreline retreat of the Chao Phraya Delta (Thailand): Science of the Total Environment, v. 769, p. 145253.

Bos, J. A. A., R. Dambeck, A. J. Kalis, A. Schweizer, and H. Thiemeyer, 2008, Palaeoenvironmental changes and vegetation history of the northern Upper Rhine Graben (southwestern Germany) since the Late glacial: Netherlands Journal of Geosciences, v. 87, no. 1, p. 67–90.

Castagna, J. P., and S. Sun, 2006, Comparison of spectral decomposition methods: First Break, v. 24, no. 3, p. 75–79.

Chaiwongsaen, N., P. Nimnate, and M. Choowong, 2019, Morphological changes of the Lower Ping and Chao Phraya Rivers, North and Central Thailand: flood and coastal equilibrium analyses: Open Geosciences, v. 11, no.1, p. 152–171.

Chopra S., and K. J. Marfurt, 2016, Spectral decomposition and spectral balancing of seismic data: The Leading Edge, v.35, no. 2, p.176–179.

Chopra, S., and K. J. Marfurt, 2018, Coherence attribute applications on seismic data in various guises—Part 1: Interpretation, v. 6, no. 3, p. T521–T529.

Colombera, L., N. P. Mountney, C. E. Russell, M. N. Shiers, and W. D. McCaffrey, 2017, Geometry and compartmentalization of fluvial meander–belt reservoirs at the bar–form scale: Quantitative insight from outcrop, modern and subsurface analogues: Marine and Petroleum Geology, v. 82, p. 35–55.

Constantine, J. A., and T. Dunne, 2008, Meander cutoff and the controls on the production of oxbow lakes: Geology, v. 36, no.1, p. 23–26.

Constantine, J. A., T. Dunne, H. Piegay, and G. Mathias Kondolf, 2010, Controls on the alluviation of oxbow lakes by bed–material load along the Sacramento River, California: Sedimentology, v. 57, no. 2, p. 389–407.

Cosma, M., M. Ghinassi, A. D'Alpaos, M. Roner, A. Finotello, L. Tommasini, and R. Gatto, 2019, Point–bar brink and channel thalweg trajectories depicting interaction between vertical and lateral shifts of microtidal channels in the Venice Lagoon (Italy): Geomorphology, v. 342, p. 37–50.

Darmadi, Y., B. J. Willis, and S. L. Dorobek, 2007, Three–dimensional seismic architecture of fluvial sequences on the low–gradient Sunda Shelf, offshore Indonesia: Journal of Sedimentary Research, v. 77, no. 3, p. 225–238.

David, S. R., J. A. Czuba, and D. A. Edmonds, 2019, Channelization of meandering river floodplains by headcutting: Geology, v. 47, no. 1, p. 15–18.

Dépret, T., J. Riquier, and H. Piegay, 2017, Evolution of abandoned channels: Insights on controlling factors in a multi–pressure river system: Geomorphology, v. 294, p. 99–118.

Donselaar, M. E., Overeem, I., 2008. Connectivity of fluvial point–bar deposits: An example from the Miocene Huesca fluvial fan, Ebro Basin, Spain. AAPG Bulletin, v. 92, no. 9, p. 1109–1129.

Durkin, P. R., R. L. Boyd, S. M. Hubbard, A. W. Shultz, and M. D. Blum, 2017, Three–dimensional reconstruction of meander–belt evolution, Cretaceous McMurray Formation, Alberta Foreland Basin, Canada: Journal of Sedimentary Research, v. 87, no. 10, p. 1075–1099.

Gersztenkorn, A., and K. J. Marfurt,1999, Eigenstructure–based coherence computations as an aid to 3–D structural and stratigraphic mapping: Geophysics, v. 64, no. 5, p. 1468–1479.

Ghinassi, M., A. Ielpi, M. Aldinucci, and M. Fustic, 2016, Downstream–migrating fluvial point bars in the rock record: Sedimentary Geology, v. 334, p. 66–96.

Goupillaud, P, A. Grossmann, and J. Morlet. 1984, Cycle–octave and related transforms in seismic signal analysis: Geoexploration, v. 23, no. 1, p. 85–102.

Gray, A. B., G. B. Pasternack, E. B. Watson, and M. A. Goni, 2016, Abandoned channel fill sequences in the tidal estuary of a small mountainous, dry–summer river: Sedimentology, v. 63, no. 1, p. 176–206.

Holbrook, J., R. W. Scott, and F. E. Oboh-Ikuenobe, 2006, Base–level buffers and buttresses: A model for upstream versus downstream control on fluvial geometry and architecture within sequences: Journal of Sedimentary Research, v. 76, no. 1, p. 62–174.

Hooke, J. M., 2004, Cutoffs galore!: occurrence and causes of multiple cutoffs on a meandering river: Geomorphology, v. 61, p. 225–238.

Kasse, C., W. Z. Hoek, S. J. P. Bohncke, M. Konert, J. Weijers, M. Cassee, and R. van der Zee, 2005, Late Glacial fluvial response of the Niers–Rhine (western Germany) to climate and vegetation change: Journal of Quaternary Science, v. 20, no.4, p. 377–394.

Kazemeini, S. H., C. Juhlin, K. Zinck-Jørgensen, and B. Norden, 2009, Application of the continuous wavelet transform on seismic data for mapping of channel deposits and gas detection at the CO2SINK site, Ketzin, Germany: Geophysical Prospecting, v. 57, no.1, p. 111–123.

Kessler, F.L., J. Jong, and M. Madon, 2020, The sedimentary record of Paleogene sequences in the Penyu and Malay Basins, offshore peninsular Malaysia: Berita Sedimentology, v. 46, no.1, 6–20.

Kington, J., 2015, Semblance, coherence, and other discontinuity attributes: The Leading Edge, v. 34, no. 12, p. 1510–1512.

Kleinhans, M. G., R. I. Ferguson, S. N. Lane, and R. J. Hardy, 2013, Splitting rivers at their seams: bifurcations and avulsion: Earth Surface Process Landforms, v. 38, no. 1, p. 47–61.

Kolla, V., H. W. Posamentier, and L. J. Wood, 2007, Deep–water and fluvial sinuous channels–characteristics, similarities and dissimilarities, and modes of formation: Marine and Petroleum Geology, v. 24, p. 388–405.

Kornsawan, A., and C. Morley, 2002, The origin and evolution of complex transfer zones (graben shifts) in conjugate fault systems around the Funan Field, Pattani Basin, Gulf of Thailand: Journal of Structural Geology, v. 24, no. 3, p. 435–449.

Lapins, S., D. C. Roman, J. Rougier, S. De Angelis, K. V. Cashman, and J. M. Kendall, 2020, An examination of the continuous wavelet transform for volcano–seismic spectral analysis: Journal of Volcanology and Geothermal Research, v. 389, p. 106728.

Lewis, G. W., and J. Lewin, 1983, Alluvial Cutoffs in Wales and the Borderlands, Modern and Ancient Fluvial Systems, p. 145–154.

Lynds, R., and E. Hajek, 2006, Conceptual model for predicting mudstone dimensions in sandy braided–river reservoirs: AAPG Bulletin, v. 90, no. 8, p. 1273–1288.

Macklin, M. G., and J. Lewin, 2003, River sediments, great floods and centennial scale Holocene climate change: Journal of Quaternary Science, v. 18, no. 2, p. 101–105.

Madon, M., J. Yang, P. Abolins, R. Hassan, A. Yakzan, and S. B. Zainal, 2006, Petroleum systems of the Northern Malay Basin: Geological Society of Malaysia Bulletin, v. 49, p. 125–134.

Mallat, S., 2009, A wavelet tour of signal processing, 3rd edition: Academic Press.

Manshor, N. A., M. H. A. Hassan, and M. Mazlan, 2022, Tidally–influenced fluvial channel systems from the Miocene Malay Basin, Malaysia: Evidence from core facies and seismic geomorphological analyses: Marine and Petroleum Geology, v. 135, p. 1–22.

Mansor, M. Y., A. H. A. Rahman, D. Menier, and M. Pubellier, 2014, Structural evolution of Malay Basin, its link to Sunda Block tectonics: Marine and Petroleum Geology, v. 58, p. 736–748.

Marfurt, K. J., 2006, Robust estimates of reflector dip and azimuth: Geophysics, v. 71, no. 4, p. 29–40.

Marfurt, K. J., R. L. Kirlin, S. L. Farmer, and M. S. Bahorich, 1998, 3-D seismic attributes using a semblance-based coherency algorithm: Geophysics, v. 63, no. 4, p. 1150–1165.

Miall, A. D., 1996, The Geology of Fluvial Deposits: Sedimentary Facies, Basin Analysis, and Petroleum Geology, Springer Berlin, Heidelberg.

Miller, K. G., J. V. Browning, W. J. Schmelz, R. E. Kopp, G. S. Mountain, and J. D. Wright, 2020, Cenozoic sea-level and cryospheric evolution from deep-sea geochemical and continental margin records: Science advances, v. 6, no. 20, p. eaaz1346.

Mitchum, R. M., P. R. Vail, and J. B. Sangree, 1977, Stratigraphic interpretation of seismic reflection patterns in depositional sequences, in C. E. Payton, eds., Seismic Stratigraphy – Applications to Hydrocarbon Exploration, AAPG Memoir 16, p. 117–133.

Morley, C. K., and A. Racey, 2011, Chapter 10 Tertiary Stratigraphy, In M. F. Ridd, A.J. Barber and M. A. Crow, eds., The Geology of Thailand, Geological Society of London Special Publication, p. 224–271.

Morley, C. K., and R. Westaway, 2006, Subsidence in the super-deep Pattani and Malay basins of Southeast Asia: A coupled model incorporating lower-crustal flow in response to post-rift sediment loading: Basin Research, v. 18, no. 1, p. 51–84.

Morley, C. K., P. Charusiri, and I. M. Watkinson, 2011, Structural geology of Thailand during the Cenozoic, in M.F. Ridd, A. J. Barber, and M. J. Crow eds., The Geology of Thailand, p. 273–354.

Partyka, G., J. Gridley, and J. Lopez, 1999, Interpretational applications of spectral decomposition in reservoir characterization: The Leading Edge, v. 18, no. 3, p. 353–360.

Phillips, J. D., 2013, Hydrological connectivity of abandoned channel water bodies on a coastal plain river: River Research and Applications, 29, no.2, p. 149–160.

Posamentier, H. W., 2001, Lowstand alluvial bypass systems: Incised vs. unincised: AAPG Bulletin, v. 85, no. 10, p. 1771–1793.

Posamentier, H. W., M. T. Jervey, and P. R. Vail, 1988, Eustatic controls on clastic deposition I – Conceptual framework. In C. K. Wilgus, B. S. Hastings, C. G. S. C. Kendall, H. W. Posamentier, C. A. Ross, and J. C. Van Wagoner, eds., Sea-Level changes – an integrated approach, SEPM Special Publication, v. 42, p. 109–124.

Posamentier, H. W., R. J. Davies, J. A. Cartwright, and L. J. Wood, 2007, Seismic geomorphology: An overview. In R. J. Davies, H. W. Posamentier, L. J. Wood, and J. A. Cartwright, eds., Seismic geomorphology: Applications to hydrocarbon exploration and production, Geological Society of London Special Publication, no. 277, p. 1–14.

Posamentier, H. W., V. Paumard, and S. C. Lang, 2022, Principles of seismic stratigraphy and seismic geomorphology I: Extracting geologic insights from seismic data: Earth-Science Reviews, v. 228, p. 103963.

Pubellier, M., and C. Morley, 2014, The basins of Sundaland (SE Asia): Evolution and boundary conditions: Marine and Petroleum Geology, v.58, p. 555–578.

Reijenstein, H. M., H. W. Posamentier, and J. P. Bhattacharya, 2011, Seismic geomorphology and high-resolution seismic stratigraphy of inner-shelf fluvial, estuarine, deltaic, and marine sequences, Gulf of Thailand: AAPG Bulletin, v. 95, no. 1, p. 959–1990.

Rhoads, B. L., 2020, River Dynamics, Geomorphology to Support Management, Cambridge University Press.

Russell, B., and J. Han, 2016, Jean Morlet and the continuous wavelet transform. CREWES Res. Rep, v. 28, p. 115.

Searle, M. P., and C. K. Morley, 2011, Tectonic and thermal evolution of Thailand in the regional context of SE Asia, in M. F. Ridd, A. J. Barber, and M. J. Crow, eds., The Geology of Thailand, p. 539–572.

Shields D. F., and S. R. Abt, 1989, Sediment deposition in cutoff meander bends and implications for effective management: Regulated Rivers: Research & Management, v. 4, no. 4, p. 381–396.

Simon, S. S. T., and M. R. Gibling, 2017, Fine-grained meandering systems of the Lower Permian Clear Fork Formation of north-central Texas, USA: Lateral and oblique accretion on an arid plain: Sedimentology, v. 64, no. 3, p. 714–746.

Sinha, S, P. S. Routh, P. D. Anno, and J. P. Castagna, 2005, Spectral decomposition of seismic data with continuous-wavelet transform: Geophysics, v.70, no. 6, p. 19–25.

Snedden, J. W., 2013, Channel-body basal scours: Observations from 3D seismic and importance for subsurface reservoir connectivity: Marine and Petroleum Geology, v. 39, no. 1, p. 150–163.

Speed, C. M., J. M. Swartz, S. P. S. Gulick, and J. A. Goff, 2023, Seismic expression and stratigraphic preservation of a coastal plain fluvial channel belt and floodplain channels on the Gulf of Mexico inner continental shelf: Sedimentology, v. 70, no. 2, p. 451–474.

Toonen, W. H., M. G. Kleinhans, and K. M. Cohen, 2012, Sedimentary architecture of abandoned channel fills: Earth Surface Processes and Landforms, v. 37, no. 4, p. 459–472.

Vail, P. R. 1987, Seismic stratigraphy interpretation using sequence stratigraphy: Part 1: Seismic stratigraphy interpretation procedure, in A.W. Bally eds., Atlas of seismic stratigraphy, AAPG Study in Geology, no. 27, p. 1–10.

Walker, R. G., and D. J. Cant, 1984, Sandy Fluvial Systems, in R.G. Walker eds., Facies models, Geoscience Canada, p. 71–87.

Winkels T. G., E. Stouthamer, and K. M. Cohen, 2022, Planform architecture, meander evolution and grain-size variability of a deltaic channel belt in the Rhine-Meuse delta, The Netherlands: Sedimentology, v. 69, no. 7, p. 2844–2866.

Wood, L. J. and K. L. Mize-Spansky, 2009, Quantitative seismic geomorphology of a Quaternary leveed-channel system, offshore eastern Trinidad and Tobago, northeastern South America: AAPG Bulletin, v. 93, no. 1, p. 101–125.

Wood, L. J., 2007, Quantitative seismic geomorphology of Pliocene and Miocene fluvial systems in the northern Gulf of Mexico, USA: Journal of Sedimentary Research, v. 77, no. 9, p. 713–730.

Wu, X., 2017, Directional structure-tensor-based coherence to detect seismic faults and channels: Geophysics, v. 82, no.2, p. A13–A17.

Wu, X., and Z. Guo, 2018, Detecting faults and channels while enhancing seismic structural and stratigraphic features: Interpretation, v. 7, no.1, p. T155–T166.

Yakzan, A. M., A. Harun, and R. Morley,1996, Integrated biostratigraphic zonation for the Malay Basin: Bulletin of the Geological Society of Malaysia, v.78, no.7, p. 1170–1171.

Zeng, H. L, 2010, Stratal slicing: Benefits and challenges: The Leading Edge, v. 29, no. 9, p. 1040–1047.

Zeng, H. L, M. M. Backus, K. T. Barrow, and, N. Tyler, 1998, Stratal slicing, part I: realistic 3-D seismic model: Geophysics, v. 63, no. 2, p. 502–513.

Zeng, H. L, R. G. Loucks, and L. F. Brown Jr, 2007, Mapping sediment-dispersal patterns and associated systems tracts in fourth-and fifth-order sequences using seismic sedimentology: Example from Corpus Christi Bay, Texas: AAPG Bulletin, v. 91, no. 7, p. 981–1003.

Chapter 3: Quantitative Lithology Prediction of Turbidite Deposits, Bone Spring Formation, Delaware Basin, Southeast New Mexico And West Texas

*This chapter was presented by invitation at the IMAGE 2021 and 2024 Annual Convention and Exhibition.

Zhai. R., and J. D. Pigott, 2021, High-resolution sequence stratigraphy and multiple attributes analysis of the Bone Spring turbidite system, northern Delaware Basin: IMAGE 2021 Annual Convention and Exhibition.

Zhai. R., and M. J. Pranter, 2024, Multidimensional data-driven characterization of deepwater turbidite deposits, Leonardian Bone Spring Formation, Delaware Basin, Southeast New Mexico and West Texas: IMAGE 2024 Annual Convention and Exhibition.

ABSTRACT

The Bone Spring Formation of the Delaware Basin in southeast New Mexico and west Texas consists of approximately 1,500 m (4,921 ft) mixed siliciclastic-carbonate deep-water turbidite systems deposited on carbonate slope and basin floor settings. Despite its substantial hydrocarbon potential, reservoir heterogeneity hinders efficient development. This study focuses on the Second Bone Spring Sandstone (2BSSS) Member, integrating 3-D seismic data, well logs from 60 wells, and core data to assess lithologic architecture and reservoir quality. High-frequency sequence stratigraphy analysis reveals that the 2BSSS Member can be subdivided into three high-frequency stratigraphic units, they reflect basinward-thickening trends shaped by relative sea-level fluctuations and turbidite sedimentation. Petrological analysis identifies four main lithologies: siltstone, dolomite-cemented siltstone, limestone, and mudstone. Turbidite deposits show significant vertical and lateral lithologic heterogeneity, with siltstone-rich intervals occurring in 2BSSS-1 and 2BSSS-3. Lithology classification was performed using RHOmaa–Umaa crossplots calibrated with core data, and predictions were extended basin-wide using a multilayer perceptron (MLP) model trained on conventional well logs. The MLP model achieved high classification accuracy, with limestone and siltstone showing the best performance. Although the 2BSSS is considered sand-rich, limestone remains the most abundant lithology (45%), followed by siltstone (30.5%) and dolomite-cemented siltstone (20.9%). Mudstone contributes only 3.6%. Bayesian lithology inversion, combining elastic seismic attributes with lithology priors, enables the prediction of spatial lithologic distribution. Inversion results reveal elongate siliciclastic belts aligned with depositional trends and complex heterogeneity across the 2BSSS units. Reservoir quality is primarily controlled

by lithology. Siltstone exhibits the highest porosity (average 8%) and permeability (average 0.05 mD), whereas dolomite-cemented siltstone and limestone have significantly reduced reservoir properties due to diagenetic modification. The study highlights the influence of stratigraphic cyclicity and lithologic variation on reservoir heterogeneity in a deep-water mixed siliciclastic-carbonate turbidite system.

3.1 INTRODUCTION

The Bone Spring Formation of lower Leonardian Series in the Permian Basin, located in West Texas and southeastern New Mexico, has attracted significant attention for its deep-water turbidite systems for its vast hydrocarbon reserves (Montgomery, 1997a). The formation comprises alternating carbonate debris flows, shales, and fine-grained siliciclastic turbidites, deposited on slope and basin-floor environments through gravity-driven flows (Montgomery,1997b; Kerans and Ruppel, 2020). Consequently, the reservoir exhibits complex stratigraphy, diverse lithology, and intricate internal depositional architecture. Studies demonstrate that sea-level fluctuations strongly impacted sediment routing from shelf margins to basin floor, resulting in layered turbidite sequences (Gardner and Borer, 2000; Nance and Rowe, 2015). Sediment gravity flows carried sediments deep into the basin (Hodson and Alexander, 2010; Hud et al. 2018). Some works (Asmus and Grammer, 2013; Minisini and Desjardins, 2024) attribute the repetitive stratigraphic cycles of Bone Spring Formation to climatic and tectonic controls, shaping reservoir heterogeneity. Petrophysical analyses (Barker,1986; Mazzullo and Reid, 1987; Montgomery,1997b) further emphasize the reservoir heterogeneity is significantly influenced by diagenesis, with carbonate cements occluding primary porosity, while others preserve matrix porosity within fine-grained sandstones. These contrasting lithologies exhibit variable porosity and permeability further complicate lateral continuity and reservoir compartmentalization. Although these reservoirs contain the largest proven oil reserves among tight oil plays and possess substantial undiscovered recoverable resources in the Permian Basin, their significant heterogeneity severely limits efficient development.

Research on deep-water turbidites in the Permian Basin's mixed siliciclastic–carbonate systems has advanced significantly over the past two decades, revealing complex sedimentary patterns and lithologies shaped by depositional dynamics and environmental factors. Sedimentary patterns in mixed systems often alternate between classic Bouma-type siliciclastic turbidites and carbonate-dominated units (Bouma, 1996; Moscardelli et al., 2019). Recent sedimentological studies (Schlager et al., 1994; Playton and Kerans, 2018) emphasize turbidite systems' lateral and vertical heterogeneity attributed to topographic confinement, fluctuating sediment supply, and multistage depositional events. In mixed systems, sediment dispersal is driven by episodic carbonate platform shedding and terrigenous influxes (Rankey & Doolittle, 2012; Reijmer et al., 2015). Deposits exhibiting cohesive debris flows and turbulent flows are interpreted as the results of linked debrite–turbidite systems or hybrid event beds (Talling, 2013; Hurd et al., 2016). In such scenarios, the lithology of mixed clastic–carbonate turbidites ranges from coarse-grained carbonate breccias to laminated calcareous silts and quartz-rich sandstones. Mixed beds appear as interbedded sequences with sharp vertical transitions, hybrid sedimentary structures, and amalgamation surfaces, reflecting rapid depositional pulses and shifts in the source material (Drzewiecki and Simó, 2002; Chiarella et al., 2012, 2017; Kvale et al., 2020). Thus, gravity flows simultaneously entrain diverse sediment types during downslope transport, producing heterogeneous deposits characterized by complex internal textures and transitional lithologies, which add significant complexity to lithological classification. This lithological complexity poses challenges for classification and highlights the importance of understanding sedimentary architecture in hydrocarbon exploration and reservoir characterization.

Advances in sedimentological studies and reservoir analysis have identified many exploration prospects within the Bone Spring Formation's mixed siliciclastic–carbonate turbidite reservoirs. However, geological uncertainty persists due to reservoir heterogeneity, hindering the effective delineation of productive zones. This study focuses on the Bone Spring reservoir in the northwestern Delaware Basin. It integrates sequence stratigraphy, seismic interpretation, and well data-based lithology analysis to unravel the turbidite reservoir's internal architecture and lithological variability. The objectives of this study are to answer the following questions: (1) what are the characteristics of seismic stratigraphy and high-frequency sequence stratigraphy based on seismic and well data? (2) what is the stratigraphic variability of lithologies? Moreover, (3) what is the spatial variability of lithologies determined by seismic inversion and Bayesian lithology inversion? This study contributes significantly to identifying and characterizing thin-bedded, mixed turbidite reservoirs, with particular emphasis on stacking patterns and lithological heterogeneity. This study enhances the reliability of lithological classification in mixed siliciclastic carbonate systems by integrating log-based multilayer perceptron lithology prediction with seismic-based Bayesian lithology inversion. These integrated methods substantially advance the geological understanding of the Second Bone Spring Sandstone Member and offer practical implications for exploration and development. These integrated methods substantially advance the geological understanding of the Second Bone Spring Sandstone Member and offer practical implications for exploration and development. Specifically, it refines multi-data-driven reservoir characterization workflows and supports identifying exploration targets in geologically analogous settings across the broader Permian Basin.

This study aims to analyze reservoir heterogeneity across multiple scales using seismic and well-log data, with the goal of predicting and mapping reservoir quality and identifying potential target zones. The study integrates 530 km^2 (205 mi^2) of 3-D seismic data, borehole logs from 40 wells, and core data from one well to evaluate high-frequency sequence stratigraphy, lithology distribution, and reservoir characteristics. High-frequency analysis of the Second Bone Spring Sandstone member is conducted by correlating seismic and well-log data to interpret the effects of relative sea-level fluctuations on vertical stacking patterns and lateral turbidite distribution. Subsequently, within the stratigraphic framework, lithology identification and characterization of reservoir heterogeneity are carried out using RHOmaa–Umaa crossplot analysis and artificial neural network prediction. Finally, lithological distribution across the study area is predicted by Bayesian lithologic inversion.

3.2 GEOLOGIC SETTING

The Bone Spring Formation is one of the significant thick stratigraphic units in the Permian Basin, formed in response to Late Paleozoic tectonic activity (Ruppel, 2019; Ewing, 2019; Ewing et al., 2019). Tectonically, the Permian Basin is a component of the multistage Paleozoic West Texas Basin complex. From the late Mississippian to early Permian, the Ancestral Rocky Mountains (ARM) and the Ouachita-Marathon orogeny caused basement uplifts, faulting, and subsidence, creating the greater Permian Basin overlying the Tobosa Basin (Schumaker, 1992; Adams and Keller,1996; Fairhurst et al., 2021). The uplifted and eroded high-standing area in the central basin divided the Permian Basin into the deep Delaware Basin to the west, the shallower Midland Basin to the east, and the Val Verde Basin to the south (Figure 3.1). Basin subsidence was synchronous with deformation during this period; subsidence was most rapid during the early Permian, then continued at a lower, steady rate until the end of the Permian. Nearly 2,400 m (8,000 ft) of Permian strata were deposited over basins and uplifts. In the Mesozoic and Cenozoic, uplift and erosion reshaped the basin margins with little effect on its central part. During the early and middle Mesozoic, uplift and tilting affected the margins of the eastern, southern, and southwestern of the basin (Brown, 2019). A transgression from the late Early to late Cretaceous covered the entire area. From the Late Cretaceous to the Eocene, the Laramide Orogeny induced compression and transpression along the southern and western margins of the Permian Basin, reactivating Paleozoic and Precambrian structures and uplifting these margins. Starting in the Oligocene, uplift, and extension supplanted earlier compressional stresses. The Delaware Basin was uplifted and tilted eastward, forming the Guadalupe Mountains and Delaware Mountains on the western flank of the basin.

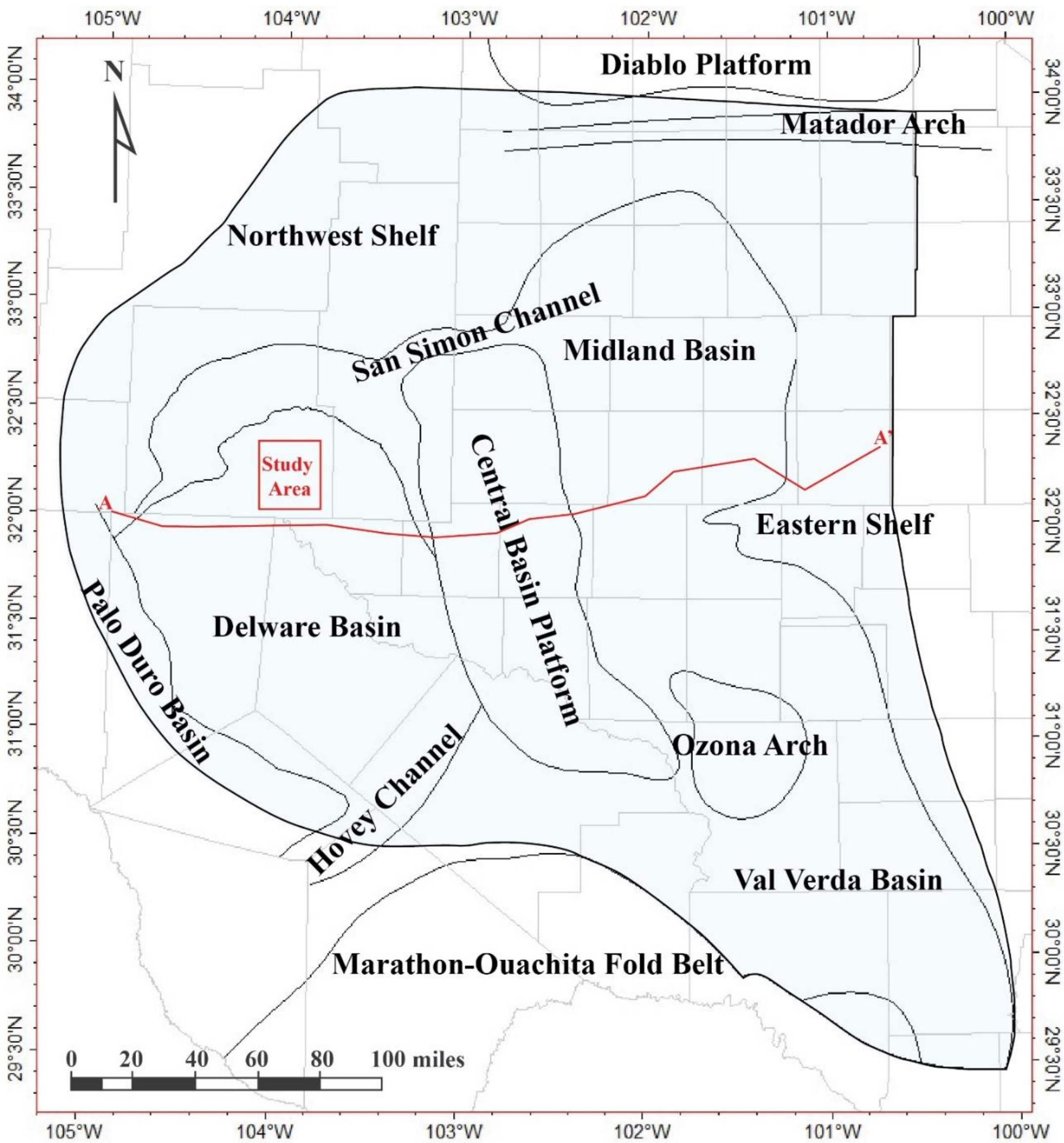

Figure 3.1: Location map of the study area in the Permian Basin and paleogeographic setting during the Late Permian (modified from Ruppel, 2019).

Delaware Basin subsidence occurred during the Early Permian (Kerans and Kempter, 2002; Hamlin and Baumgardner, 2020; Nance and Hamlin, 2020). The Wolfcampian and Leonardian series constitute the primary stratigraphy of the Delaware Basin (Figure 3.2). The Bone Spring Formation of the Leonardian Series comprises more than 1,060 m (3,480 ft) of alternating carbonate and siliciclastic successions on the slope and basin floor. Uplift of the basin margin and Central Basin Platform during the Early Permian contributed to the growth of reefs and the buildup of carbonate shelf margins on the edges of the Delaware Basin. At the same time, the basin subsidence rate exceeded the depositional rate, forming a deepwater basin with structurally steep ramp margins and platforms. The Early Permian Period was a global warming phase, transitioning from Late Carboniferous icehouse conditions to a Mesozoic greenhouse climate, with sea-level fluctuations reaching up to 70 m (230 ft) during the Leonardian. Sea-level fluctuations transported carbonate detritus from shallow-water carbonate and siliciclastic sources into the basin through debris and turbidite flows. The cyclic stratigraphic pattern divides the Bone Spring Formation into multiple lithostratigraphic members. The thickness of each member varies between 30 m to 300 m (100 ft to 1,000 ft).

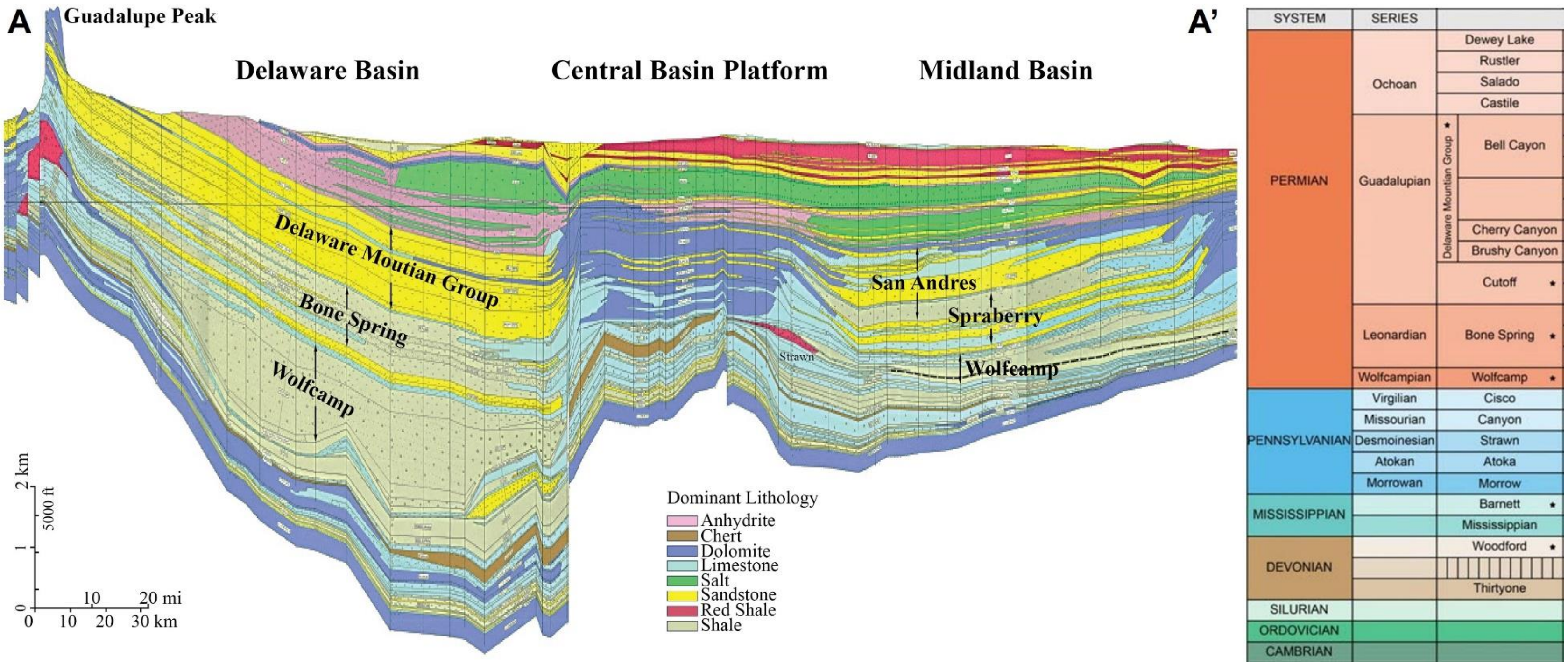

Figure 3.2: Stratigraphic section and chart of the Permian Basin (modified from Ewing, 2019).

3.3 METHODS

This study employs an integrated lithology identification and prediction workflow using multiple datasets. First, the RHOmaa–Umaa crossplot method is applied to 34 wells with photoelectric-effect (PE) logs to classify lithologies. Subsequently, a multilayer perceptron (MLP) neural network is trained using these classifications to predict lithology in the remaining six wells lacking PE logs. Finally, seismic Bayesian lithology inversion is conducted by integrating the well-based lithology classifications with acoustic impedance inversion results from all 40 wells, enabling spatial prediction of reservoir lithologies.

3.3.1 RHOmaa-Umaa Crossplot Analysis

The collaboration of different porosity logs, such as density (RHOB), neutron (NPHI), photoelectric-effect (PE), and sonic logs (DT), along with their crossplots serves as a key method for lithology estimation. This study uses the matrix identification plot method for lithology identification (Asquith and Krygowski, 2004a, 2004b; Pranter et al., 2004). This method relies on two physical properties: the apparent matrix density and the apparent volumetric cross-section. Lithologies are identified by determining these apparent matrix parameters within a crossplot framework. The parameter RHOmaa (or written as ρ_{maa}) represents the estimated density of the solid framework of the rock measured in the formation, and Umaa (or written as U_{maa}) denotes the bulk photoelectric absorption of the rock derived from the logs. Because these values are primarily influenced by mineralogical composition and emphasize matrix values rather than porosity, they are effective for distinguishing different lithologies. Their calculations are described in Appendix A. This study uses three mineralogical compositions, quartz, calcite, and dolomite, to construct a mineralogical triangle. Lithology can be accurately identified by plotting the calculated RHOmaa and Umaa values on this mineralogy triangle with percentage contours.

3.3.2 Multilayer Perceptron (MLP)

This study employs the multilayer perceptron (MLP) model on well-log data for lithology prediction (Schmidhuber, 2015; Golovkoa, 2017). The MLP is a type of deep learning model that is the foundation for more complex architectures, such as convolutional and recurrent neural networks (Delashmit and Manry, 2005; Sarker, 2021). The MLP comprises multiple layers of neurons and includes three main components: the input layer, hidden layer, and output layer. Each neuron in a layer connects to every neuron in the subsequent layer, forming a fully connected network. Each neuron in a layer is connected to every neuron in the next layer, making it a fully connected network. The MLP processes data through forwarding and backpropagation. In forward propagation, input values pass through layers where neurons compute weighted sums, add biases, and apply activation functions to introduce non-linearity. The final output layer generates predictions. Backpropagation then evaluates prediction error using a loss function and adjusts weights and biases iteratively until optimal performance is achieved. Backpropagation calculates the prediction error using a loss function and propagates it backward to update weights and biases through gradient descent. This iterative process continues until model performance is optimized.

The following steps were developed to apply the MLP model for lithology prediction. Step 1: Data preparation. This step involves selecting and preprocessing the data. The dataset is built using selected log features and lithologic classifications defined in the lithologic analysis. To avoid overfitting, only one log is used per logging type. Since

MLP is sensitive to feature scales, normalization is applied to get training efficiency and model stability. Step 2: Dataset design for classifier training. The dataset is split into training, validation, and testing subsets. Training data from 34 wells, labeled via RHOmaa–Umaa analysis, is used to train the model. Core data from one well supports validation, while six wells without PE logs form the testing set for prediction. Step 3: Hyperparameter tuning. The MLP's performance depends on optimizing architectural and training parameters, including the number of neurons and hidden layers. The hyperparameter setting is described in Appendix B. Step 4: Performance assessment. Model performance is evaluated using Accuracy, Precision, Recall, and F1-score. These metrics quantify prediction correctness, relevance, completeness, and overall balance. Definitions and formulas are provided in Appendix B.

3.3.3 Bayesian Inversion

Building on lithology identification, Bayesian lithology inversion is applied to estimate the spatial distribution of lithologies based on the probability of a given lithology occurring at a specific seismic impedance value (Lambert, 2018). This probabilistic method, grounded in Bayes' theorem, integrates prior geological knowledge with seismic observations to compute posterior lithology probabilities (Larsen et al., 2006; Sayers et al., 2019; Kolbjørnsen et al., 2020). This method enables lithology prediction from seismic response by updating prior distributions with new seismic data. Refer to Appendix C for detailed calculations.

This study implements Bayesian lithology inversion in four steps: (1) Seismic Inversion: Compute P-impedance and S-impedance volumes using model-based inversion methods. (2) Probability modeling: Construct the full probability model, a joint probability distribution for all lithologies. The prior probability $P(B_i)$ for each lithologic type is derived from lithologic proportions using RHOmaa-Umaa analysis and MLP prediction. The conditional probability $P(A|B_i)$ calculates the probability that a specific seismic inversion value corresponds to each type of lithology. The full probability $P(A)$ is obtained by summing the products of conditional probabilities $P(A|B_i)$ and prior probability $P(B_i)$ across all lithologies. (3) Posterior evaluation: Use kernel density estimation (KDE) to condition well and seismic data by lithology and train the conditional probability distribution of seismic attributes. (4) Posterior evaluation: To validate the inversion results, assess posterior distributions using confusion matrices at well locations. This Bayesian inversion framework integrates seismic attributes with prior geological knowledge to enable lithology prediction from seismic data.

3.4 RESULTS AND INTERPRETATIONS

3.4.1 High-Frequence Sequence Stratigraphy

(1) Stratigraphic Cyclicity of The Bone Spring Fromation

In the study area, stratigraphic boundaries within the Bone Spring Formation are identified based on seismic unconformities and abrupt lithologic contacts. The seismic profile (Figure 3.3) shows that the Bone Spring Formation downlap a prominent angular unconformity, which truncates the underlying Wolfcamp Formation. The top of the Bone Spring Formation is marked by high-angle, continuous downlap reflections from the overlying Cutoff Formation. Because the study area is located along the lower slope and basin floor, stratigraphic surfaces such as unconformity, maximum flooding surface, and maximum regressive surface are not clearly expressed by typical seismic reflection terminations such as onlap, downlap, or toplap. These stratigraphic surfaces were delineated by integrating well-log characteristics with correlated seismic reflections. Figure 3.4 illustrates that gamma-ray logs identify the erosional bases of siliciclastic intervals, characterized by high gamma-ray values, and the sharp contacts with overlying carbonate intervals, marked by low gamma-ray values. These abrupt changes are interpreted as submarine equivalents of subaerial unconformities and maximum flooding surfaces, which appear as continuous and intense reflections in seismic profiles. As a result, seven distinct stratigraphic surfaces were identified within the Bone Spring Formation.

The identified stratigraphic surfaces define the stratigraphic hierarchy and divide the Bone Spring Formation into three fourth-order sequences. Within each fourth-order sequence, complete systems tracts are rarely developed in the study area. Instead, the falling-stage systems tract (FSST) and lowstand systems tract (LST) produce siliciclastic

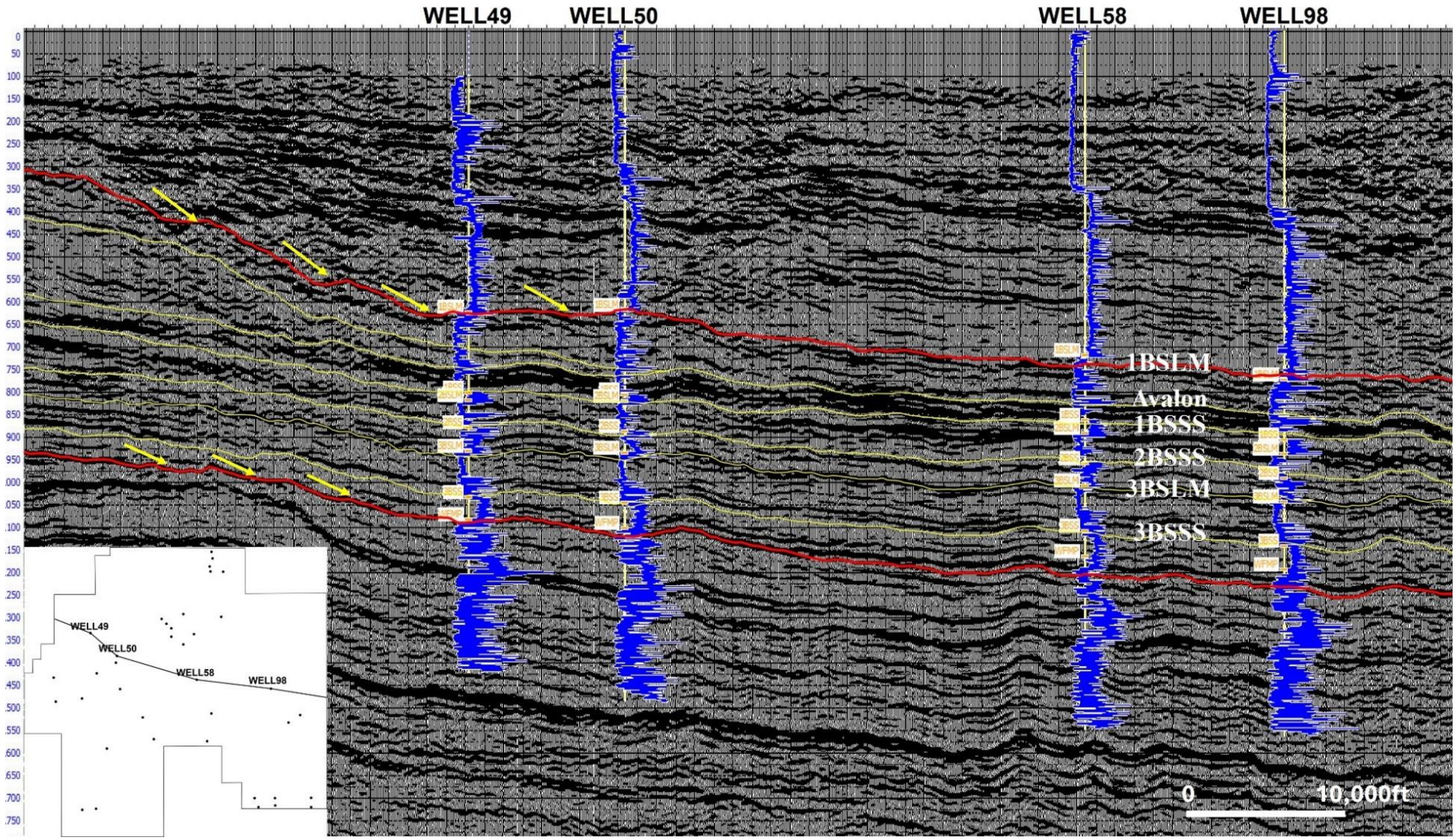

Figure 3.3: Seismic sequence stratigraphy interpretation of the Bone Spring Formation in the study area. Seven stratigraphic surfaces are traced across the study area, including the top and base of Bone Spring, the tops of 3BSSS, 3BSLM, 2BSSS, 1BSSS, and Ava.

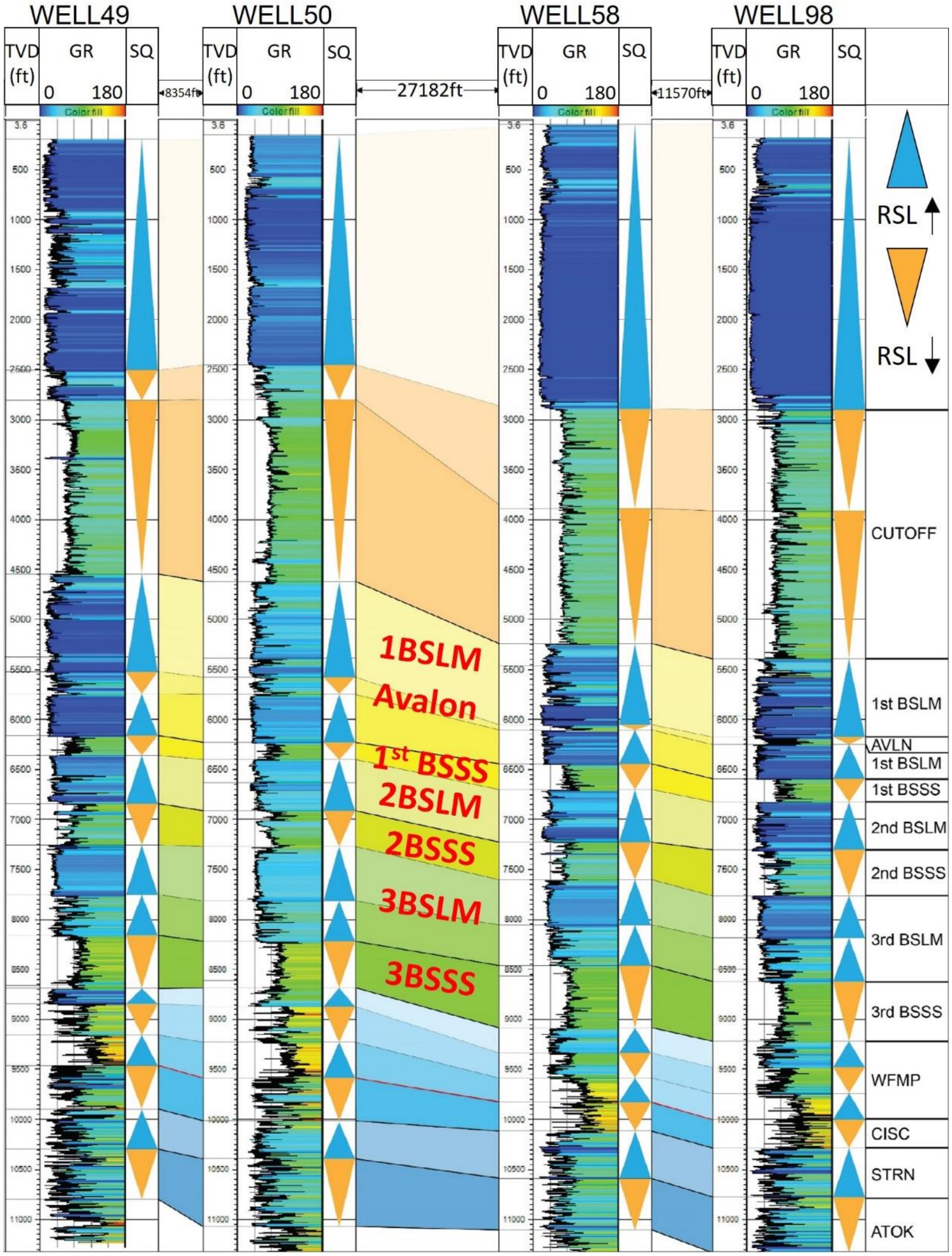

Figure 3.4: Well cross-section shows the high-frequency sequence stratigraphy interpretation of the Bone Spring Formation. Wells are correlated to the seismic in Figure 3.3.

intervals during the relative sea-level regression and lowstand. In contrast, the transgressive systems tract (TST) and highstand systems tract (HST) are responsible for accumulating limestone intervals during the relative sea-level rise. As a result, these sequences are subdivided into seven lithostratigraphic members. Following regional stratigraphic nomenclature, these members from bottom to top are named the Third Bone Spring Sandstone (3BSSS), Third Bone Spring Limestone (3BSLM), Second Bone Spring Sandstone (2BSSS), Second Bone Spring Limestone (2BSLM), First Bone Spring Sandstone (1BSSS), Avalon Sandstone (AVLN), and First Bone Spring Limestone (1BSLM). Well cross-sections show that each siliciclastic Member is characterized by basinward thickening, indicating a progradational stacking pattern. The four siliciclastic members vertically exhibit a general thinning-upward trend, whereas the carbonate members progressively increase in thickness. This pattern reflects the gradual reduction of turbidite input into the basin during relative sea level rise. As a result, the Bone Spring Formation exhibits an overall deepening upward stratigraphic trend.

(2) Stratigraphic architecture of the Second Bone Spring Member

This study focuses on the 2BSSS Member to interpret the turbidite depositional characteristics in the study area. Well cross-section (Figure 3.5) reveals that the 2BSSS Member consists of alternating siliciclastic and carbonate intervals. Multistory thick siliciclastic deposits were stacked on a sharp base, while the top typically displays a gradual fining upward trend, indicating either decreasing energy conditions or reduced sediment supply. Based on the vertical stacking pattern, three high-frequency stratigraphic cycles were identified within the 2BSSS member, named from bottom to top as Units: 2BSSS-3, 2BSSS-2, and 2BSSS-1. 2BSSS-1 and 2BSSS-3 contain more abundant siliciclastic

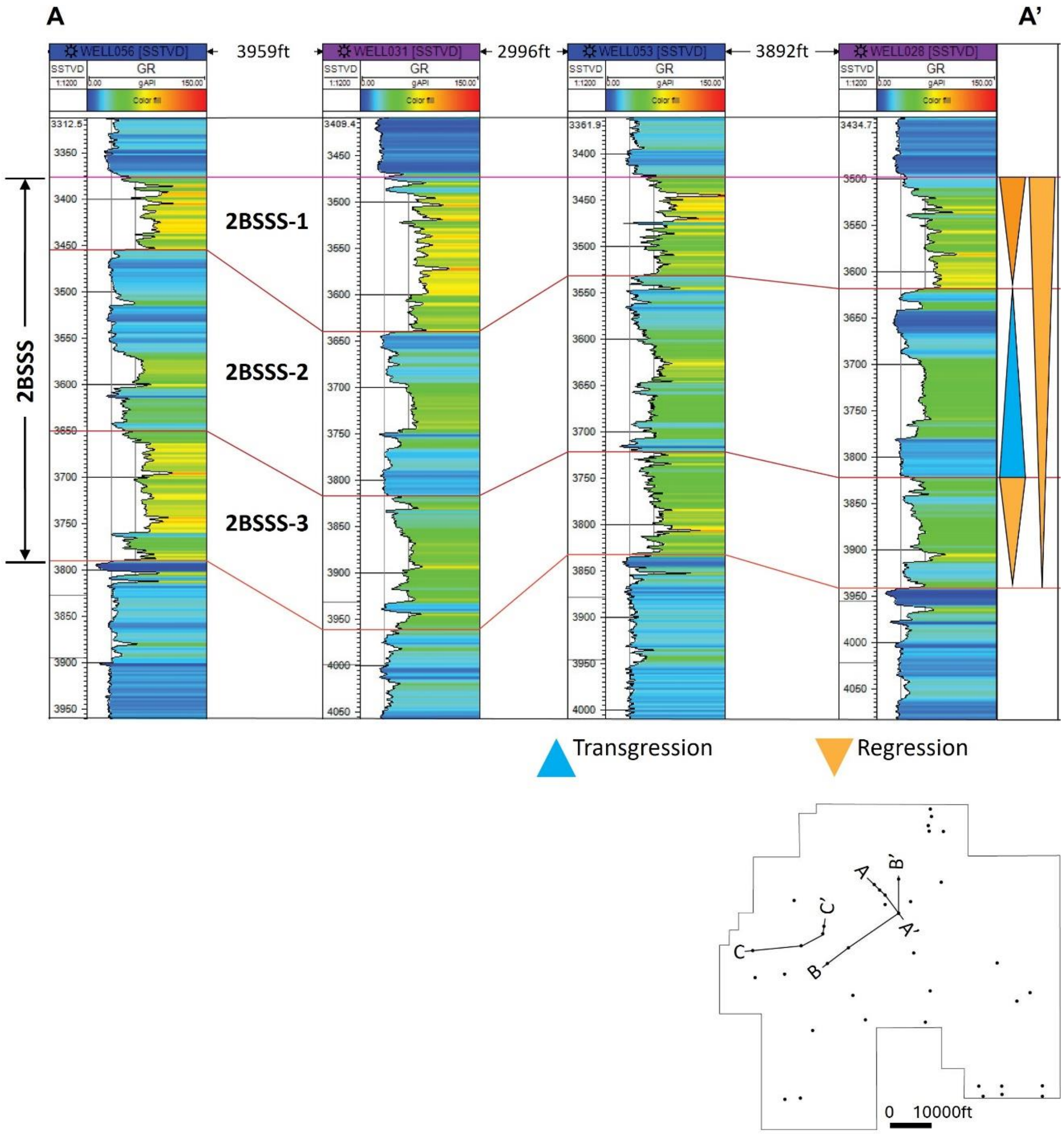

Figure 3.5: Well, the cross-section shows the stratigraphic cyclicity of 2BSSS members. The 2BSSS member contains three high-frequency stratigraphic units: 2BSSS-1, 2BSSS-2, and 2BSSS-3.

deposits, while a higher proportion of limestone distinguishes 2BSSS-2. All three stratigraphic units exhibit a progradational stacking pattern, as indicated by their thickness variations (Figure 3.6). The average thickness of the 2BSSS is approximately 120 m (394 ft), with 2BSSS-3 averaging 50 m (164 ft), 2BSSS-2 and 2BSSS-1 each averaging approximately 30 m (98 ft). Despite local variation, all units exhibit a trend of increasing thickness basinward, reflecting vertical progradation toward the basin. Significant lateral thickness variations are attributed to topographic relief and depositional dynamics. These variations are interpreted as a response to high-frequency relative sea-level fluctuations. Constructive interference during these fluctuations enhanced siliciclastic sediment supply at specific locations, resulting in marked lateral thickness changes.

On the lower slope, thick stacked siliciclastic deposits in Units 2BSSS-1 and 2BSSS-3 exhibit pronounced cyclicity (Figure 3.7). Individual cycles range from 2 m to 10 m (7 ft to 33 ft) in thickness and are generally only correlatable over short distances. Alternating low and high siliciclastic layers are interpreted as products of episodic turbidite deposition. These stacking patterns reflect the accumulation of multiple, discrete turbidite events. During relative sea-level lowstands or stillstands, pulses of high-energy turbidity currents likely triggered variations in sediment supply, explaining the observed variations in siliciclastic content within each unit. These findings demonstrate that, although the 2BSSS Member shows a general progradational stacking pattern, its internal architecture is far more complex at finer stratigraphic scales, reflecting significant heterogeneity in turbidite distribution.

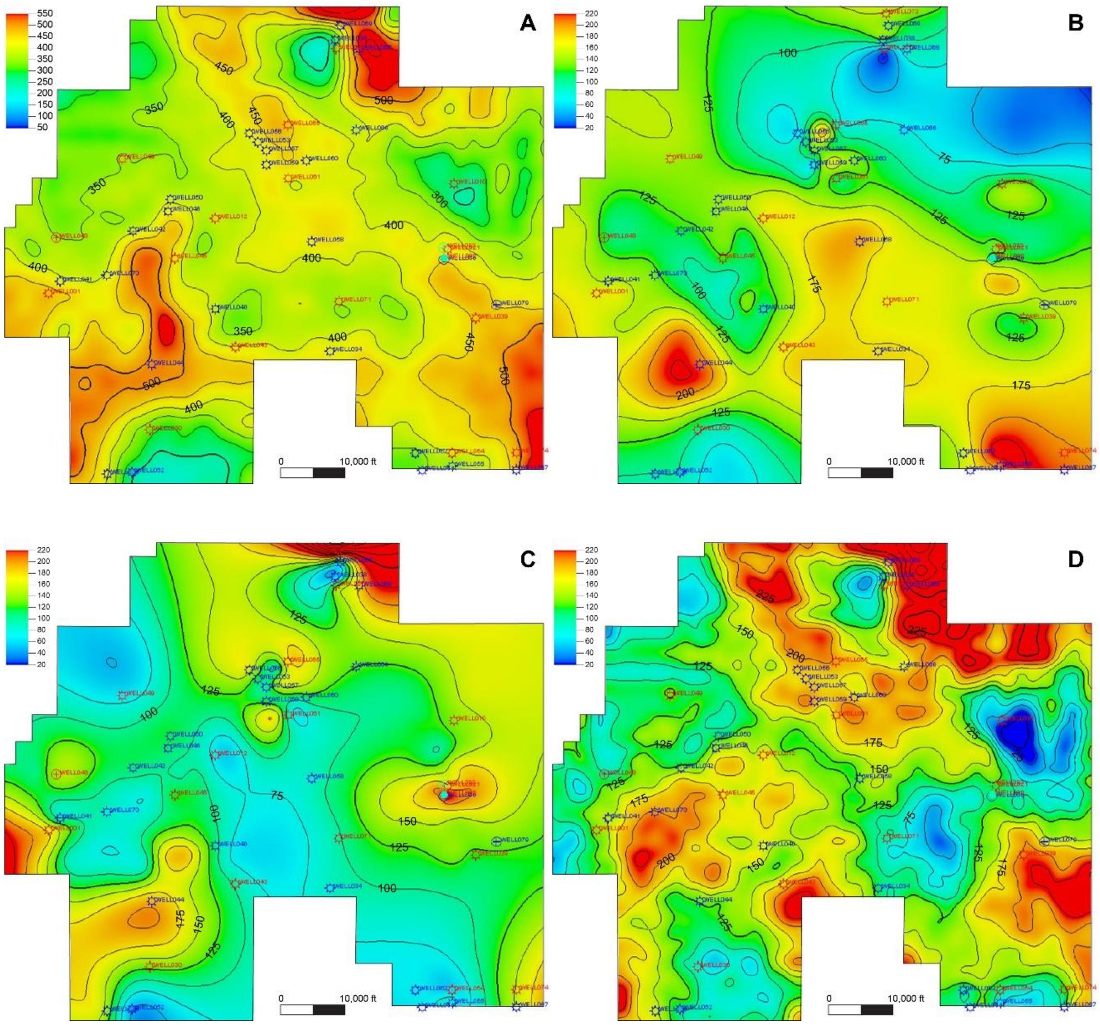

Figure 3.6: (A) The isopach map of the 2BSSS; (B) The isopach map of the 2BSSS-1; (C) The isopach map of the 2BSSS-2; and (D) The isopach map of the 2BSSS-3. The thickness of individual stratigraphic units generally increases basinward.

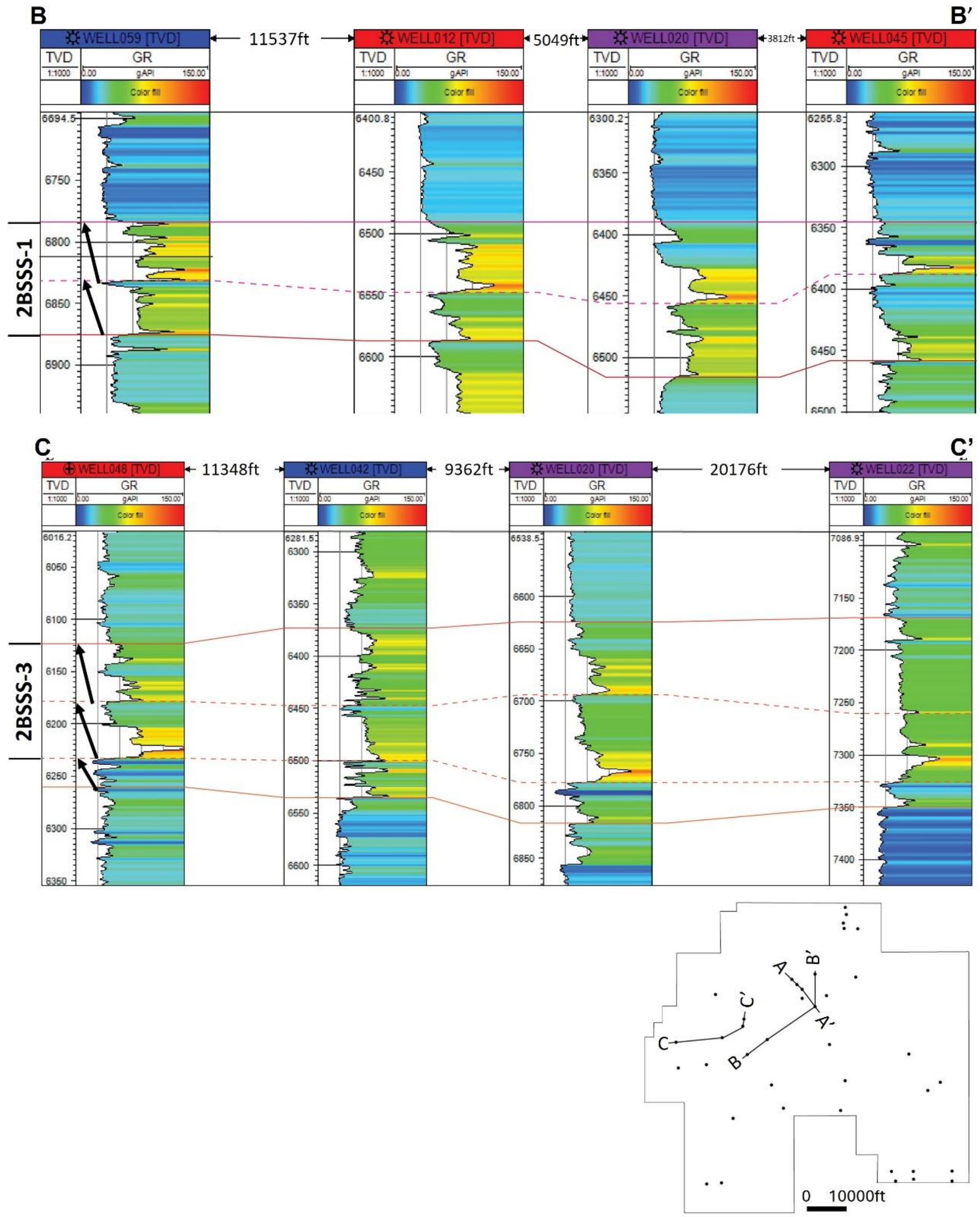

Figure 3.7: The well cross-section shows the depositional cyclicity of the 2BSSS-1 and 2BSSS-3 Units. The 2BSSS-1 unit contains two stacking cycles, and the 2BSSS-3 unit contains three stacking cycles.

3.4.2 Rhomaa–Umaa Crossplots Lithology Identification

This study adopts the lithology classification scheme of four lithologies previously defined through petrological analysis, including siltstone, dolomite-cemented siltstone, limestone, and mudstone. (1) Siltstone: Siltstone is extensively developed in basin-floor deposits of all four sandstone members of the Bone Spring Group, forming major hydrocarbon reservoirs. In the 2BSSS, siltstone has intermediate gamma-ray values (API > 60), low bulk densities (RHOB < 2.5 g/cm^3), high sonic values (DT > 65 μs/ft), and high neutron porosity (NPHI > 0.10). (2) Dolomite-cemented siltstone: dolomitization is a primary diagenetic process in the Bone Spring Group, resulting in widespread dolomite-cemented siltstone within the 2BSSS. Dolomite cementation significantly impacts reservoir quality. Dolomite-cemented siltstone shows well-log responses similar to siltstone but has slightly lower neutron porosity (NPHI < 0.08). (3) Limestone: Limestone primarily comprises dense lime mudstone with some wackestone, formed as calciturbidites and related sediment-density flow deposits. Compared to siliciclastic deposits, limestone exhibits low gamma-ray responses (API < 35), high bulk densities (RHOB > 2.5 g/cm^3), high sonic values (DT < 60 μs/ft), and low neutron porosity (NPHI < 0.06). (4) Mudstone: Mudstone in the Bone Spring Formation comprises fine-grained silt, clay minerals, fine-grained carbonates, and organic matter. Mudstone typically forms millimeter- to centimeter-scale interbeds with siltstone. It is characterized by very high gamma-ray responses (API > 90).

To estimate the proportion of lithology within the 2BSSS Member, the RHOmaa–Umaa crossplots were first calibrated with core data. A total of 951 data points of RHOmaa and Umaa, from the entire 140 m (459 ft) 2BSSS Member, were plotted on the crossplot

(Figure 3.8A). Different percentage cutoff values were applied to determine the relative proportions of the three end-member mineralogical components, and the results were compared with core data to verify lithology classification. The lithology classification was further evaluated using gamma ray (GR), sonic (DT), density (RHOB), neutron (NPHI), and photoelectric effect (PE) logs. Based on core and log data from the cored well, data points on the RHOmaa-Umaa crossplot with quartz content above 40% primarily represent siltstone, as confirmed by core data (Figure 3.8C). Points with quartz content below 40% are associated with limestone and dolomite-cemented siltstone. To differentiate limestone from dolomite-cemented siltstone, cutoff values of 50% calcite and 50% dolomite were used (Figure 3.8 B & D). Each data point was used to extract the relative proportions of the three end-member minerals (totaling 100%), providing a direct approach to evaluate lithology classification results (Figure 3.9). The results indicate that the selected cutoff values are reliable, as the lithology classification closely aligns with core data. Furthermore, the analysis confirms that in mixed lithologies, GR and DR logs are ineffective for distinguishing siltstone from dolomite-cemented siltstone, while neutron and density logs offer relatively better differentiation (Figure 3.10). Based on the verification, RHOmaa-Umaa crossplots were generated for 34 wells, from which lithology classifications were obtained. Figure 3.11 shows the lithology classification of a representative well with mixed siliciclastic–carbonate deposition, illustrating that the distinction between siltstone and dolomite-cemented siltstone is often subtle.

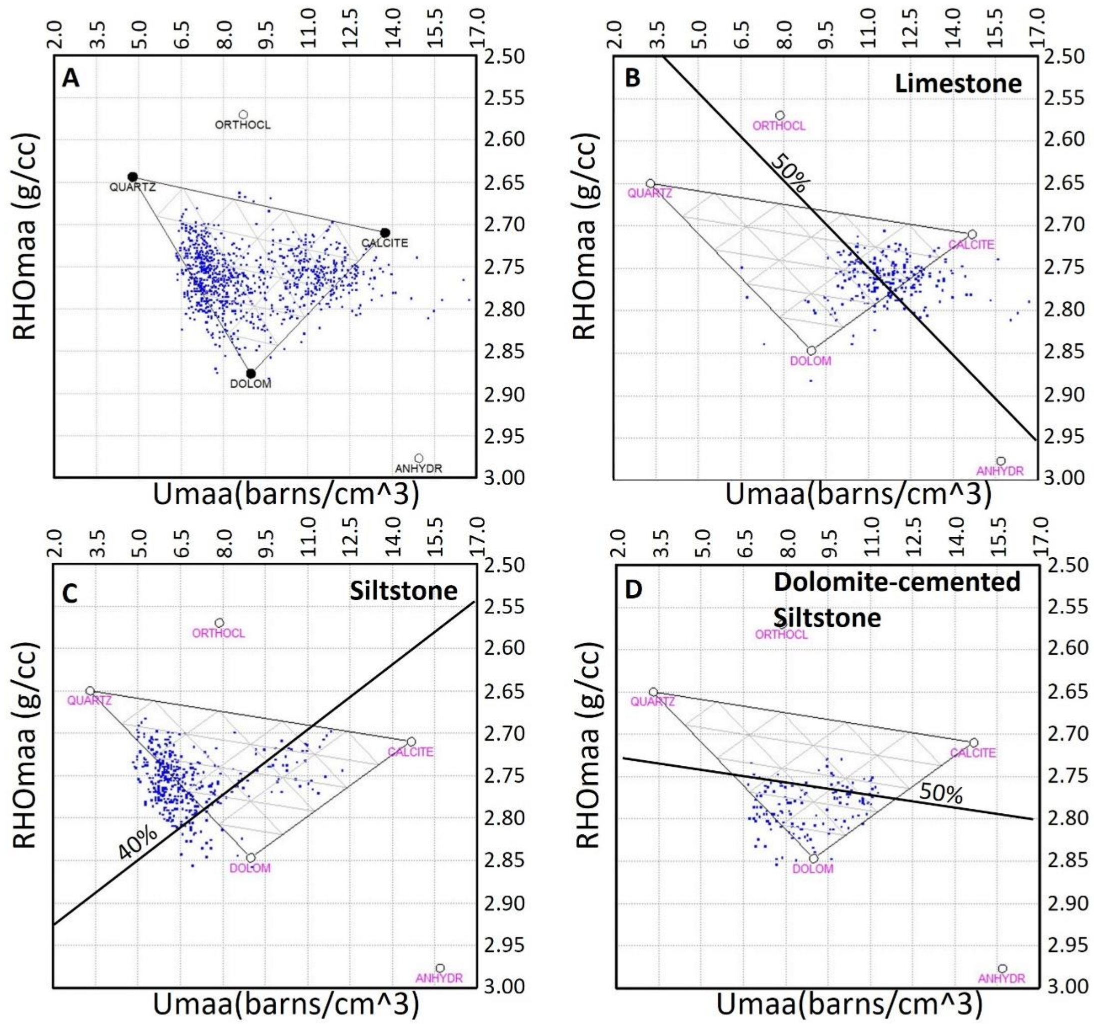

Figure 3.8: (A) RHOmaa-Umaa crossplot for the 2BSSS Member of the cored well, (B) the RHOmaa and Umaa data points for limestone, (C) the RHOmaa and Umaa data points for siltstone, and (D) the RHOmaa and Umaa data points for dolomite-cemented siltstone. The observed data distribution supports its use as a diagnostic standard for lithology classification.

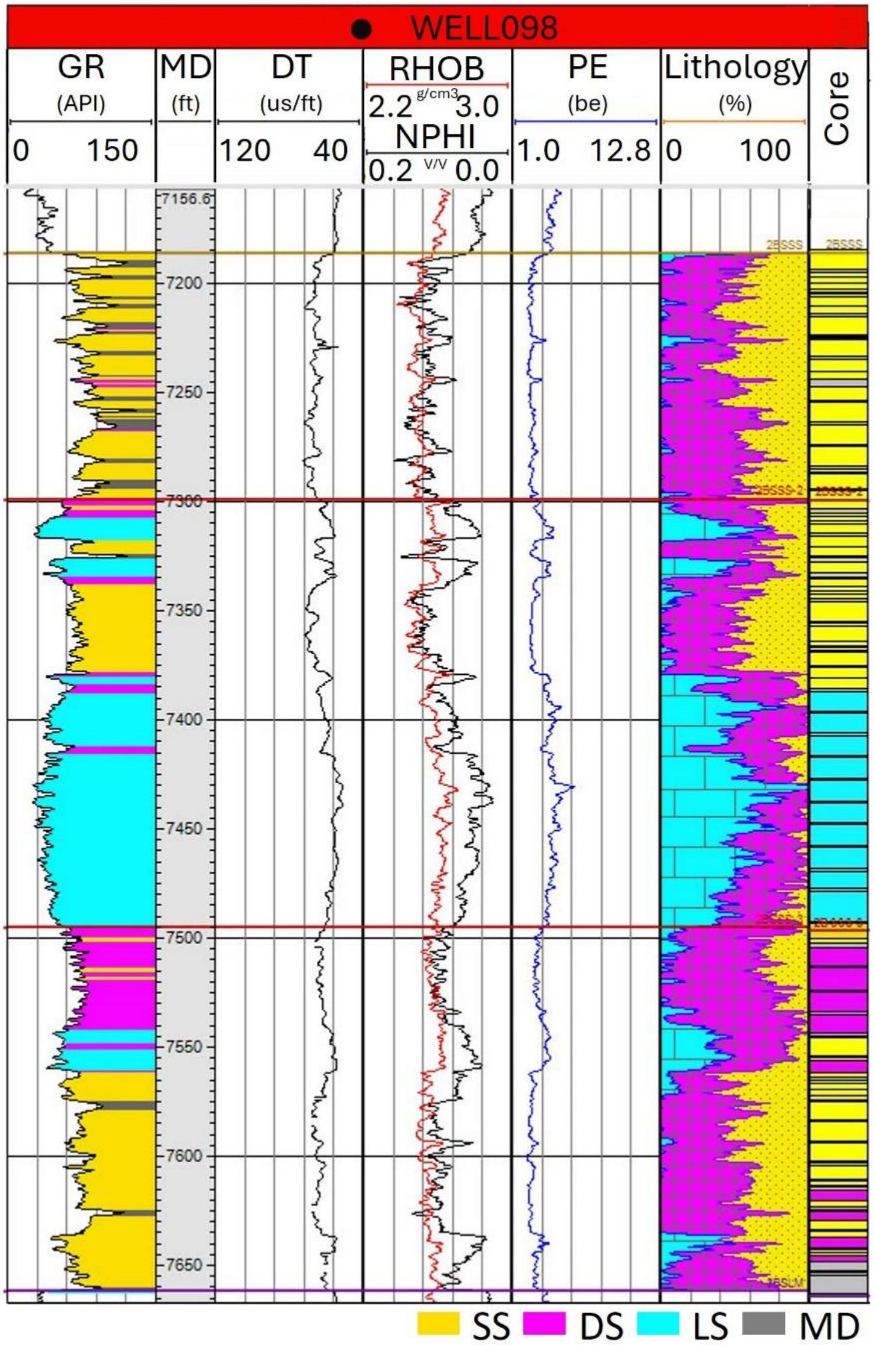

Figure 3.9: Comparison between lithology identification results based on RHOmaa-Umaa crossplot in the cored well (shown as lithology percentages in the "Lithology" column) and core-described lithology (shown in the "Core" column). The two results show good agreement: siltstone is predominantly developed in the 2BSSS-1 and 2BSSS-3 units, while the 2BSSS-2 unit is dominated by limestone.

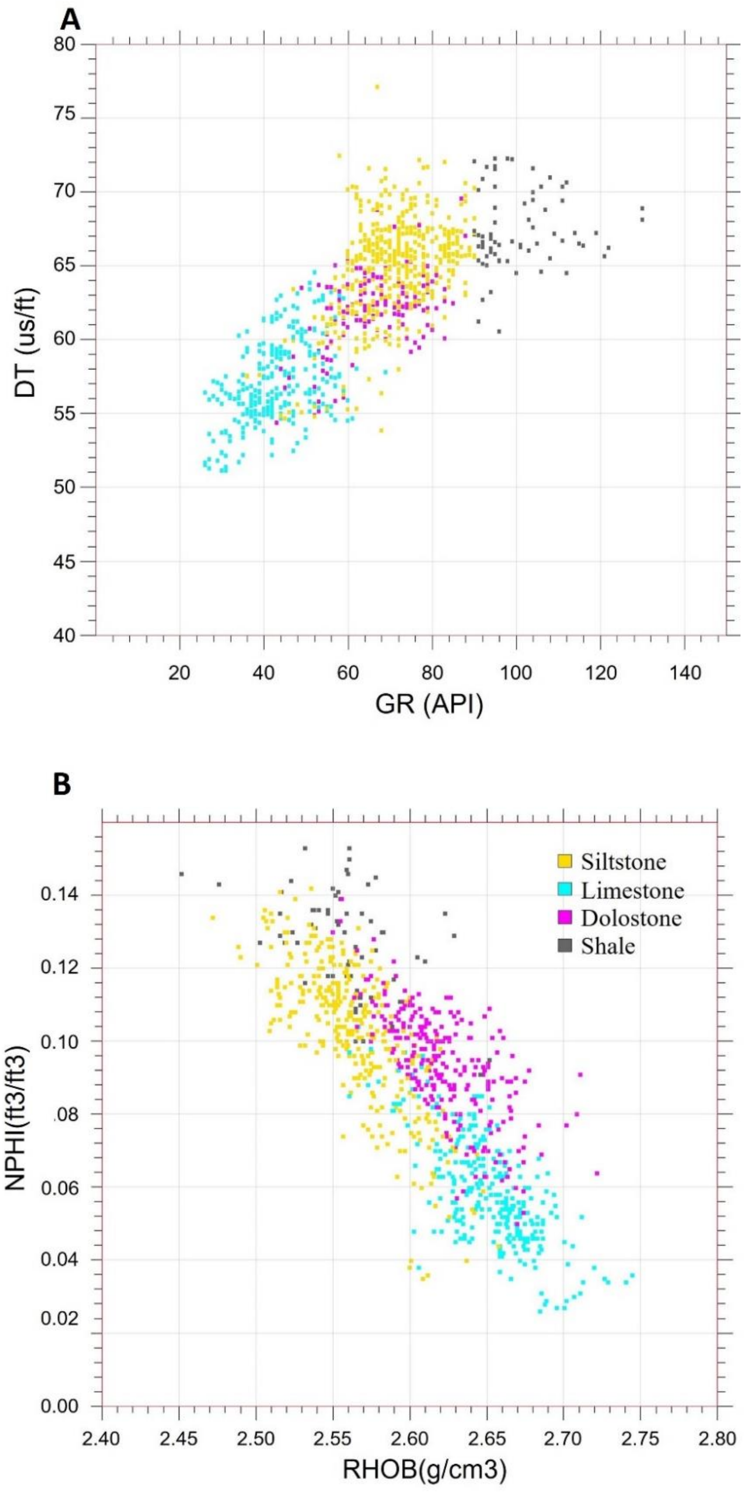

Figure 3.10: (A) Crossplot of gamma-ray (GR) versus sonic log (DT) data, and (B) crossplot of density (RHOB) versus neutron log (NPHI) data from the 2BSSS Member of the cored well. The data distribution indicates neutron logs are more effective than gamma-ray logs in distinguishing between siltstone and dolomite-cemented siltstone.

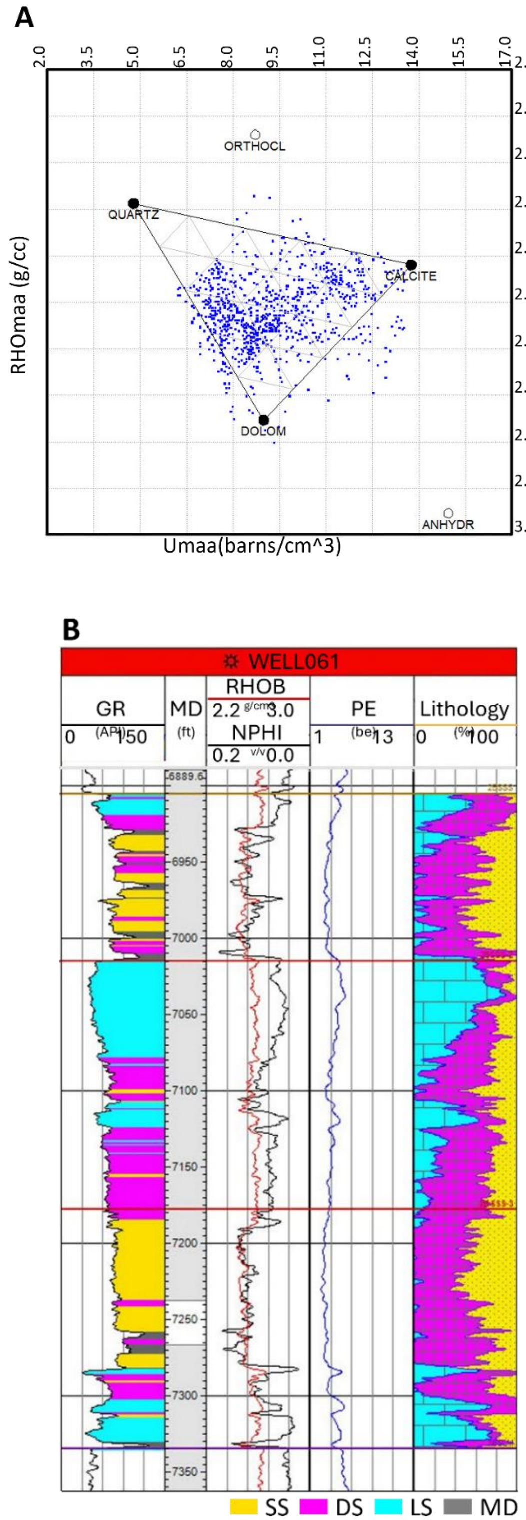

Figure 3.11: (A) RHOmaa–Umaa crossplot for one test well and (B) lithology identification result. The identified lithologies correspond well with the characteristic responses of each log curve.

3.4.3 MLP Lithology Prediction

For lithology prediction, the MLP model was trained using features extracted from four commonly available well logs: gamma ray (GR), sonic transit time (DT), density (RHOB), and neutron porosity (NPHI), as these logs are present in all wells. The training dataset included 34 wells with lithology classifications obtained through RHOmaa-Umaa crossplot analysis, accounting for 85% of the dataset. The cored well data was used for validation. Lithology predictions were performed on the remaining six wells without PE logs, comprising 15% of the dataset.

These logs were input as variables into the constructed MLP model to classify the cored well and validate the model's effectiveness. Figure 3.12 compares lithology predictions from the optimized MLP model with RHOmaa–Umaa crossplot classifications for the cored well. The confusion matrix (Figure 3.13) was constructed to evaluate the MLP model's performance on 951 records of 4 input variables. Performance metrics included accuracy (A), precision (P), recall (R), and F1-score (F1), each ranging from 0 to 1, with higher values indicating better classification. The MLP model achieved classification accuracy exceeding 0.85 across all lithologies. Limestone showed the best performance, with all values of performance metrics close to or above 0.90. Siltstone exhibited a slightly lower precision of 0.7217, mainly due to 118 misclassifications, 79 of which involved confusion with dolomite-cemented siltstone. This misclassification is attributed to similar log responses between the two lithologies. Similarly, dolomite-cemented siltstone had relatively low recall and F1-score values below 0.70. Due to class imbalance and overlapping log values with siltstone, mudstone had the lowest recall value at 0.5882.

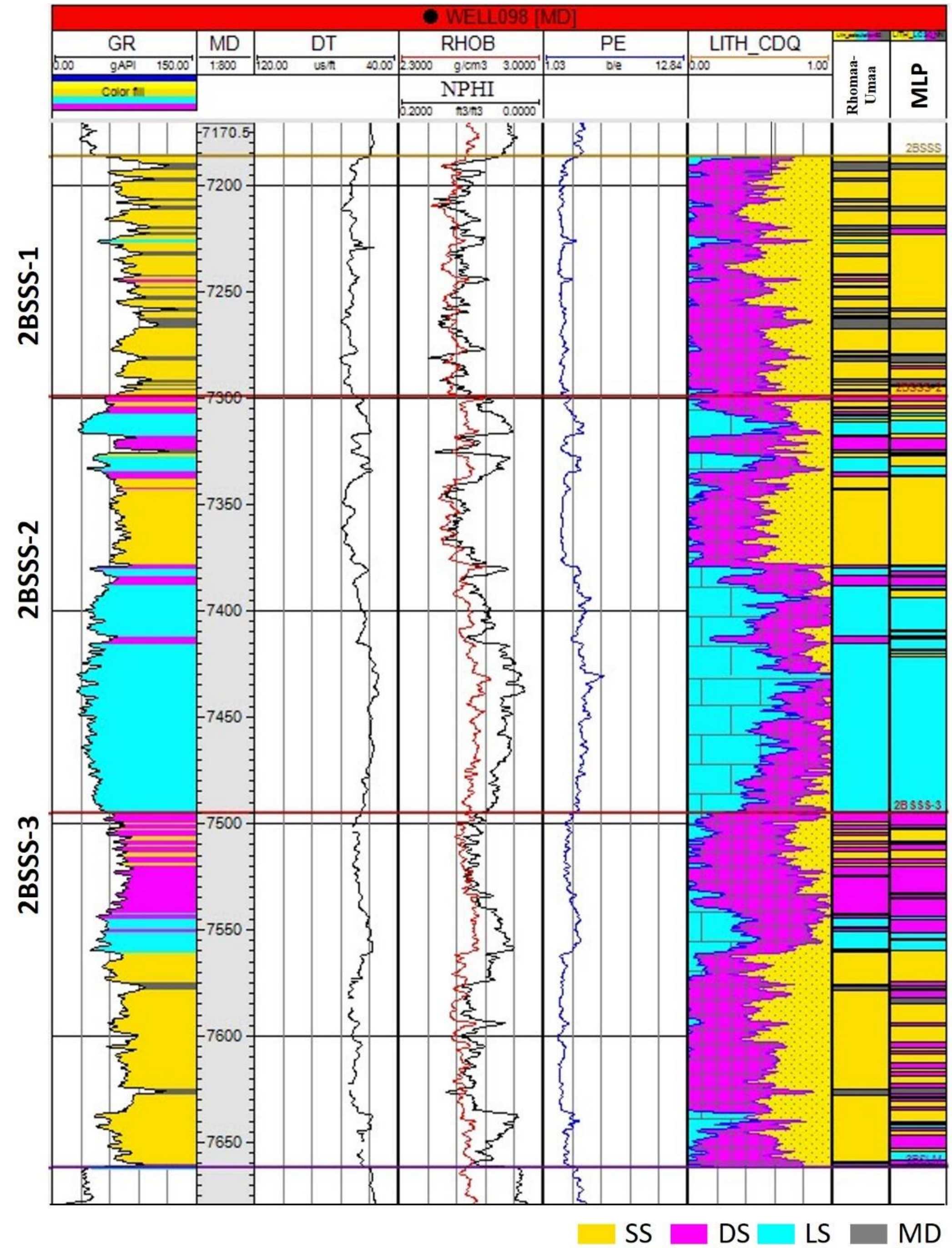

Figure 3.12: Comparison between lithology prediction results using the MLP model (shown in the "MLP" column) and lithology classification results from the RHOmaa–Umaa crossplot analysis. The MLP prediction shows a greater amount of dolomite-cemented siltstone. The MLP model predicts a slightly higher proportion of dolomite-cemented siltstone.

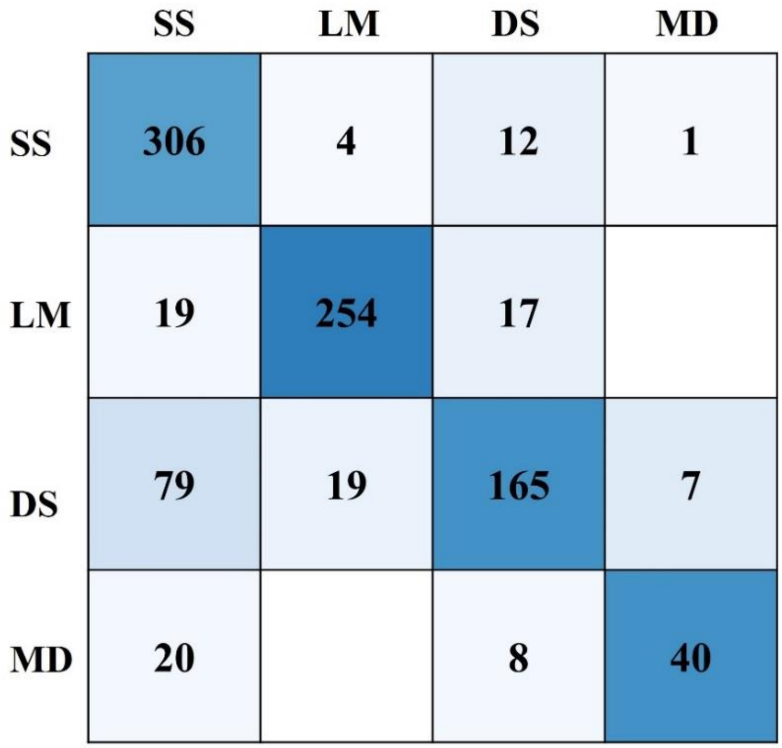

Accuracy	0.8580	0.9380	0.8507	0.9621
Precision	0.7217	0.9170	0.8168	0.8333
Recall	0.9474	0.8759	0.6111	0.5882
F1-Score	0.8193	0.8959	0.6992	0.6897

Figure 3.13: Confusion matrix of the MLP prediction results. The prediction accuracy for all four lithologies exceeds 0.85 (total samples = 951). Misclassifications primarily involved confusion between siltstone and dolomite-cemented siltstone (n = 79).

Overall, validation results confirmed that the MLP model proved effective for lithology classification by leveraging combined input log features.

The validated MLP model was subsequently applied to classify lithologies in the remaining six wells of the test dataset. Figure 3.14 exhibits prediction results for two wells, showing strong agreement with known well log patterns: limestone corresponds to low gamma-ray values, while siltstone shows moderate gamma-ray responses and high neutron values. The classification results were compared with lithologies of the cored well derived from a well-log crossplot to assess prediction accuracy. Figure 3.15A presents the density and neutron crossplot for cored well, and Figure 3.15B shows the corresponding plot for the six predicted wells, whose values show highly similar distribution patterns and value ranges, indicating strong consistency. These findings confirm that the MLP model successfully captured the diagnostic features of the four lithologies from well-log data, effectively managing complex dependencies and producing reliable lithologic predictions. These results confirm that the MLP model effectively captured the diagnostic features of the four lithologies from well-log data, accurately handling complex dependencies and achieving reliable lithofacies predictions.

Lithology classifications for all 40 wells in the 2BSSS member were obtained by integrating RHOmaa–Umaa analysis with MLP classification results. Statistical analysis (Figure 3.16) indicates that limestone remains the most dominant lithology, accounting for 45%. It is followed by siltstone at 30.5%, dolomite-cemented siltstone at 20.9 %, and mudstone at 3.6 %. Siliciclastic rocks, which are the primary hydrocarbon reservoirs, make up only 51.4 % of the total volume in the 2BSSS member. Siltstone is more abundant in 2BSSS-1 and 2BSSS-3 units, accounting for 9.7 % and 13.6 % respectively.

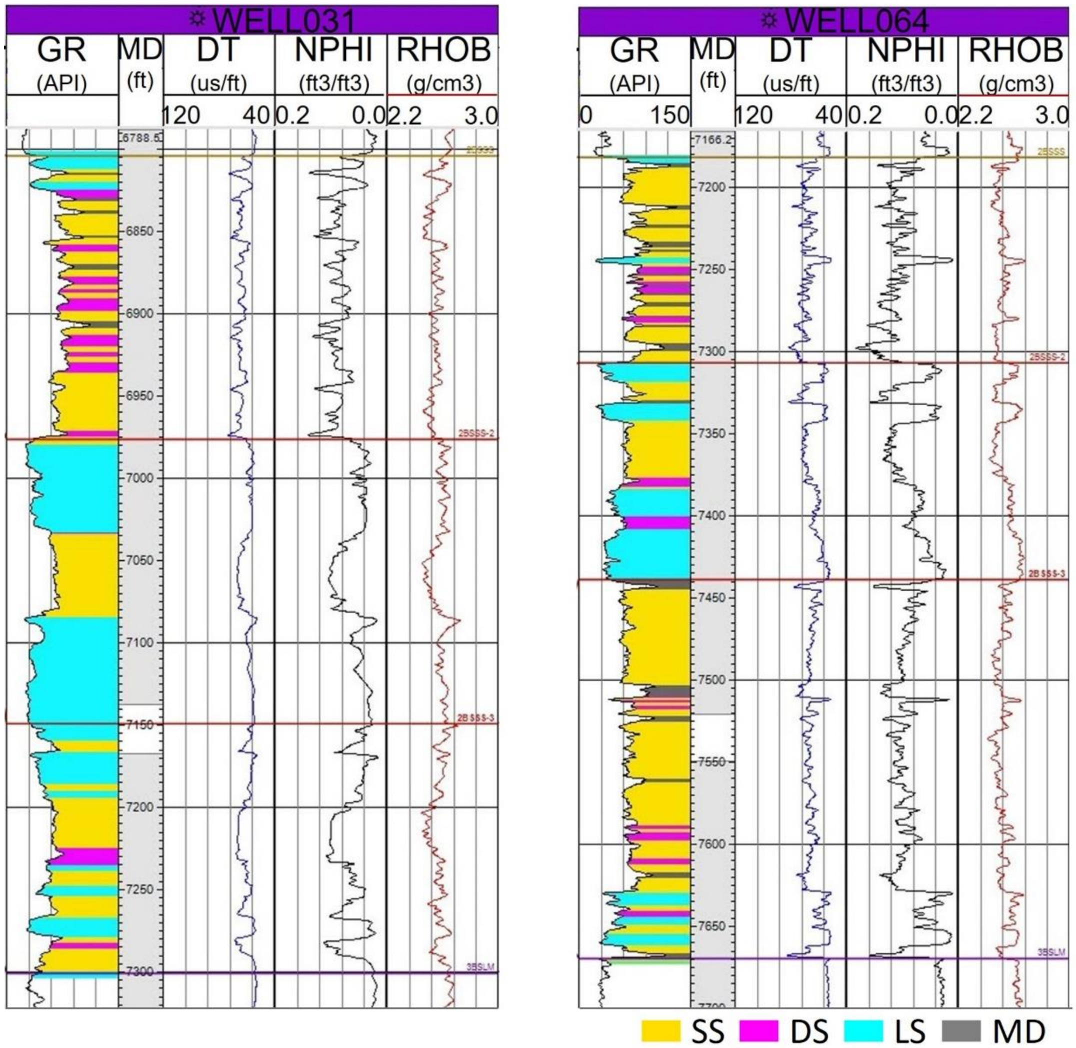

Figure 3.14: MLP lithology prediction results for two test wells. The predicted lithologies show good agreement with the characteristic log signatures of each lithology.

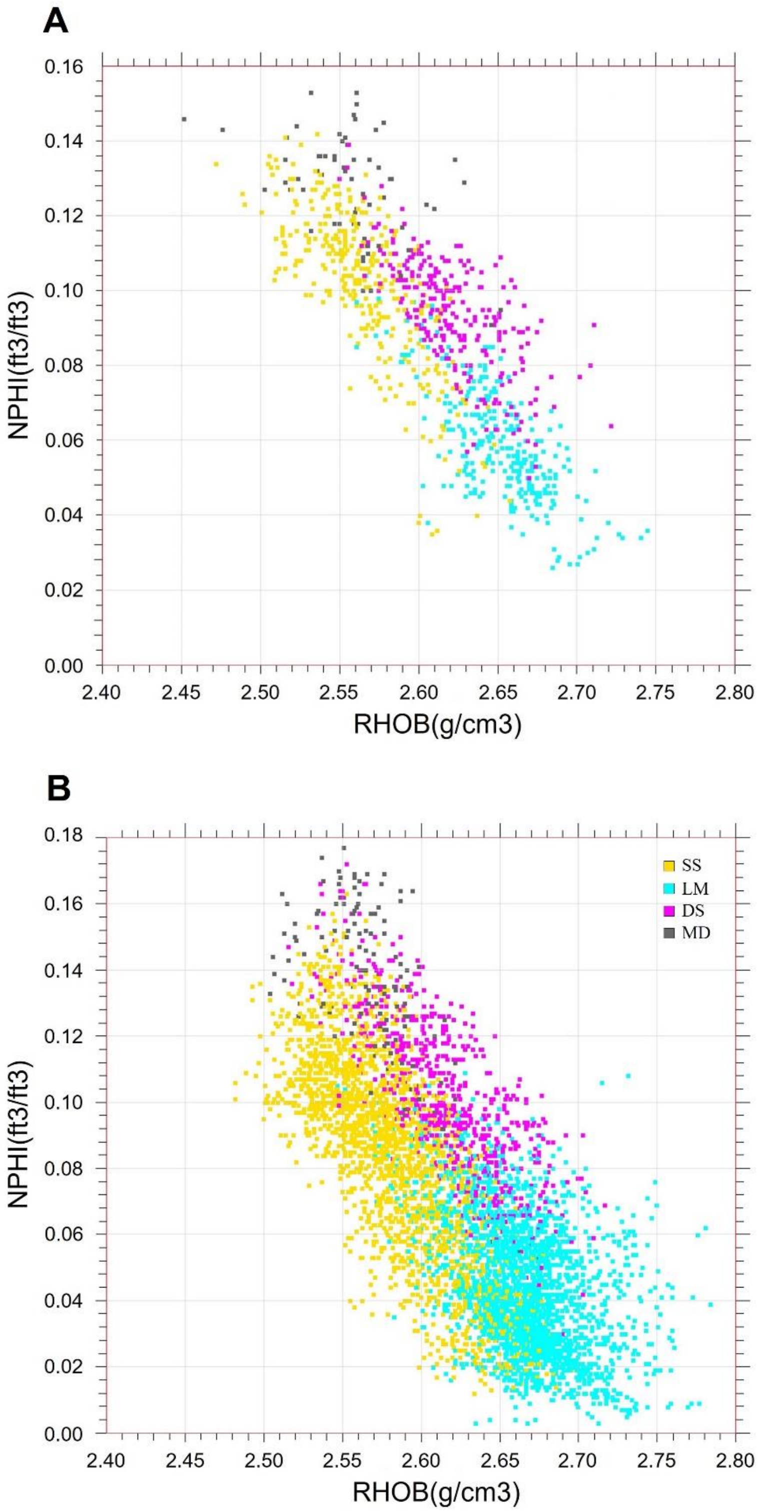

Figure 3.15: (A) Density–neutron crossplot from a cored well; (B) Crossplot from six MLP-predicted wells. The data exhibits similar distribution trends and value ranges across all wells.

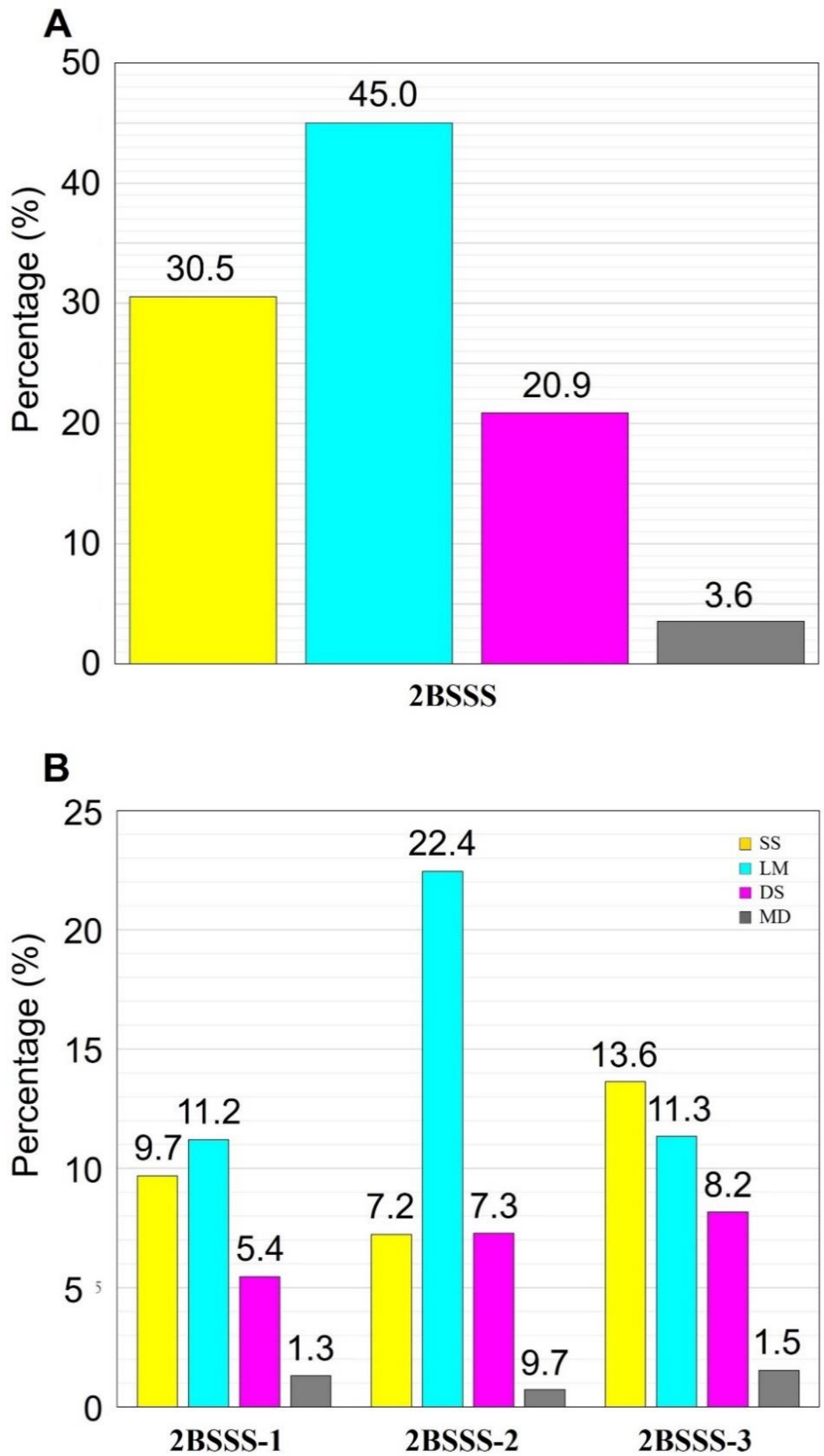

Figure 3.16: (A) Proportions of each lithology within the entire 2BSSS Member; (B) Lithology proportions within each unit of 2BSSS. Siltstone and dolomite-cemented siltstone account for 51.4% of the 2BSSS Member, primarily concentrated in the 2BSSS-1 and 2BSSS-3 units.

The classification results show that siltstone and dolomite-cemented siltstone have similar gamma ray values, which makes them difficult to distinguish using gamma logs alone (Figure 3.17). In contrast, neutron logs effectively differentiate between the two lithologies, consistent with core-calibrated well observations.

This study found that MLP performance is highly sensitive to the number of input features. How different combinations of input variables affect model performance are evaluated. In the minimal-input scenario, the model was trained using only GR and NPHI. The RHOmaa–Umaa analysis showed that the four lithologies have distinct NPHI distributions, although siltstone and dolomite-cemented siltstone overlap in GR values. With limited inputs, the MLP struggles to fully capture lithological differences, achieving a lower accuracy of siltstone. In the expanded-input scenario, seven input variables were used: GR, RHOB, DT, NPHI, and multiple resistivity logs (deep, medium, and shallow resistivity). However, multiple similar resistivities introduced redundancy, leading to model overfitting. Although training accuracy exceeded 0.85, testing accuracy dropped to about 0.80, and the accuracy became unstable across different wells. To avoid underfitting and overfitting, four input variables (GR, RHOB, DT, and NPHI) represent distinct physical properties are selected, rather than redundant logs. GR differentiates mudstone; RHOB and NPHI identify dolomite-cemented siltstone; DT distinguishes dolomite from siltstone. This configuration achieved an overall prediction accuracy of above 0.86 for each lithology. These results highlight key limitations of using MLP for lithology prediction. Specifically, MLP performance is highly sensitive to input selection, and high correlations among features can cause overfitting. Therefore, thoroughly analyzing input data, such as using crossplots to understand log responses to lithologies, is essential before applying

MLP. Importantly, adding more input features does not necessarily improve model performance.

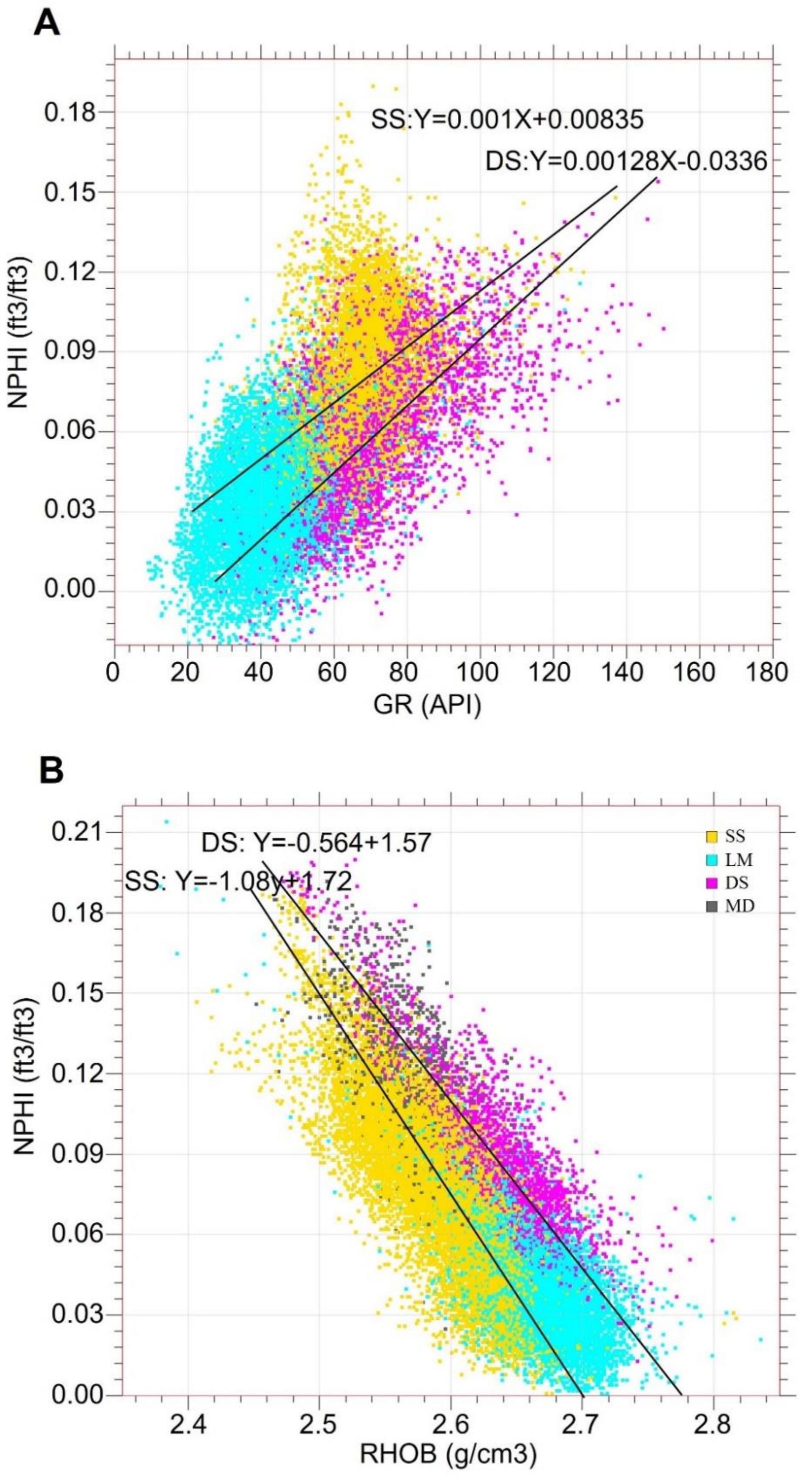

Figure 3.17: (A) Gamma-ray versus neutron crossplot from 40 wells; (B) Density–neutron crossplot from 40 wells. The data distribution shows that density–neutron crossplots provide relatively more apparent separation among the four lithologies and can serve as a more reliable basis for lithology identification in the study area.

3.4.4 Bayesian Lithology Inversion

To predict the spatial distribution of lithology by effectively linking seismic and well log data, Bayesian lithology inversion was applied to integrate elastic rock properties (P-wave impedance, S-wave impedance, and Vp/Vs ratio) with lithology classifications derived from well logs. Model-based post-stack seismic inversion was first conducted within the sequence stratigraphic framework. The resulting impedance values varied across lithologies, making them effective for lithology prediction. Figure 3.18 shows the extracted P-wave impedance for the upper (2BSSS-1) and lower (2BSSS-2 and 2BSSS-3) parts of the 2BSSS member, respectively. The impedance maps reveal northwest-southeast trending belts of relatively low impedance. A crossplot between the P-wave impedance from the borehole-side trace and the neutron log demonstrates that limestone has a higher impedance, while siliciclastic rocks have a lower impedance (Figure 3.19A). This trend is consistent with the crossplot derived from well logs (Figure 3.19B). Therefore, the low-impedance belts in the seismic inversion data indicate zones of siliciclastic rock distribution. Based on this preliminary result, P-wave impedance combined with Vp/Vs ratio was used to classify and predict lithology within the 2BSSS member. These lithologic proportions obtained from the above analysis were incorporated as prior probabilities in the Bayesian lithology classification. The Bayesian conditional probability approach was applied to calculate the probability density functions (PDFs) of impedance parameters for the four lithologies. The results show that siliciclastic rocks and limestone can be effectively differentiated, whereas mudstone classification is less reliable. Figure 3.20 shows a 2-D kernel density estimation visualization of impedance parameters, with P-impedance on the x-axis, Vp/Vs ratio on the y-axis, and lithology classification probability

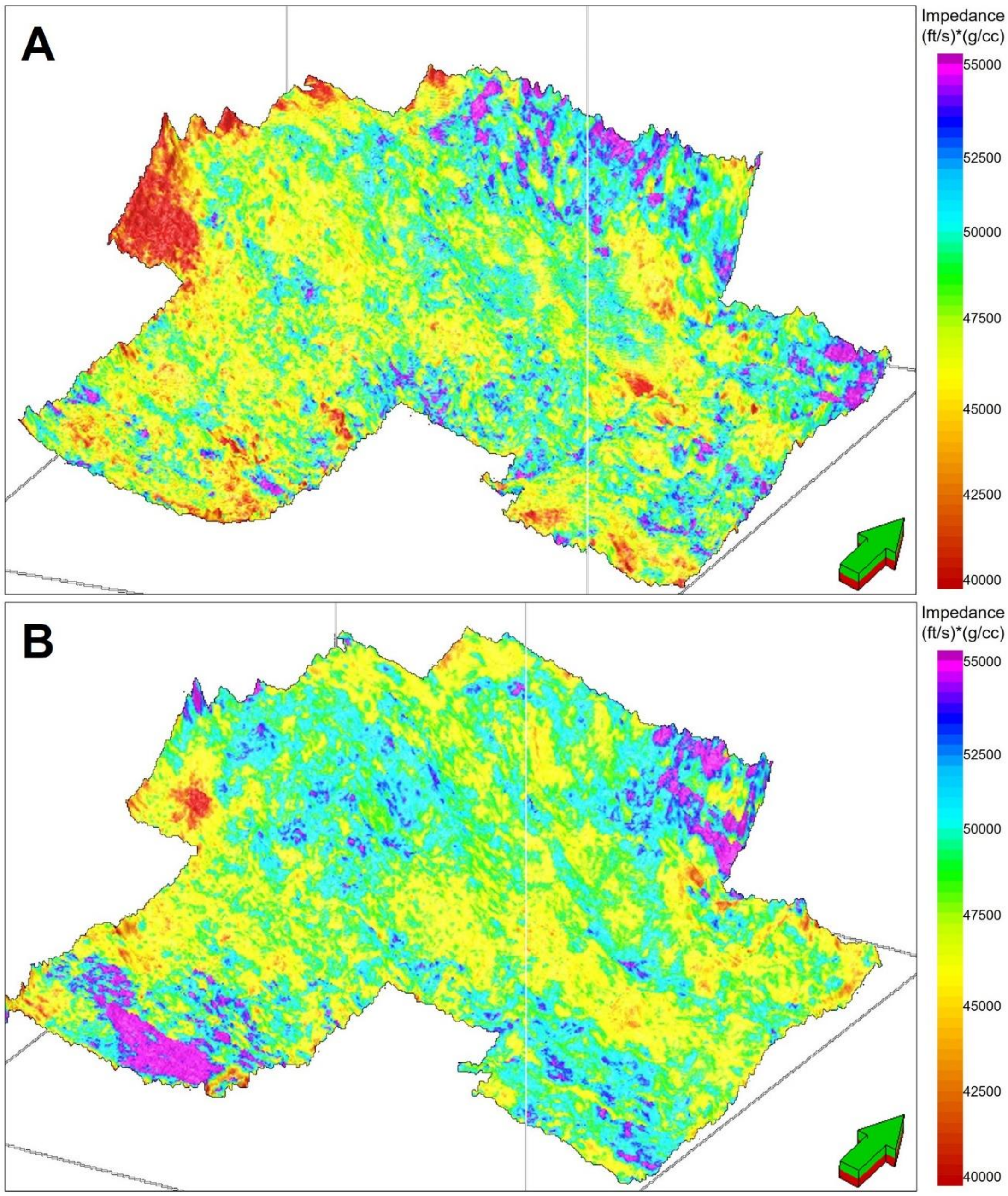

Figure 3.18: (A) P-wave impedance extraction for the 2BSSS-1 unit; (B) P-wave impedance extraction for the 2BSSS-2 and 2BSSS-3 units. The results show a northwest-southeast trending, banded distribution of low-impedance siltstone.

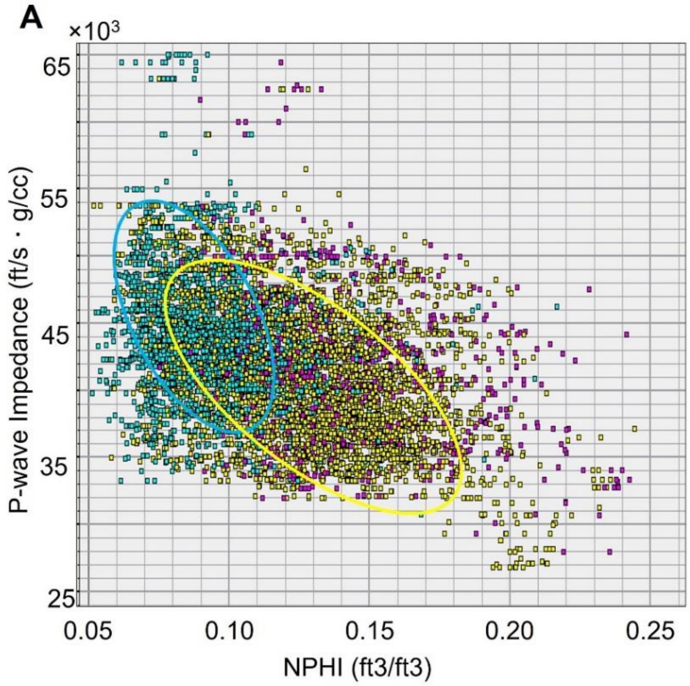

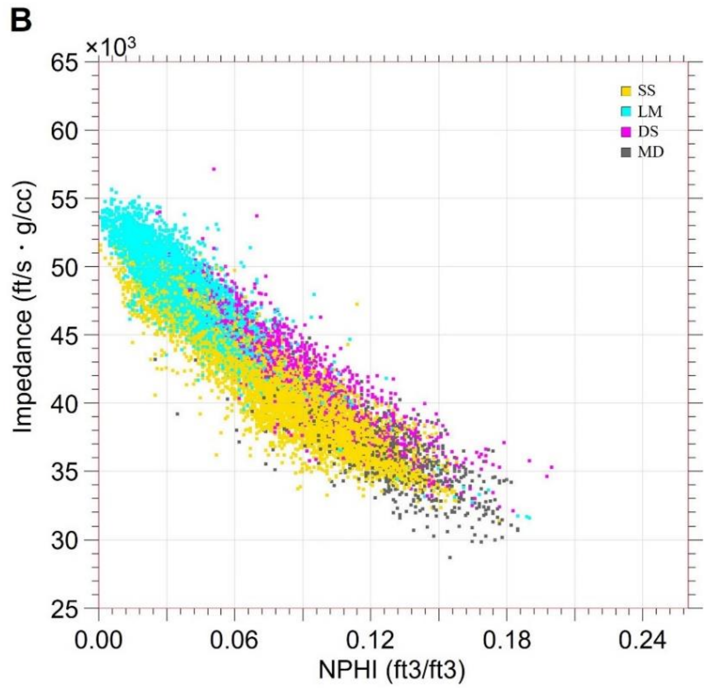

Figure 3.19: (A) Crossplot of P-wave impedance extracted from borehole-side trace and neutron log in the cored well; (B) Crossplot of P-wave impedance calculated from sonic and density logs versus neutron log in the same well. Both plots exhibit similar distribution patterns, indicating consistency between seismic-derived and log-derived impedance values.

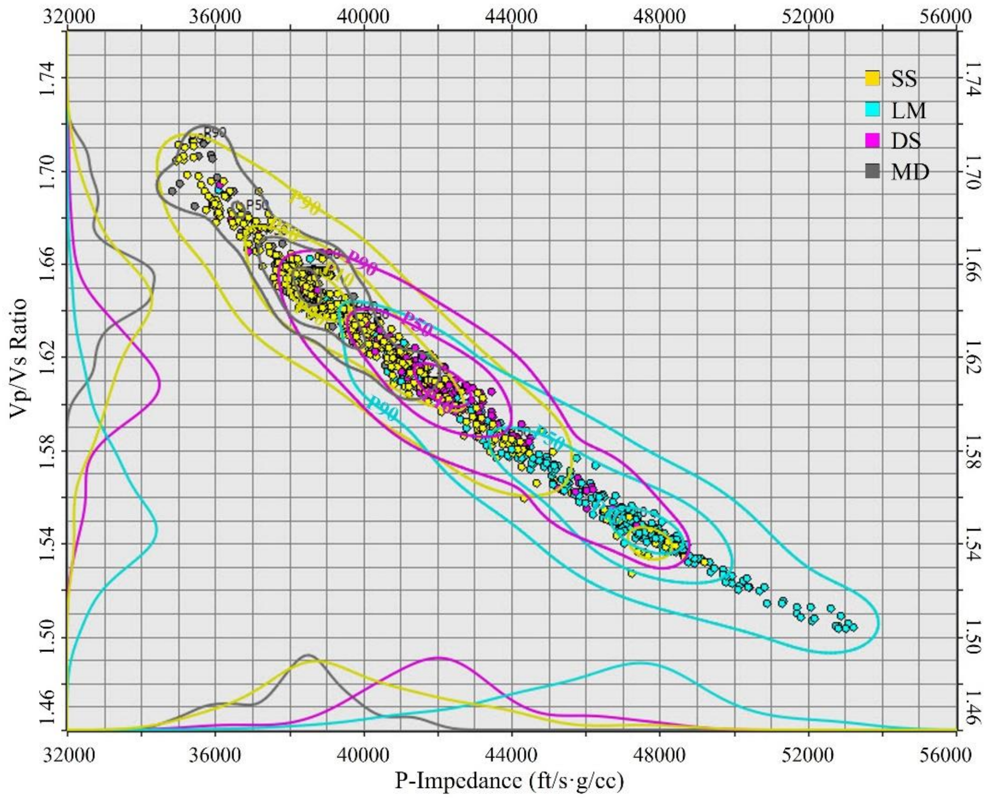

Figure 3.20: The kernel density distribution of Bayesian lithology inversion results extracted from the well-side seismic trace of the cored well shows limited overlap between siltstone and limestone and partial overlap between siltstone and dolomite-cemented siltstone. However, the P50 values for each lithology are separated.

on the z-axis, which exhibits P10, P50, and P90 distributions for each lithology. Although there is a minor ove rlap between the siltstone and limestone, their P50 distributions are clearly separated, indicating effective lithological differentiation. Likewise, dolomite-cemented siltstone is reasonably well distinguished from limestone. However, despite the separation of P50 distributions between dolomite-cemented siltstone and siltstone, they have considerable overlap, resulting in only moderate classification accuracy. Substantial overlap between mudstone and siltstone results in poor differentiation. This finding aligns with the previous analysis, which found that mudstone contains a high proportion of silt. As a result, Bayesian conditional probability classification provides reliable predictions for siltstone, dolomite-cemented siltstone, and limestone. Although mudstone classification is less effective, its limited occurrence (3.6%) and high silt content suggest that the overall lithological classification remains robust.

Based on the above Bayesian conditional probability training model, Bayesian lithology inversion was performed by integrating the optimal PDF model derived from 40 wells with the 3-D P-wave impedance volume. Figure 3.21 shows predicted lithology profiles through two wells. The results confirm that predictions align with prior information at the well sites and capture lateral lithological variations, enabling effective spatial mapping of lithology distribution. In addition, the inversion results reveal complex lithological variations within the 2BSSS. To quantitatively analyze lithological variation, lithology probability volumes were calculated to characterize spatial distribution. Figure 3.22A shows the lithology distribution in the 2BSSS-1 unit, and Figure 3.22B presents the associated siltstone probability. Limestone dominates this unit, whereas siltstone appears in northeast–southwest-trending belts with localized high-probability zones (>50%).

Figure 3.23A and Figure 3.23B show that siltstone is the dominant lithology in the 2BSSS-2 and 2BSSS-3. It appears as a sheet-like, continuous distribution due to stacking effects. However, high probability siltstone zones (>50%) still exhibit localized or belt-like geometries. Dolomite-cemented siltstone appears randomly intermixed within siltstone and lacks regional continuity in all units. Due to its low content, mudstone is not visualized in the mapping because of stacking effects. It is important to note that isolated “bull’s-eye” anomalies in the lithological and probability maps are artifacts caused by the post-stack inversion algorithm and data limitations. These do not represent actual geological features and should be interpreted cautiously, incorporating regional geological knowledge to ensure reasonable interpretation.

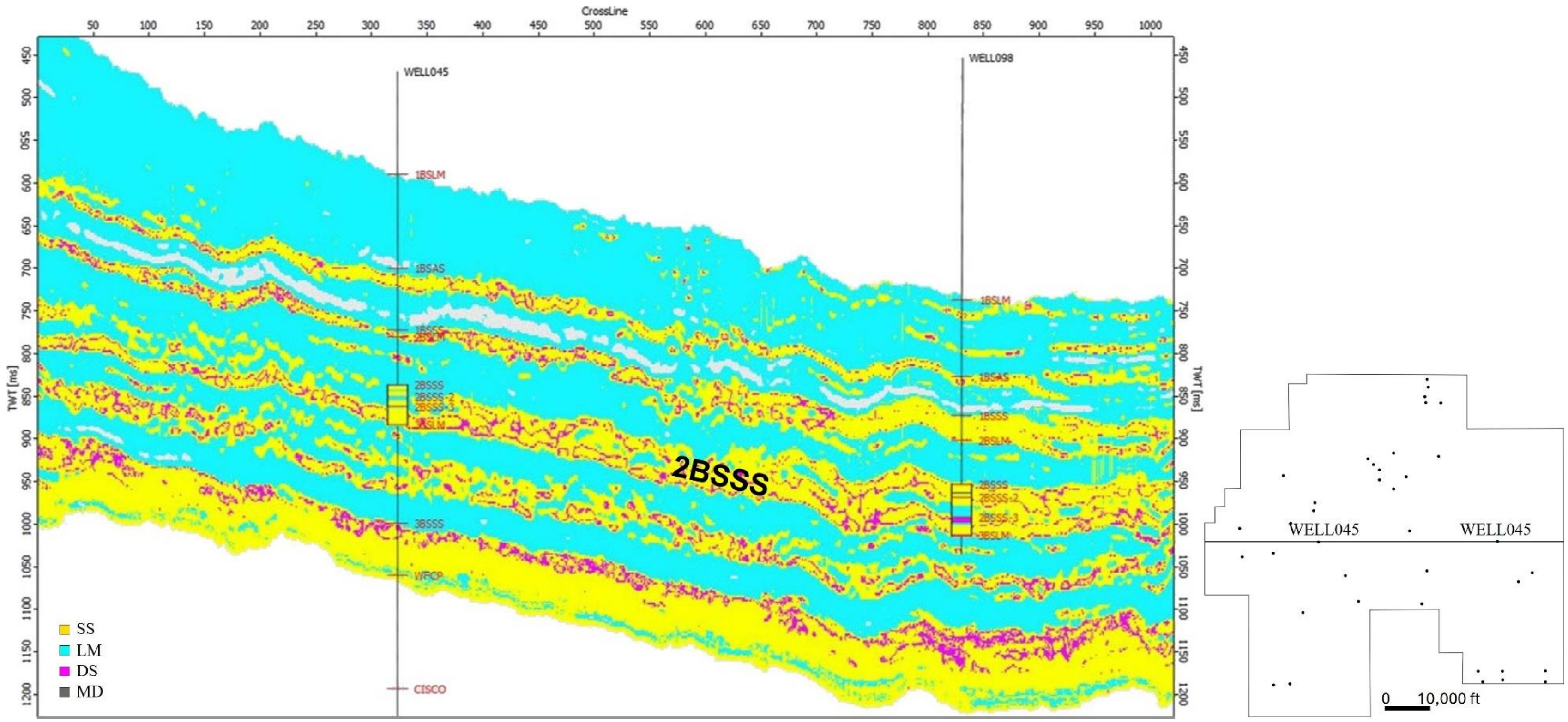

Figure 3.21: A profile of Bayesian lithology inversion results shows increased siltstone content in the lower part of the 2BSSS Member, and limestone is rich in the middle unit, consistent with well-log-based lithology predictions.

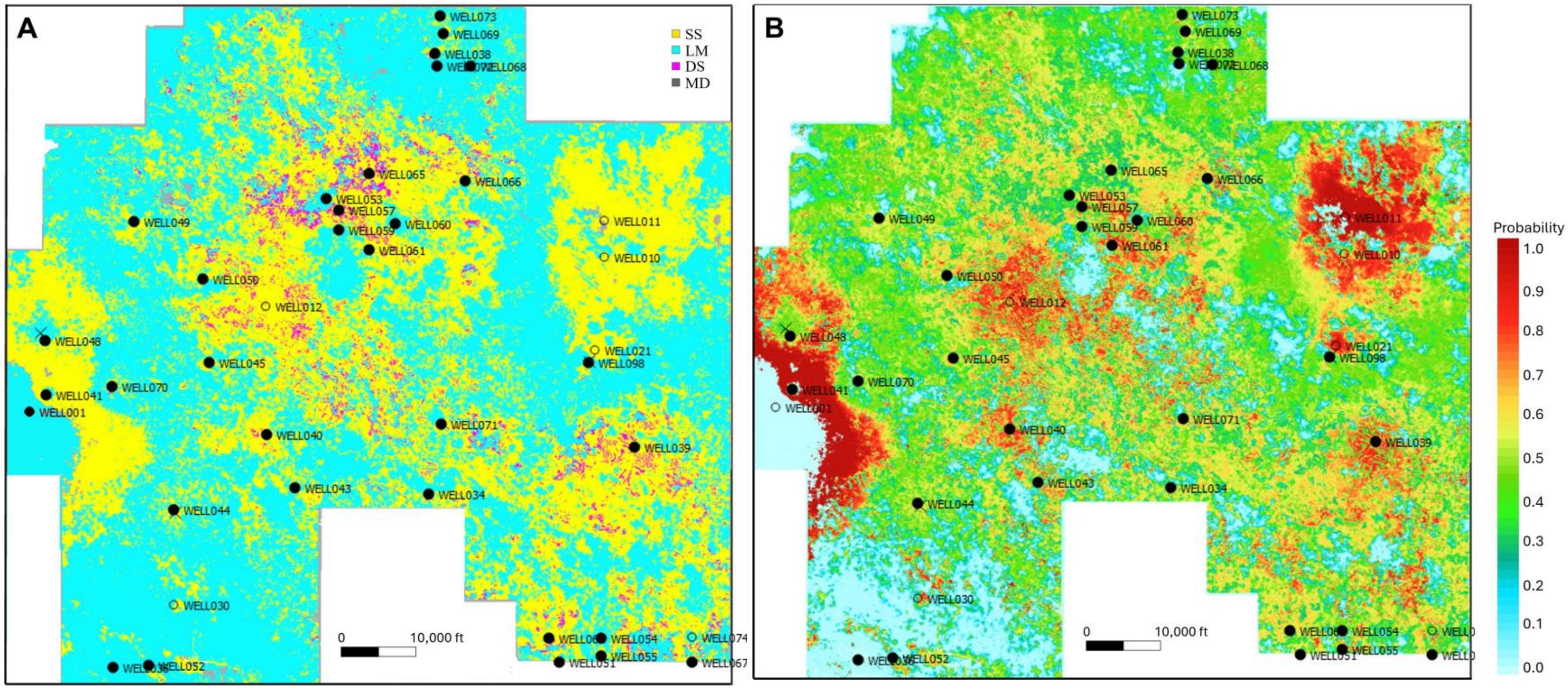

Figure 3.22: (A) Bayesian-inverted lithology distribution extracted from the upper part of the 2BSSS Member (corresponding to the 2BSSS-1 unit), showing siltstone distributed in a northwest–southeast-oriented banded pattern. (B) Corresponding siltstone probability within the unit.

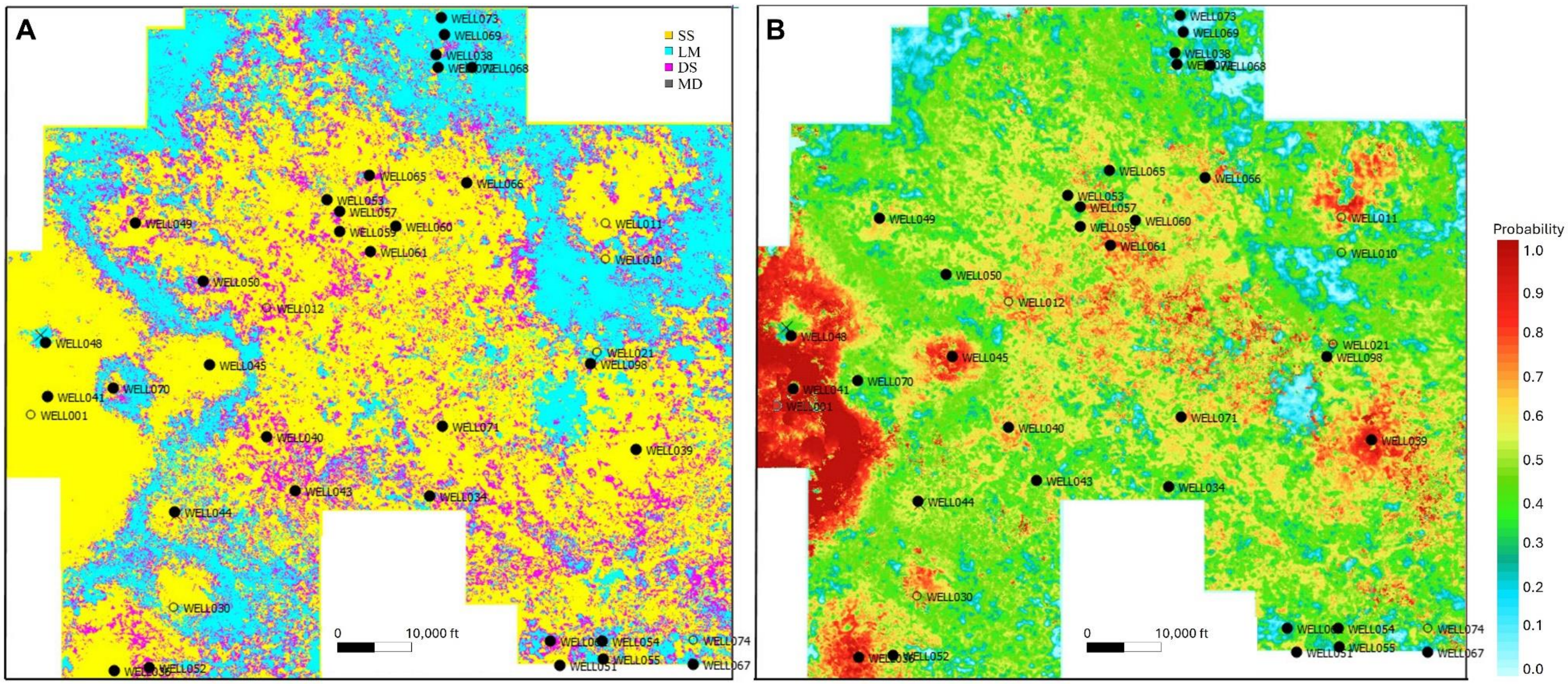

Figure 3.23: (A) Bayesian-inverted lithology distribution from the lower part of the 2BSSS interval (corresponding to the 2BSSS-2 and 2BSSS-3 units), showing a higher abundance of siltstone. (B) Corresponding siltstone probability map, revealing a continued trend of banded distribution.

3.5 DISCUSSION

3.5.1 Sequence Stratigraphic Control on Depositional Trends

The high-frequency sequence stratigraphic framework of the 2BSSS Member reveals a multi-cyclic stacking pattern controlled by relative sea-level fluctuations, which strongly influence depositional trends at the depositional system scale. Outcrop studies (Gardner and Borer, 2000; Ruppel and Ward, 2013; Kerans et al., 2017) show that stacked high-frequency sequences characterize the Bone Spring Formation. Hurd et al. (2016) attribute this stratigraphic architecture to the complex interplay among relative sea-level fluctuations, sediment gravity flows, and slope morphology. This study shows that the stratigraphic architecture of each 2BSSS unit varies significantly from the lower slope to the basin floor, with these variations exerting firm control on depositional trends. The seismic amplitude and coherence blended image of the lower part of 2BSSS (Figure 3.24), corresponding to 2BSSS-2 and 2BSSS-3 units, shows turbidite distribution across multiple zones, with multiple depositional trends extending from the lower slope to the basin floor. These Depositional trends originate from point sources rather than line sources along the structural strike, exhibit elongated geometries, and extend continuously over 20 km (12 mi) along a northwest-southeast depositional strike and dip direction. These trends are primarily controlled by a low-relief, southeast-dipping, stable slope that provided high accommodation and facilitated progradation during relative sea-level fall. In the 2BSSS-3 unit, the well cross-section across the lower slope reveals two to three depositional cycles, marked by low-gamma limestone beds separating high-gamma siliciclastic beds (the c-c' profile in Figure 3.7). Sharp basal contacts and upward-fining trends characterize each cycle. These high-frequency depositional cycles thin and become less distinct toward the

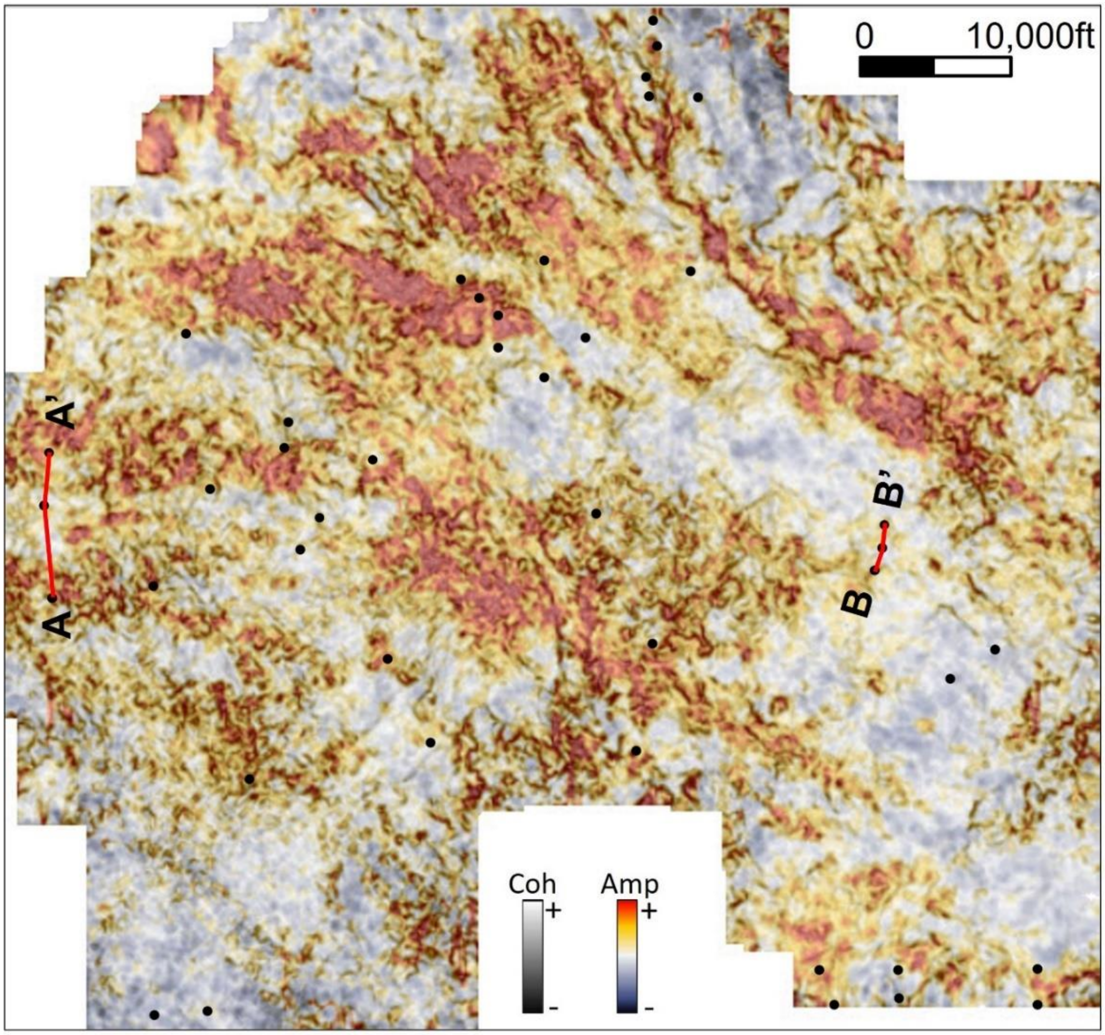

Figure 3.24: Blended display of RMS amplitude and coherence attributes for the lower part of the 2BSSS (corresponding to the 2BSSS-2 and 2BSSS-3 units). High-amplitude zones associated with siltstone exhibit a northwest-southeast oriented, banded distribution from the slope to the basin.

basin floor. Fine-grained lithologies dominate the area, indicating that the 2BSSS turbidite system was deposited in a low-energy environment. These characteristics suggest that regression increased sediment flux from the relict platform to the slope, promoting the widespread development of turbidite deposits across the study area. In addition, high sediment supply enabled erosive gravity flows to carve confined, preferential transport pathways, resulting in vertically stacked turbidite deposits within linear depositional trends. As a result, the three units of the 2BSSS Member exhibit strong allogenic controls on sediment supply and stratigraphic architecture, emphasizing the influence of high-frequency relative sea-level fluctuations on sequence architecture and internal depositional trends. These fluctuations increased the frequency and volume of basinward-prograding turbidite influxes, shaping the spatial distribution of lithology across the study area.

3.5.2 Lithological Variability Within Depositional Trends

This study indicates that variable stacking patterns and geometries along the slope-to-basin transition within the 2BSSS member reflect complex lithological changes within the depositional trends. Outcrop studies by Hurd et al., (2018) and Walker et al., (2021) documented a distinct transition in the Bone Spring Formation from proximal carbonate-rich gravity flows to distal siliciclastic turbidites, where coarse-grained sediments accumulated in high-energy slope environments, while finer-grained material was transported into lower-energy basin settings. Although siltstone-rich turbidites are encountered across the study area, significant lithologic variation exists from the lower slope to the basin floor. Downslope-transported turbidite complexes formed elongate packages with sublinear to sinuous geometries, dispersing distally on the basin floor. Seismic attributes (Figure 3.24) show widths ranging from 1 km to 2.5 km (0.6 mi to 1.5

mi) on the lower slope, expanding to over 5 m (3.1 mi) on the basin floor. These geometries and scales are comparable to outcrops of turbidites in the Delaware Mountain Group (Gardner and Borer, 2000; Gardner et al., 2003; Hurd et al., 2016; Kane et al., 2017). Rapid lateral changes between siltstone and limestone over short distances indicate strong heterogeneity within the turbidite complexes. Vertically, well logs show that the turbidite complex within each stratigraphic unit comprises stacked siltstone interbedded with limestone, which is interpreted as the result of multiple pulsed depositional events, suggesting significant vertical heterogeneity.

Although lithologic continuity dominates along depositional trends, appreciable variations in siltstone thickness and log responses are observed from the lower slope to the basin floor. On the lower slope, siltstone typically exhibits cylindrical or bell-shaped gamma-ray responses. Thick siltstone beds interbedded with abundant limestone reflect proximal sediment flux and upward compensational stacking. Siltstone beds range from 5 m (16.4 ft) for isolated units to as much as 20 m (65.6 ft) for thicker assemblages (Figure 3.25A). In contrast, basin floor siltstone beds show thin, serrated gamma-ray responses and sparse, thin limestone, reflecting reduced sediment input from a waning feeder system and a change in stacking style. The thickness of individual siltstone beds significantly decreases to about 1.5 m (5 ft) (Figure 3.25B). Distal low-energy conditions and dispersive depositional style increased siltstone content and cumulative thickness, aligning with Bayesian lithology prediction results. Regarding siltstone connectivity, basin floor siltstone exhibits better lateral continuity than those on the lower slope. As a result, the 2BSSS turbidite complexes record a downslope transition in sediment flux and depositional style, firmly controlling lithologic distribution.

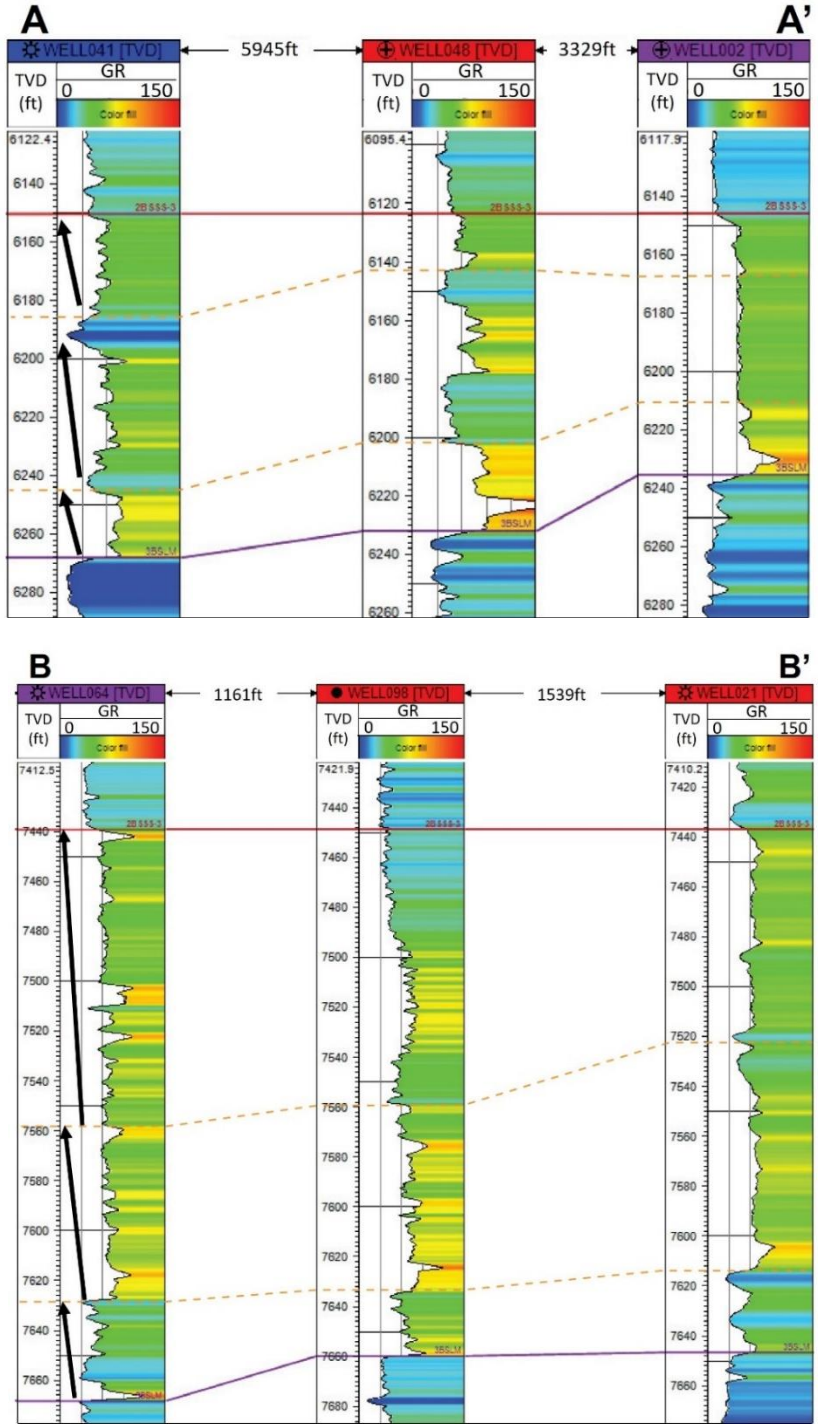

Figure 3.25: (A) In the lower slope area, siltstone within the 2BSSS-3 unit exhibits a cyclic pattern of thick stacked beds. (B) In the basin floor, siltstone exhibits continuous thin-layer stacking; although thickness increases, the cyclicity becomes less apparent. The locations of both sections are indicated in Figure 3.24.

3.5.3 Lithologic Control on Reservoir Quality

Reservoir properties within the 2BSSS Group exhibit heterogeneity driven by depositional cyclicity, lateral lithological variation, and diagenetic processes. The current porosity and permeability reflect lithology as the dominant control on reservoir quality. Kerans and Ruppel (2020) pointed out that variations in quartz, carbonate, and clay content influence the storage capacity of Bone Spring reservoirs. Montgomery (1997a and 1997b) noted that dolomite cement significantly alters porosity and permeability. To assess reservoir quality in the 2BSSS Member, we compared permeability derived from neutron porosity logs across four lithologies. The results show that siltstone within the hybrid turbidite deposits exhibits significantly higher porosity and permeability than limestone, indicating better reservoir quality. However, diagenetic cementation has locally reduced the reservoir properties of some siltstones. Within the 2BSSS Group, reservoir porosity typically ranges from 3% to 12% and permeability from 0.001 to 0.15 mD. Siltstone exhibits porosity values ranging from 6% to 10%, with an average of 8%, and permeability ranges between 0.005 and 0.15 mD, with an average of 0.05mD. Post-depositional dolomite cementation significantly reduces reservoir quality. Dolomite-cemented siltstone exhibits porosity ranging from 3% to 8%, with an average of 5% and permeability between 0.001 and 0.005 mD, averaging 0.5 mD. Its irregular distribution throughout the 2BSSS Group future contributes to significant reservoir heterogeneity. Limestone has distinctly lower reservoir quality compared to siltstone. Porosity is lower than 3%, and permeability is lower than 0.002 mD. Mudstone contains abundant silt-sized detrital quartz and carbonate grains, resulting in porosity and permeability values comparable to siltstone. Its porosity is close to10%, and permeability is close to 0.03 mD. However, its low abundance of 3.6% within the 2BSSS Member, it contributes minimally to reservoir performance. In summary, this study indicates that lithology is a primary sedimentological control of the porosity and permeability within the 2BSSS member. Compositional segregation during turbidite transport drives spatial variations in composition and reservoir properties, resulting in significant heterogeneity across the depositional system.

3.6 CONCLUSIONS

The 2BSSS Member of Bone Spring Formation comprises a mixed siliciclastic-carbonate turbidity system. High-frequency sequence stratigraphic analysis indicates the 2BSSS Member can be subdivided into three high-frequency cycles (2BSSS-1, 2BSSS-2, and 2BSSS-3), each defined by distinct stacking patterns and lithologic characteristics. The sequences display a basinward-thickening, progradational trend shaped by relative sea-level fluctuations. Turbidite deposition is controlled by slope morphology and sediment supply, producing laterally extensive, siliciclastic-rich packages.

Turbidite deposits in the 2BSSS Member exhibit complex lithologic compositions, reflecting variable depositional energy, sediment supply, and diagenetic alteration. Lithologies include siltstone, dolomite-cemented siltstone, limestone, and mudstone. RHOmaa–Umaa crossplots effectively distinguish these lithologies, with siltstone and limestone exhibiting the highest classification accuracy.

The MLP model, trained on core and log-derived features, accurately predicts lithology across the study area. Combined with crossplot analysis, it provides robust classification in wells lacking complete petrophysical datasets. Although the 2BSSS Member is considered a siliciclastic-rich interval, results reveal a significant proportion of limestone (45%), exceeding that of siltstone (30.5%) and dolomite-cemented siltstone (20.9%). Even in the siliciclastic-rich units 2BSSS-1 and 2BSSS-3, the combined siltstone proportion is only 23.3%, indicating that carbonate deposits remain volumetrically significant even within siltstone-rich intervals.

Bayesian lithology inversion integrates well data with seismic impedance to map lateral variations in lithology. The inversion revealed laterally continuous siltstone belts, patchy dolomite-cemented zones, and widespread but variable limestone bodies. Despite some uncertainty, spatial probability volumes captured fine-scale lithologic heterogeneity and depositional trends aligned with slope-to-basin transitions. These results highlight turbidite lithologies' complex and discontinuous nature and enhance subsurface prediction accuracy.

Siltstone shows the best reservoir properties (average porosity approximately 8%, permeability approximately 0.05 mD, while dolomite-cemented siltstone and limestone exhibit reduced porosity and permeability due to diagenesis. Lithologic variability and depositional trends create significant heterogeneity, impacting reservoir connectivity and quality.

ACKNOWLEDGMENTS

We gratefully acknowledge Devon Energy for providing the data used in this study and granting permission to publish the findings. We also acknowledge the technical support offered by Petrel from SLB, Hampson-Russell form Geosoftware, Geolog from AspenTech, and AASPI form the University of Oklahoma.

REFERENCES

Adams, D. C., and G. R. Keller, 1996, Precambrian basement geology of the Permian Basin region of west Texas and eastern New Mexico: A geophysical perspective: AAPG Bulletin, v. 80, no. 3, p. 410–431.

Asmus, J. A., and G. M. Grammer, 2013, Characterization of deep-water carbonate turbidites and mass-transport deposits utilizing high-resolution electrical borehole image logs: Upper Leonardian (lower Permian) Upper Bone Spring Limestone, Delaware Basin, Southeast New Mexico and West Texas: Gulf Coast Association of Geological Societies Transactions, v. 63, p. 27–65.

Asquith, G., and D. Krygowski, 2004a, Porosity Logs, in G. Asquith and D. Krygowski, Basic Well Log Analysis: AAPG Methods in Exploration 16, p. 37–76

Asquith, G., and D. Krygowski, 2004b, Petrophysical Techniques, in G. Asquith and D. Krygowski, Basic Well Log Analysis: AAPG Methods in Exploration 16, p. 137–149.

Barker, C. E., 1986, Fluid inclusion, stable isotope, and vitrinite reflectance, evidence for the thermal history of the Bone Spring Limestone, southern Guadalupe Mountains, Texas: Society of Economic Paleontologists and Mineralogists, Special Publication, v. 38, p. 189–203.

Bouma, A. H., 1996, Initial comparison between fine- and coarsegrained submarine fans and the Brushy Canyon Formation sandstones, in W. D. DeMis, and A. G. Cole, eds., The Brushy Canyon play in outcrop and subsurface: concepts and examples: guidebook: Society of Economic Paleontologists and Mineralogists Permian Basin Section Publication 96–38, p. 41–50.

Brown, A., 2019, Post-Permian history of the greater Permian Basin area, in S. C. Ruppel, ed., Anatomy of a Paleozoic basin: The Permian Basin, USA: Austin Texas, The University of Texas at Austin, Bureau of Economic Geology Report of Investigations 285 and AAPG Memoir 118, v. 1, p. 97–134.

Chiarella, D., and S. G. Longhitano, 2012, Distinguishing depositional environments in shallow-water mixed bio-siliciclastic deposits on the basis of the degree of heterolithic segregation (Gelasian, southern Italy): Journal of Sedimentary Research, v. 82, no. 12, p. 969–990.

Chiarella, D., S. G. Longhitano, and M. Tropeano, 2017, Types of mixing and heterogeneities in siliciclastic carbonate sediments: Marine and Petroleum Geology, v. 88, p. 617–627.

Delashmit, W. H., and M. T. Manry, 2005, May. Recent developments in multilayer perceptron neural networks, in Proceedings of the seventh annual Memphis area engineering and science conference, MAESC, Vol. 7, p. 1–15.

Drzewiecki, P. A., and J. A. Simó, 2002, Depositional processes, triggering mechanisms and sediment composition of carbonate gravity flow deposits: examples from the Late Cretaceous of the south-central Pyrenees, Spain: Sedimentary Geology, v. 146, no. 1–2, p. 155–189.

Ewing, T. E., 2019, Tectonics of the West Texas (Permian) Basin–Origins, structural geology, subsidence, and later modification, in S. C. Ruppel, ed., Anatomy of a Paleozoic basin: The Permian Basin, USA: Austin, Texas, The University of Texas at Austin, Bureau of Economic Geology Report of Investigations 285 and AAPG Memoir 118, v. 1, p. 63–96.

Ewing, T. E., M. A. Barnes, and R. E. Denison, 2019, Proterozoic foundations of the Permian Basin, west Texas and southeastern New Mexico – A review, in S. C. Ruppel, ed., Anatomy of a Paleozoic basin: The Permian Basin, USA: Austin, Texas, The University of Texas at Austin, Bureau of Economic Geology Report of Investigations 285 and AAPG Memoir 118, v. 1, p. 43–61.

Fairhurst, B., T. Ewing, and B. Lindsay, 2021, West Texas (Permian) Super Basin, United States: Tectonics, structural development, sedimentation, petroleum systems, and hydrocarbon reserves: AAPG Bulletin, v. 105, no. 6, p.1099–1147.

Gardner, M. H., and J. M. Borer, 2000, Submarine channel architecture along a slope to basin profile, Brushy Canyon Formation, west Texas, in A. H. Bouma and C. G. Stone, eds., Fine-grained turbidite systems: AAPG Memoir, v. 72, p. 195–214.

Gardner, M. H., J. M. Borer, J. J. Melick, N. Mavilla, M. Dechesne, and R. N. Wagerle, 2003, Stratigraphic process–response model for submarine channels and related features from studies of Permian Brushy Canyon outcrops, West Texas: Marine and Petroleum Geology, v. 20, no. 6, p. 757–787.

Golovkoa, V. A., 2017, Deep learning: an overview and main paradigms: Optical Memory and Neural Networks, v. 26, no. 1. p. 1–17.

Hamlin, H. S., and R. W. Baumgardner Jr., 2020, Lower Permian (Leonardian) deepwater successions in the Midland Basin: Lithofacies, stratigraphy, reservoirs, and source rocks, in S. C. Ruppel, Anatomy of a Paleozoic basin: The Permian Basin, USA: Austin Texas, Bureau of Economic Geology Report of Investigations 285 and AAPG Memoir 118, v. 2, p. 283–320.

Hodson, J. M., and J. Alexander, 2010, The effects of grain density variation on turbidity currents and some implications for the deposition of carbonate turbidites: Journal of Sedimentary Research, v. 80, no. 6, p. 515–528.

Hurd, G. S., C. Kerans, S. Fullmer, and X. Janson, 2016, Large-scale inflections in slope angle below the shelf break: A first order control on the stratigraphic architecture of carbonate slopes: Cutoff Formation, Guadalupe Mountains National Park, West Texas, USA: Journal of Sedimentary Research, v. 86, no. 4, p. 336–362.

Hurd, G.S., C. Kerans, E. L. Frost, J. A. Simo, and X. Janson, 2018, Sediment gravity-flow deposits and three-dimensional stratigraphic architectures of the linked Cutoff, upper Bone Spring, and upper Avalon system, Delaware Basin. AAPG Bulletin, v. 102, no. 9, p. 1703–1737.

Kane, I. A., A. S. M. Pontén, B. Vangdal, J. T. Eggenhuisen, D. M. Hodgson, and Y. T. Spychala, 2017, The stratigraphic record and processes of turbidity current transformation across deep-marine lobes: Sedimentology, v. 64, no. 5, p. 1236–1273.

Kerans, C. and K. A. Kempter, 2002, Hierarchical stratigraphic analysis of a carbonate platform, Permian of the Guadalupe Mountains, AAPG discovery series no. 5.

Kerans, C., and S. C. Ruppel, 2020, Composite and high frequency cyclicity in Middle Permian shelf carbonates: The San Andres and Grayburg (Guadalupian) succession in the Permian Basin, in S. C. Ruppel, eds., Anatomy of a Paleozoic basin; The Permian Basin, USA, volume 2: Austin, Texas, The University of Texas at Austin, Bureau of Economic Geology Report of Investigations 285 and AAPG Memoir, v.118, p. 349–398.

Kerans, C., C. Zahm, B. Garcia-Fresca, and P. Harris, 2017, Guadalupe Mountains, West Texas and New Mexico: Key excursions: AAPG Bulletin, v. 101, no. 4, p. 465–474.

Kolbjørnsen, O., A. Buland, R. Hauge, P. Røe, A. O. Ndingwan, and E. Aker, 2020, Bayesian seismic inversion for stratigraphic horizon, lithology, and fluid prediction: Geophysics, v. 85. p. R207–R221.

Kvale, E. P., C. M. Bowie, C. Flenthrope, C. Mace, J. M. Parrish, B. Price, S. Anderson, and W. A. DiMichele, 2020, Facies variability within a mixed carbonate–siliciclastic sea-floor fan (upper Wolfcamp Formation, Permian, Delaware Basin, New Mexico): AAPG Bulletin, v. 104, no. 3, p. 525–563.

Lambert, B., 2018, A Student's Guide to Bayesian Statistics, SAGE, London.

Larsen, A. L., M. Ulvmoen, H. More, and A. Buland, 2006, Bayesian lithology/fluid prediction and simulation on the basis of a Markov-chain prior model: Geophysics, v. 71, no. 5, p. B69–B78.

Mazzullo, S. J., A. M. Reid, and J. M. Gregg, 1987, Dolomitization of Holocene Mg-calcite supratidal deposits, Ambergris Cay, Belize: Geological Society of America Bulletin, v. 98, no. 2, p. 224–231.

Minisini, D. and Desjardins, P., 2024. Application of a deep-water stratigraphic framework to the production of the Wolfcampian units in the Permian Basin. AAPG Bulletin, v. 108, no. 1, p. 179–212.

Montgomery, S. L., 1997a, Permian Bone Spring formation: sandstone play in the Delaware basin part I—slope. AAPG Bulletin, v. 81, no. 8, p. 1239–1258.

Montgomery, S. L., 1997b, Permian bone spring formation: Sandstone play in the Delaware Basin, part II—Basin. AAPG bulletin, v. 81, no. 9, p. 1432–1434.

Moscardelli, L., Ochoa, J., Lunt, I. and Zahm, L., 2019. Mixed siliciclastic–carbonate systems and their impact for the development of deep-water turbidites in continental margins: A case study from the Late Jurassic to Early Cretaceous Shelburne subbasin in offshore Nova Scotia: AAPG Bulletin, v.103, no. 10, p. 2487–2520.

Nance, H. S., and H. S. Hamlin, 2020, The bone spring formation (Leonardian) of the Delaware Basin: Deepwater lithofacies and Stratigraphy. in S. C. Ruppel, ed., Anatomy of a Paleozoic Basin: The Permian Basin, USA: Austin, Texas, The University of Texas at Austin, Bureau of Economic Geology Report of Investigations 285 and AAPG Memoir 118, v. 2, p. 321–348.

Nance, H.S., and H. Rowe, 2015, Eustatic controls on stratigraphy, chemostratigraphy, and water mass evolution preserved in a Lower Permian mudrock succession, Delaware Basin, west Texas, USA. Interpretation, v. 3, no. 1, p. SH11–SH25.

Playton, T. E., and C. Kerans, 2018, Architecture and genesis of prograding deep boundstone margins and debris-dominated carbonate slopes: Examples from the Permian Capitan Formation, Southern Guadalupe Mountains, West Texas: Sedimentary Geology, v. 370, p. 15–41.

Pranter, M.J., N. F. Hurley, and T. L. Davis, 2004, Anhydrite distribution within a shelf-margin carbonate reservoir: San Andres Formation, vacuum field, New Mexico, USA: Petroleum Geoscience, v. 10, no. 1, p. 43–52.

Rankey, E. C., and D. F. Doolittle, 2012, Geomorphology of carbonate platform-marginal uppermost slopes: Insights from a Holocene analogue, Little Bahama Bank, Bahamas: Sedimentology, v. 59, no. 7, p. 2146–2171.

Reijmer, J. J. G., T. Mulder, and J. Borgomano, 2015, Carbonate slopes and gravity deposits: Sedimentary Geology, v. 317, p. 1–8.

Ruppel, S. C., 2019, Anatomy of a Paleozoic basin: the Permian Basin, USA: introduction, overview, and evolution, in S. C. Ruppel, ed., Anatomy of a Paleozoic basin: the Permian Basin, USA: The University of Texas at Austin, Bureau of Economic Geology Report of Investigations 285 and AAPG Memoir 118, v. 1, p. 1–27.

Ruppel, S. C., and W. B. Ward, 2013, Outcrop-based characterization of the Leonardian carbonate platform in west Texas: Implications for sequence-stratigraphic styles in the Lower Permian: AAPG Bulletin, v. 97, no. 2, p. 223–250.

Sarker, I. H., 2021, Deep cybersecurity: A comprehensive overview from neural network and deep learning perspective: SN Computer Science, v. 2, no. 3, p. 154–170.

Sayers, C. M., S. Dasgupta, A. Koesoemadinata, and M. Shoemaker, 2019, Rock physics of the Wolfcamp formation, Delaware Basin: Geophysics, v. 84, no. 6, p. B353–B361.

Schlager, W., J. J. Reijmer, and A. Droxler, 1994, Highstand shedding of carbonate platforms: Journal of Sedimentary Research, v. 64, no. 3b, p. 270–281.

Schmidhuber J., 2015, Deep learning in neural networks: An overview: Neural Networks, v. 61, p. 85–117.

Schumaker, R. C., 1992, Paleozoic structure of the Central Basin Uplift and adjacent Delaware Basin, West Texas: AAPG Bulletin, v. 76, no. 11, p. 1804–1824.

Talling, P. J., 2013, Hybrid submarine flows comprising turbidity current and cohesive debris flow: Deposits, theoretical and experimental analyses, and generalized models: Geosphere, v. 9, no. 3, p. 460–488.

Walker W, Z. R. Jobe, J. F. Sarg, and L. Wood, 2021, Progradational slope architecture and sediment distribution in outcrops of the mixed carbonate-siliciclastic Bone Spring Formation, Permian Basin, west Texas: Geosphere, v. 17, no. 4, p. 1268–1293.

APPENDICES

Appendix A: RHOmaa-Umaa Crossplot Analysis

Apparent matrix density (ρ_{maa}, in g/cm^3) and the apparent volumetric cross section (U_{maa}, in barns/cm^3) are calculated from neutron, density, and photoelectric-effect logs using the following equations:

$$U_{maa} = \frac{(p_e \times \rho_b) - (\Phi_{\mathrm{ND}} \times U_{fl})}{1 - \Phi_{\mathrm{ND}}} \quad \text{(A-1)}$$

$$\rho_{maa} = \frac{\rho_b - (\Phi_{\mathrm{ND}} \times \rho_{fl})}{1 - \Phi_{\mathrm{ND}}} \quad \text{(A-2)}$$

Where P_e (barns/electron) is photoelectric absorption index, it needs to be converted to a volumetric measure by multiplying it by the electron density, $P_e = (\rho_b + 0.1883)/1.0704$; ρ_b (g/cm^3) is bulk density from density log; φ_{ND} (fraction) neutron-density porosity from neutron log; ρ_{fl} (g/cm^3) is flushed zone pore fluid density (= 1.0 g/cm^3 for freshwater mud filtrate); U_{fl} (barns/cm^3) is photoelectric absorption of fluid (= 0.398 barns/cm^3 for freshwater mud filtrate).

Matrix identification triangular charts are construct using the following apparent matrix values of common lithologies.

Table A. Apparent matrix values for calculated for common minerals

Mineral	ρ_{maa} (g/cm^3)	U_{maa} (barns/cm^3)
Sandstone	2.644	4.78
Limestone	2.710	13.80
Dolomite	2.877	8.98

Appendix B: Multilayer Perceptron (MLP)

MLP is a type of artificial neural network used in supervised learning. In this study, all computations are based on Scikit-learn functions in Python, the algorithms available on the Scikit-learn website: https://scikit-learn.org

The model requires hyperparameter tuning to suit the dataset. Table B-1 outlines the MLP architecture and the parameters used in the algorithm

Table B-1 Parameters for MLP applied to predict lithology classification

Input size	4
Number of hidden layers	3
Number of neurons per hidden layer	50; 25; 5
Activation function	ReLU
Solver	Adam
Iteration	100

Accuracy (A), Precision (P), Recall (R), and F1-score (F1) are used to evaluate the classification performance.

Accuracy measures the proportion of correct predictions made by the model.

$$A = \frac{TP+TN}{TP+TN+FP+FN} \quad \text{(B-1)}$$

Precision measures how many of the predicted positive labels were actually correct,

$$P = \frac{TP}{TP+FP} \quad \text{(B-2)}$$

Recall measures how well the MLP correctly identifies actual positives in the data.

$$R = \frac{TP}{TP+TP+FN} \quad \text{(B-3)}$$

F1-score is the harmonic mean of Precision and Recall.

$$F1 = 2 \times \frac{R \times P}{R + P} \tag{B-4}$$

Where: TP (True Positive): The model correctly predicted the positive class (e.g., correctly identifying a lithology that is actually present). TN (True Negative): The model correctly predicted the negative class (e.g., correctly identifying a lithology is not present). FP (False Positive): The model incorrectly predicted the positive class (e.g., predicting a lithology that is not actually present). FN (False Negative): The model incorrectly predicted the negative class (e.g., failing to identify a lithology that is actually present).

Appendix C: Bayesian Lithology Inversion

Bayesian lithology inversion is to predict lithologies by integrating seismic data with prior geological knowledge. It uses the framework of Bayes' theorem to estimate the posterior probability of a specific lithology. Bayesian lithology inversion is formulated as:

$$P(B_i|A) = \frac{P(A|B_i)P(B_i)}{P(A)} \qquad \text{(C-1)}$$

Where: A represents seismic attribute; B_i denotes a lithologic classification; $P(B_i|A)$ is the posteriori probability, also known as the conditional probability, which represents the probability of a specific lithology B_i that results in a seismic attribute value of A; $P(A|B_i)$ is the probability of A for lithology B_i, it's the probability of seismic attribute for the specific lithologic proportion of B_i; $P(B_i)$ is the prior probability of lithology without other preconditions, it is derived from lithologic proportions; P(A) is the total probability of a given seismic attribute value, regardless of lithologic types.

CONCLUSIONS

This dissertation applies seismic sequence stratigraphy and seismic geomorphology to analyze the stratigraphic architecture and depositional architectural elements of fluvial strata in the Northern Malay Basin. It also integrates seismic attributes, inversion results, and well data to predict reservoir lithology in deep-water turbidite systems of the Delaware Basin. These studies highlight the stratigraphic and sedimentological complexity of fluvial and turbidite depositional systems.

In the low-gradient coastal plain of the North Malay Basin, the Falling-Stage Systems Tract (FSST) lacks the typical progradational stacking patterns and diagnostic offlap terminations characteristic of standard sequence stratigraphic models. Subaerial exposure and subsequent transgressive erosion have largely removed the FSST across the coastal plain, making it a missing link in the array of systems tracts. However, incised valleys preserve stratigraphic records of base-level fluctuations and fluvial processes, with FSST deposits situated above the subaerial unconformity and below the transgressive ravinement surface. Multi-stage terraced fluvial deposits within these valleys reflect episodic base-level fall, marked by fluvial terrace geomorphology along their upper boundaries. Identifying FSST records within incised valleys provides critical insights into stratigraphic completeness and preservation variability across diverse depositional settings. Seismic geomorphological patterns identified in this study refine sequence stratigraphic models by illustrating the seismic geomorphological expression of the FSST.

This study identifies and interprets the upper and lower boundaries of falling-stage systems tracts (FSST) developed within a coastal plain setting. The upper boundary is a composite surface formed by the amalgamation of a subaerial unconformity and a transgressive ravinement surface. In interfluvial areas, this surface is characterized by undulating reflections near valley margins in seismic profiles and appears as dendritic, tidally influenced distributary channels in seismic slices. In intrafluvial areas, the composite surface is marked by small tidal scour gullies developed atop channel sandstones or point bars. The lower boundary of the FSST corresponds to a regional subaerial unconformity, which may align stratigraphically with the upper boundary of shelf-margin FSST deposits. This spatial correlation establishes a stratigraphic linkage between the coastal plain FSST and its shelf-margin counterpart.

In low-gradient coastal plain settings, two morphologically distinct types of incised valleys—low-sinuosity and high-sinuosity—are observed within the same FSST stage. These valleys commonly display multi-stage terraces dipping toward the valley axis. Low-sinuosity valleys are characterized by deeply incised, straight to slightly sinuous geometries, indicative of high-energy incision under confined conditions. In contrast, high-sinuosity valleys retain meandering morphologies inherited from pre-existing highstand fluvial systems. Their limited lateral confinement and proximity to the paleo-estuarine zone likely contributed to the preservation of sinuosity during subsequent incisions.

High-resolution seismic geomorphological analysis reveals that abandoned channel mud plugs are extensively developed within fluvial sandstone bodies due to lateral channel migration, avulsion, and base-level changes. This study establishes recognition criteria for identifying abandoned channels using seismic geomorphology, including: (1) On seismic profiles, abandoned channel mud plugs typically display U-shaped geometries and occur consistently in the upper to middle parts of fluvial sandstone bodies, often at the distal ends of inclined or chaotic reflections; (2) Compared to the variable continuity and amplitude of channel sandstones, abandoned channel mud plugs exhibit weak or transparent seismic responses; (3) On seismic slices, they are characterized by low coherence values and appear as embedded, continuous sinuous or crescentic features within channel sandstones; (4) In contrast to the variable widths of fluvial sandbodies, abandoned channel mud plugs exhibit relatively consistent widths. These criteria enhance the interpretive framework of seismic geomorphology for fluvial depositional systems.

Four typical types of abandoned channel mud plugs are identified in the Pliocene–Pleistocene strata: (1) low-sinuosity single abandoned channels, (2) high-sinuosity single abandoned channels, (3) neck cutoff abandoned channels, and (4) bifurcation abandoned channels. These features ' morphological variations and spatial distributions offer new insights into the seismic geomorphological interpretation of fluvial depositional systems. Within channel belts, seismic attributes such as coherence image continuous sinuous or discontinuous crescent-shaped features more likely represent abandoned channel mud plugs than channel sandstones. This distinction provides important guidance for interpreting fluvial systems, particularly under low seismic resolution conditions.

Abandoned channel mud plugs represent a substantial component of channel sandstones in the study area. Most act as partial barriers, reducing the connectivity of the upper half to two-thirds of the channel sandstones. This barrier effect is more pronounced in incised channel belts, where mud plugs can form complete barriers in straight channel segments. Consequently, abandoned channel mud plugs significantly hinder channel sandstone connectivity and increase intermediate-scale reservoir heterogeneity.

In the Delaware Basin, the Second Bone Spring Sandstone Member (2BSSS) represents a mixed siliciclastic–carbonate deep-water turbidite system characterized by variable progradational stratigraphic patterns, high-frequency cyclicity, and significant lithological variability. High-frequency sequence stratigraphy of the 2BSSS reveals that during the falling-stage and lowstand systems tracts, multiple point sources from the northwestern shelf generated extensive (~110 m, 361 ft) turbidite deposits that accumulated on the low-gradient slope and basin floor. These sequences display a basinward-thickening, progradational trend controlled by relative sea-level fluctuations. The 2BSSS consists of three stratigraphic units: two siltstone-rich intervals (2BSSS-1 and 2BSSS-3) separated by a limestone-rich interval (2BSSS-2). The average thicknesses of the upper and lower siltstone intervals are approximately 30 m (98 ft) and 50 m (164 ft), respectively. The lower and upper siltstone intervals contain at least four and three depositional cycles, respectively, with individual cycle thicknesses highly variable but averaging about 10 m (33 ft).

Mixed siliciclastic–carbonate turbidite deposits in the 2BSSS exhibit complex lithologic compositions, reflecting variations in depositional energy, sediment supply, and diagenetic processes. Lithologies identified include siltstone, dolomite-cemented siltstone, limestone, and mudstone. RHOmaa–Umaa crossplot combined with the multilayer perceptron (MLP) neural network are applied to distinguish and predict these lithologies. Although the 2BSSS is classified as a siliciclastic-rich interval, results reveal a substantial proportion of limestone (45%), exceeding that of siltstone (30.5%) and dolomite-cemented siltstone (20.9%). Even within the siliciclastic-dominated intervals 2BSSS-1 and 2BSSS-3, the combined siltstone proportion is only 23.3%, underscoring the volumetric proportion of carbonate deposition throughout the succession.

Bayesian lithology inversion delineates continuous siltstone trends and captures fine-scale lithological heterogeneity in deep-water turbidites. Despite inherent uncertainties, the results reveal depositional patterns consistent with slope-to-basin transitions. These results highlight the complexity and discontinuity of turbidite lithologies and improve the accuracy of subsurface predictions.

These findings demonstrate the value of integrating seismic stratigraphy, geomorphology, attribute analysis, and neural network-based prediction to improve stratigraphic architecture and heterogeneity interpretation. This integrative framework enhances reservoir characterization and prediction while defining a promising trajectory for future research.